Chapter 4

Pump-repump of the molecular motor

Transient absorption (TA) studies in Chapter three of the P-cis and P-trans isomers of a molecular motor gave insight into their excited state dynamics. In this chapter, pump-repump probe (PrPP) TA spectroscopy and pump-dump probe (PDP) TA spectroscopy[1–9] are used to further investigate the excited states and photoproducts of the molecular motor. PrPP spectroscopy prepares short-lived species, such as excited states or metastable photoproducts, with a pump pulse, and excites those species with a repump pulse[1–9]. PDP spectroscopy alters the course of the excited states' evolution by returning population to the ground state by stimulated emission (SE) with a dump pulse. The repump/dump pulse can be delayed with respect to the pump pulse and use various wavelengths to target different species during the evolution of the excited states of the molecule[1–9]. The TA spectra of P-cis and P-trans show excited state absorption (ESA), SE, and photoproduct absorption around 400 nm. These signals are targeted by 404 nm repump/dump pulses at various times during the evolution of the molecular motor to further investigate the excited species and photoproducts (M-cis and M-trans). The relative populations of each excited state and the relative time delays of the repump/dump pulses are shown in Figures 4.1 for P-cis and P-trans.

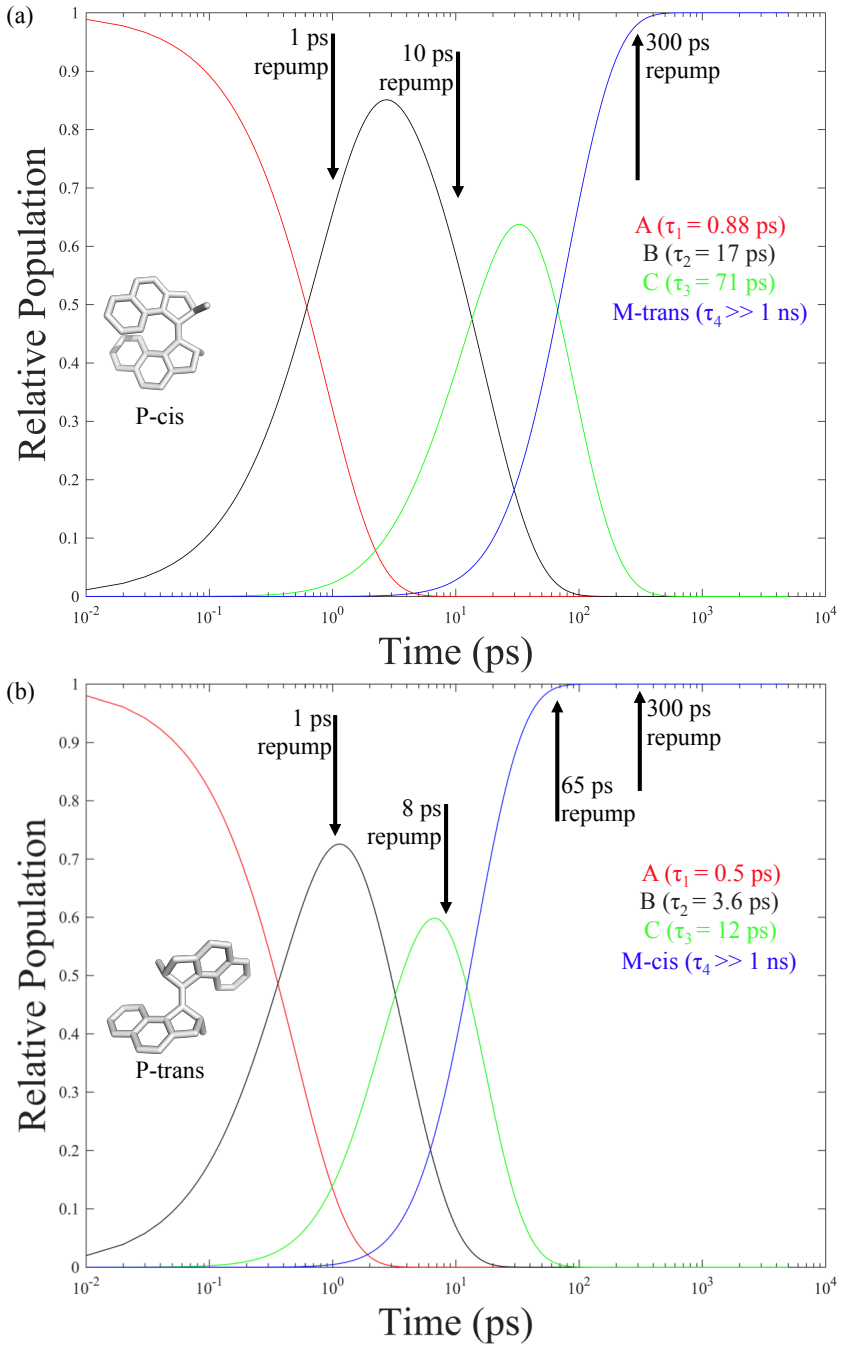

Figure 4.1. Relative populations of the excited states and photoproducts of (a) P-cis and (b) P-trans after excitation by 269 nm. The black arrows indicate various delays for the 404 nm repump pulse.

The photochemistry of the metastable M-trans and M-cis isomers of the molecular motor is an important aspect to understanding the efficiency of light driven molecular motors[10–14]. Photoisomerization of these metastable species in the backwards direction is contrary to the intended use of the molecular motor in driving small-scale devices[15–20]. The photochemistry of the M-helicity conformers has not been studied because they are unstable, undergoing thermal helix inversion on a second to minute timescale in the lab[20,21]. However, a pump pulse easily produces these short-lived intermediates and their lifetimes are extremely long relative to the timescales in a standard TA experiment. M-cis and M-trans are excellent targets for PrPP spectroscopy.

The P-cis molecular motor forms M-trans photoproducts on a ~ 70 ps timescale. The M-trans photoproduct is probed in PrPP by exciting P-cis with 269 nm and repumping M-trans with a 404 nm repump pulse 300 ps afterward. The PrPP TA spectra and timescales match the M-trans TA data in Chapter three. This supports the conclusion that P-trans is in equilibrium with a minor M-trans population in solution that can be selectively excited by 404 nm. Again, the PrPP of the M-trans isomer show two excited state lifetimes and no measureable quantum yield for isomerization.

Similarly, the P-trans molecular motor forms M-cis photoproducts on a timescale of 12 ps or 45 ps, as seen in Chapter three Figures 3.9 and 3.10. A 404 nm repump pulse was introduced at 65 ps and 300 ps after excitation to probe the M-cis conformer. The differences between repumping at 65 ps or 300 ps are within the signal to noise of the PrPP experiment and indicate M-cis photoproducts are formed completely by 65 ps. This leads to the conclusion that M-cis is formed on a ~ 12 ps timescale, rather than a ~ 45 ps timescale. In contrast to M-trans, the PrPP

TA of M-cis show a non-zero quantum yield to form P-trans. Unlike the M-trans conformer, the M-cis conformer undergoes photoisomerization.

Sample Handling

The data are expressed as a double difference to give a background free PrPP or PDP signal, given by the equation below.

$$\Delta\Delta A(\lambda, t) = \Delta A_{pump\&repump} - \Delta A_{pump} - \alpha * \Delta A_{repump}$$

Equation 4.1

Note there is a scale factor "α" which is not equal to one if the repump/dump is absorbed by the ground state of the sample. More details can be found in Chapter two. The background signal ΔA_{repump} contained in $\Delta A_{pump\&repump}$ is only equal to the measured ΔA_{repump} if the sample does not absorb the repump in its ground state. Otherwise, the pump pulse depletes a small percentage of the ground state, decreasing the concentration interacting with the repump pulse. Therefore, the ΔA_{repump} background signal will be too large. In these cases α will be equal to one minus the percent excited by pump. This complication applies to the P-cis repump data because P-cis absorbs the 404 nm repump as demonstrated in Chapter three. This issue does not complicate the P-trans PrPP or PDP data. Unfortunately, this problem was not accounted for during these experiments, because the excitation percentage was not measured rigorously but the percentage is between five and 10 percent.

The probe (320 – 800 nm) was generated by focusing 1 mW of the laser fundamental (808 nm) into a continuously translating 5 mm thick CaF_2 plate with an f = 100 mm lens. The continuum was focused to a 65 μm spot at the sample with an f = 500 mm curved aluminum mirror. A 269 nm 400 nJ pump pulse was focused to a 135 μm spot and overlapped with the probe at a ~ 10° angle. The 404 nm 1 μJ repump/dump pulse was focused to a 200 μm spot and

overlapped with the pump and probe at a -10° angle. The pump and repump/dump polarizations were set to parallel to each other and magic angle to the probe polarization. Relative time delays between the pump and repump/dump were achieved by sending the repump/dump beam down a delay line. Time points in the experiments were achieved by adjusting the relative probe time delay with a separate delay line. Relative pump/repump time delays were chosen to re-excite the intermediate species and photoproducts generated by the pump pulse as depicted in Figure 4.1.

Sample handling in this chapter was similar to sample handling in Chapter two. A key difference in sample preparation was much larger volumes of sample were necessary to avoid significant photoproduct buildup over the course of an experiment. This is because two pump beams are utilized so the sample is exposed to twice as much light over the course of an experiment and twice the numbers of time points are required in order to acquire adequate background signals. Samples were typically 250 mL of ~ 1 mM solutions.

Results – P-cis

P-cis – 404 nm dump pulse at 1 ps. After excitation by 269 nm, P-cis quickly relaxes from the excited state created by 269 nm to the bright "A" state on a timescale faster than the instrument response (IRF, ~ 300 fs) of the experiment. A 404 nm "dump" pulse delayed by 1 ps, whose polarization is parallel to the pump pulse, returns some "A" population to ground state by stimulated emission (SE). The PDP TA data are shown in Figure 4.2. The data are similar to P-cis TA, except ESA and photoproduct signals are negative and SE and GSB signals are positive. ΔΔA is a measure of the change in the transient absorption signal with and without a repump or dump pulse:

$$\Delta\Delta A(\lambda, t) = \Delta A_{repumpON} - \Delta A_{repumpOFF}$$

Equation 4.2

So, when the dump or repump pulse is ON, the original $\Delta A_{repumpOFF}$ signal is greater than the $\Delta A_{repumpON}$ and the $\Delta\Delta A$ signal will appear negative, assuming no new peaks are present. This is because the dump pulse bleached these signals.

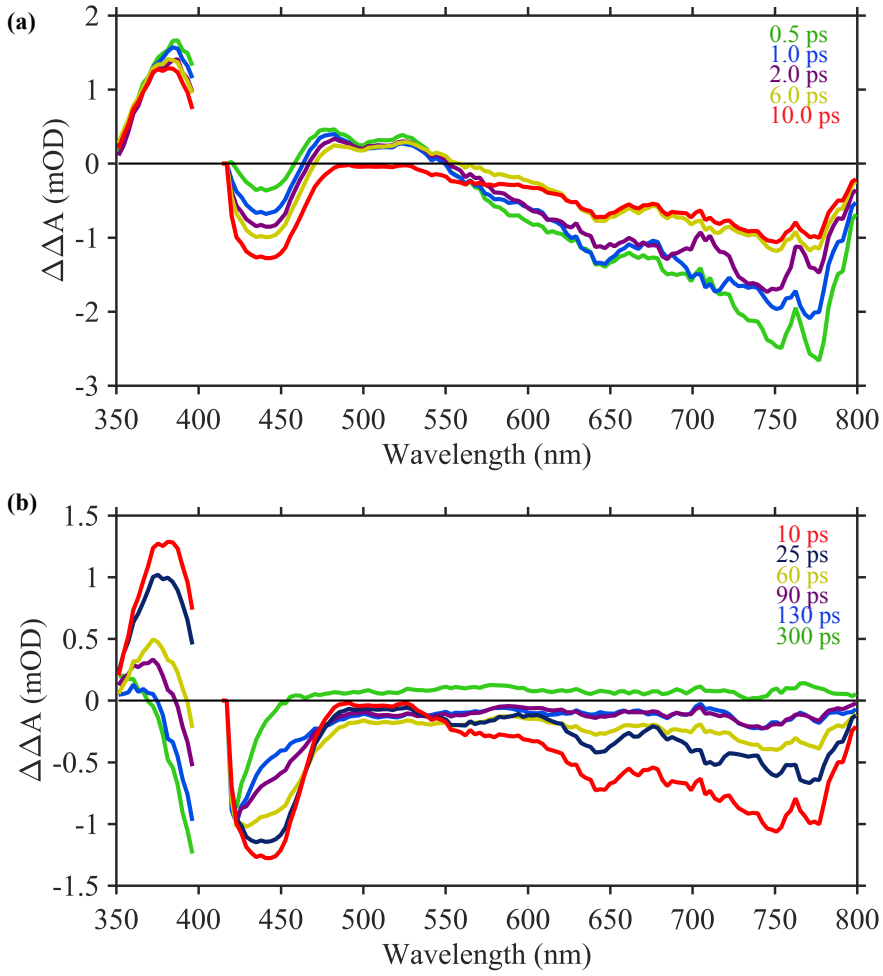

Figure 4.2. 1 ps PDP TA spectra of the P-cis molecular motor. Pump pulse was 269 nm and the dump pulse was 404 nm. (a) PDP spectra at early times: 0.5 ps (green), 1.0 ps (blue), 2.0 ps (purple), 6.0 ps (yellow), 10 ps (red). (b) PDPP spectra at later times: 10 ps (red), 25 ps (dark blue), 60 ps (yellow), 90 ps (purple), 130 ps (royal blue), 300 ps (green).

The PDP spectra are fit to a sum of three exponential decays and a time independent amplitude. As mentioned in the sample handling section, the exact double difference signal for the P-cis experiments depends on the choice of the α scale factor for subtracting the ΔA_{repump} background signal. If α equal to one is used, the global fitting results are $\tau_1 = 0.45$ ps. $\tau_2 = 11$ ps, $\tau_3 = 92$ ps, and $\tau_4 >> 300$ ps. These results are close to the P-cis TA results shown in Chapter three Table 3.2. The DADS and SADS resulting from the global fit are shown in Figure 4.3. Kinetic lineouts demonstrating the quality of the fit results are shown in Figure 4.4.

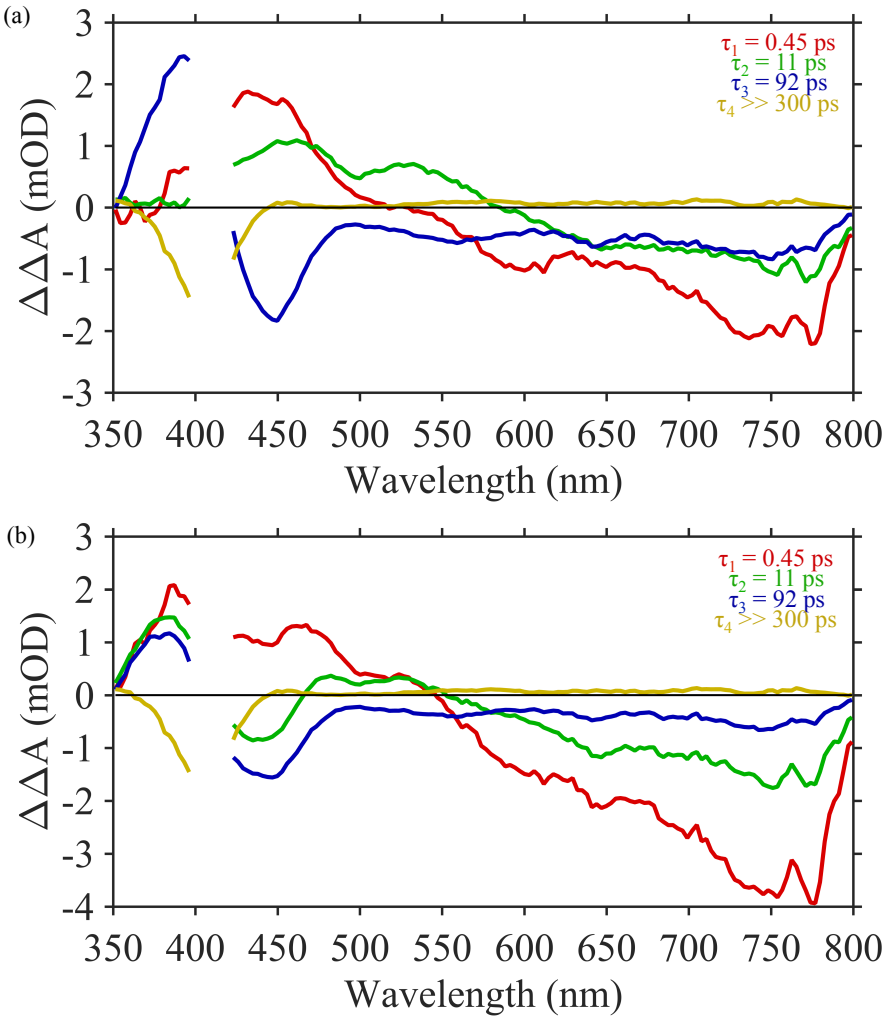

Figure 4.3. Results of global analysis of P-cis 1 ps PDP data. (a) DADS and (b) SADS. Lifetimes from global analysis are 0.45 ps (red), 11 ps (green), 92 ps (blue) and >> 300 ps (yellow).

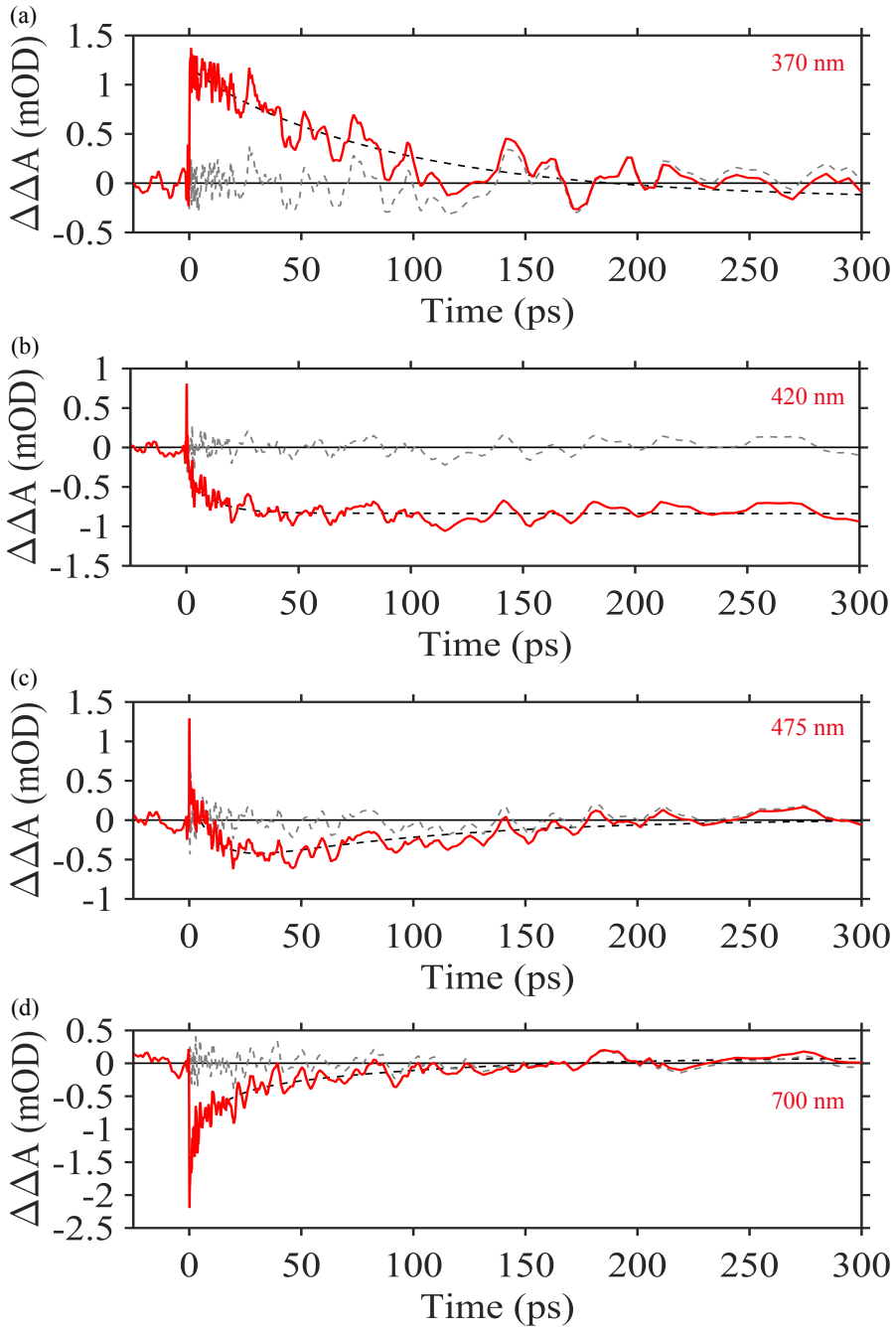

Figure 4.4. Kinetic lineouts (red), fits (black dash) and residuals (grey dash) of the P-cis 1ps PDP data. (a) 370 nm lineout tracking the depleted GSB, (b) 420 nm lineout tracking the depletion of the photoproduct, (c) 475 nm lineout tracking the depletion of SE and intermediate excited states, and (d) 700 nm lineout tracking the depletion of the initial excited state.

P-cis – 404 nm repump at 10 ps. By 10 ps after excitation, P-cis evolves from the "A" state and builds up ~ 56% population in the "B" state and ~ 42% population in the "C" state, assuming a sequential kinetic model as depicted in Figure 4.1a. The TA data in Chapter three Figure 3.3 show a strong ESA peak centered at 435 nm. The 404 nm repump pulse excites a mixture of states "B" and "C". The data analysis is complicated by the presence of a mixture of "B" and "C" and uncertainty in the value of α. The data shown in Figure 4.5 were calculated with α equal to one.

The PrPP data are characterized by depletion of an excited state, showing little if any new ESA peaks. Figure 4.5 shows the PrPP spectra. Notably, the PrPP spectra in Figure 4.5 are similar to the TA spectra of M-trans in Chapter three. Again, the PrPP spectra are inverted relative to the M-trans TA spectra because the repump pulse bleaches the excited state. The sharp peak centered at 645 nm and the peak at ~ 450 nm are in excellent agreement with M-trans TA spectra. In addition, the peak centered at 395 nm agrees with the M-trans UV-vis spectrum. Repumping a mix of the "B" and "C" states of P-cis after 10 ps gives PrPP spectra resembling the excited states of M-trans.

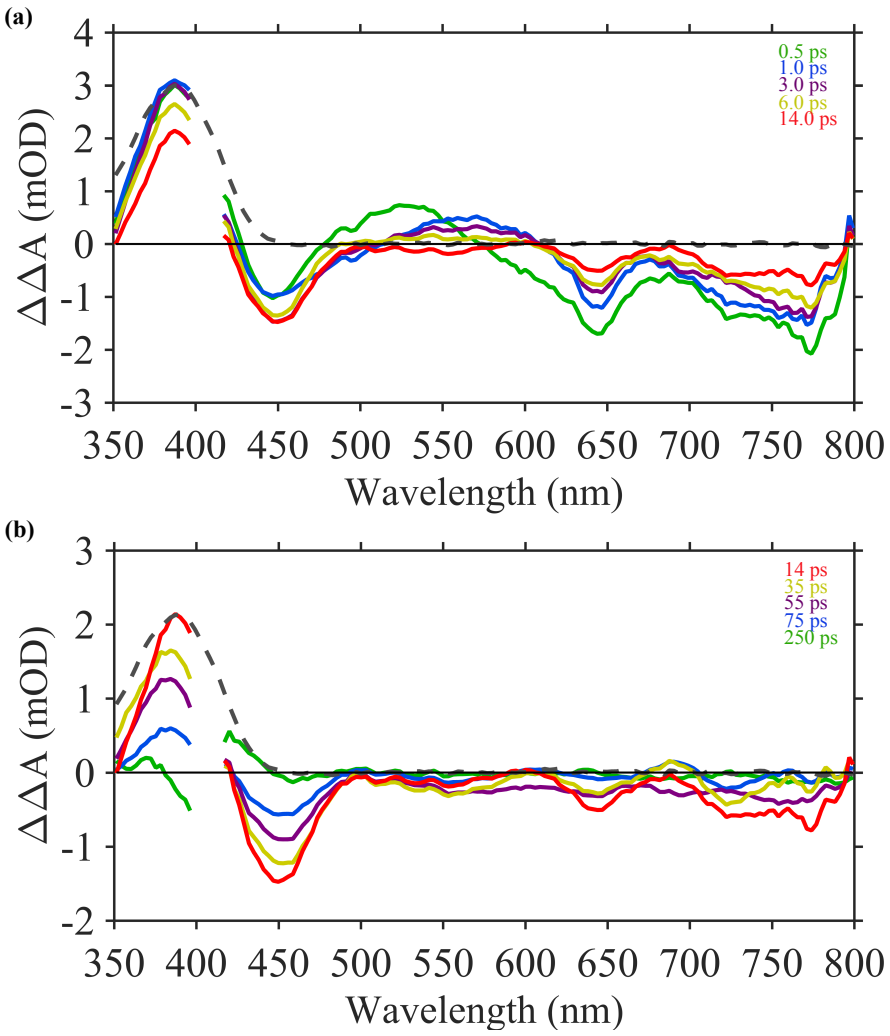

Figure 4.5. PrPP TA spectra after 10 ps repump of P-cis with 404 nm. (a) PrPP spectra at early times: 0.5 ps (green), 1.0 ps (blue), 3.0 ps (purple), 6.0 ps (yellow), 14 ps (red), M-trans UV-vis (grey dash). (b) PrPP spectra at later times: 14 ps (red), 25 ps (yellow), 55 ps (purple), 75 ps (blue), 250 ps (green), M-trans UV-vis (grey dash).

The PrPP data were globally fit to a sum of two exponential decays and a time independent amplitude. The lifetimes from the fit depend on the scale factor α chosen. When α is equal to one, the lifetimes are of $\tau_1 = 2.2$ ps and $\tau_2 = 62$ ps, and when α is equal to 0.95 the lifetimes are equal to $\tau_1 = 1.1$ ps and $\tau_2 = 34$ ps. The DADS and SADS (assuming a sequential model) for α equal to one are displayed in Figure 4.6. Kinetic lineouts showing the quality of the global

analysis are shown in Figure 4.7. Kinetic lineouts in Figure 4.7 are integrated over the three main peaks: 400, 445, and 645 nm.

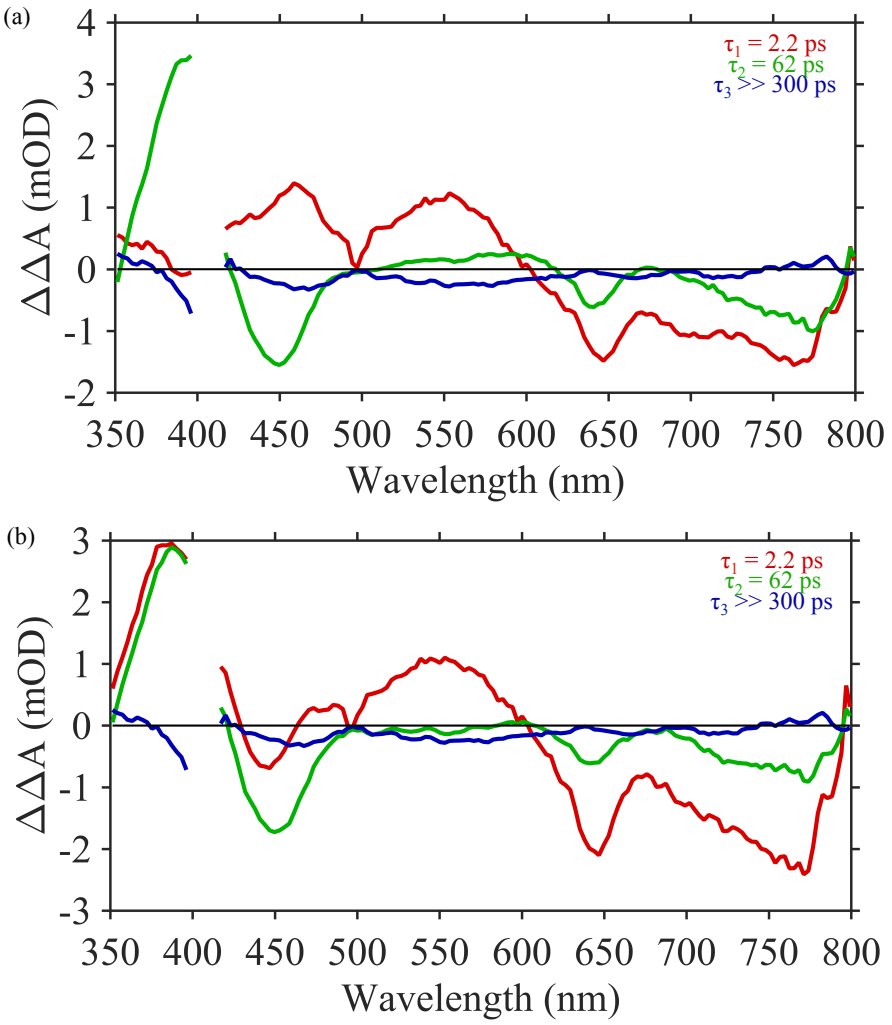

Figure 4.6. Global fitting results after 10 ps repump of P-cis with 404 nm pulses. (a) DADS and (b) SADS (assuming a sequential kinetic model.) The SADS appear to be inverted forms of the M-trans SADS spectra.

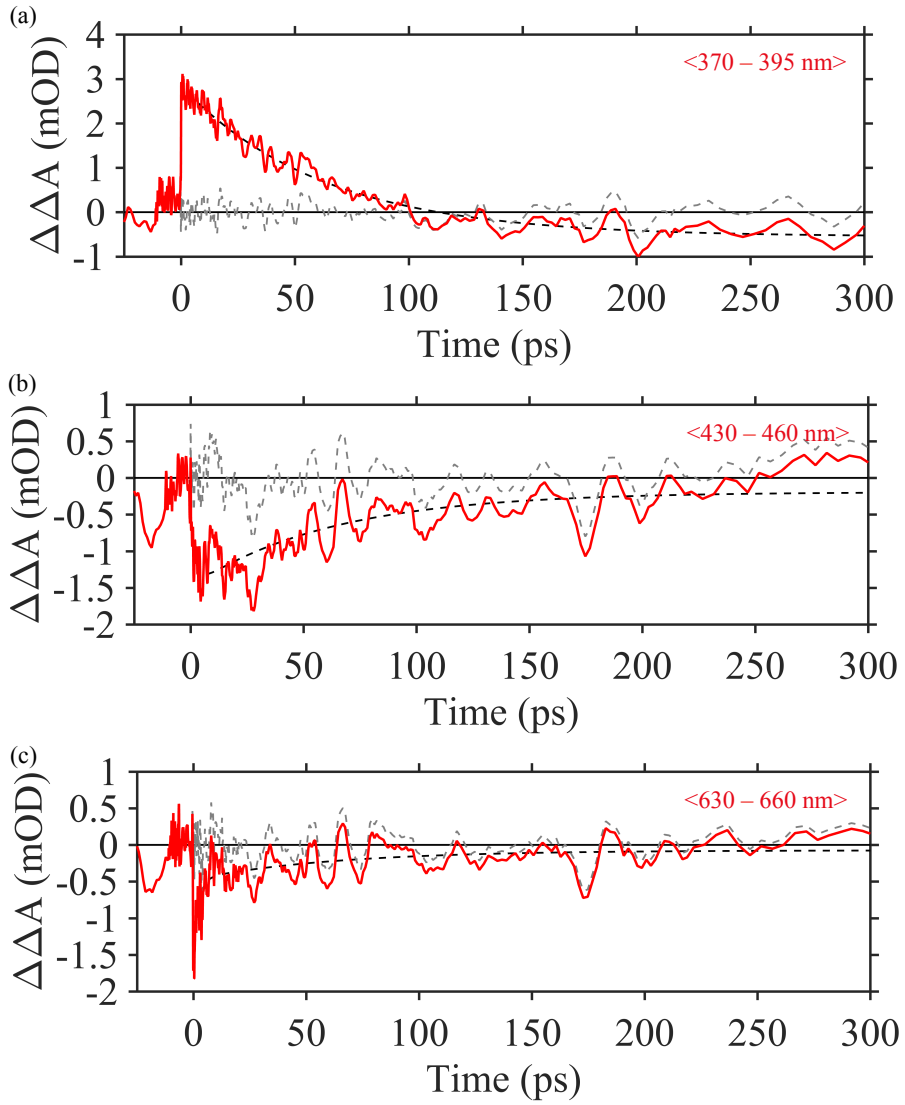

Figure 4.7. Kinetic lineouts from the global analysis of the 10 ps delayed 404 nm repump experiment on P-cis. The data are integrated over the three main spectral features to provide reasonable signal to noise. Data given in red, fits are black dashed lines and residuals are grey dashed lines. (a) the bleach of the M-trans GSB 370-395 nm, (b) bleach of repumped ESA 430 – 460 nm, and (c) the bleach of the ESA 630 – 660 nm.

The choice of α in calculating the double difference data was based on reasonable restrictions on the amount of molecules excited by the pump pulse, between 0% and 7.5%. Since the global analysis results are dependent on the value of α, little confidence is held in the rate constants.

However, all reasonable values of α, from 1.0 to 0.925, yield spectral features showing a bleach of excited state spectra resembling the TA spectra of M-trans.

P-cis – 404 nm repump at 300 ps (M-trans). The M-trans photoproduct is formed 300 ps after excitation of P-cis and does not change for the next 1 nanosecond (ns). This is demonstrated in Chapter three Figures 3.2, 3.3 and 3.4. A 404 nm repump pulse delayed by 300 ps excites the M-trans photoproducts to probe their TA spectra and excited state dynamics.

Figure 4.8 shows the PrPP spectra of the P-cis photoproducts, M-trans. These data agree with measurements made by exciting a sample of the trans molecular motor with 404 nm as shown in Chapter three Figure 3.14. At time delays from 10 to 300 ps the peaks decay to baseline giving rise to no detectable photoproducts. It should be noted the signal to noise of these data is considerably lower and baseline issues at long times show up. The signal to noise is inherently low in these experiments because the repump excites a small percentage of the already small percentage of initially excited molecules. However, the PrPP confirm the assignment of the 404 nm excitation data in Chapter three to M-trans.

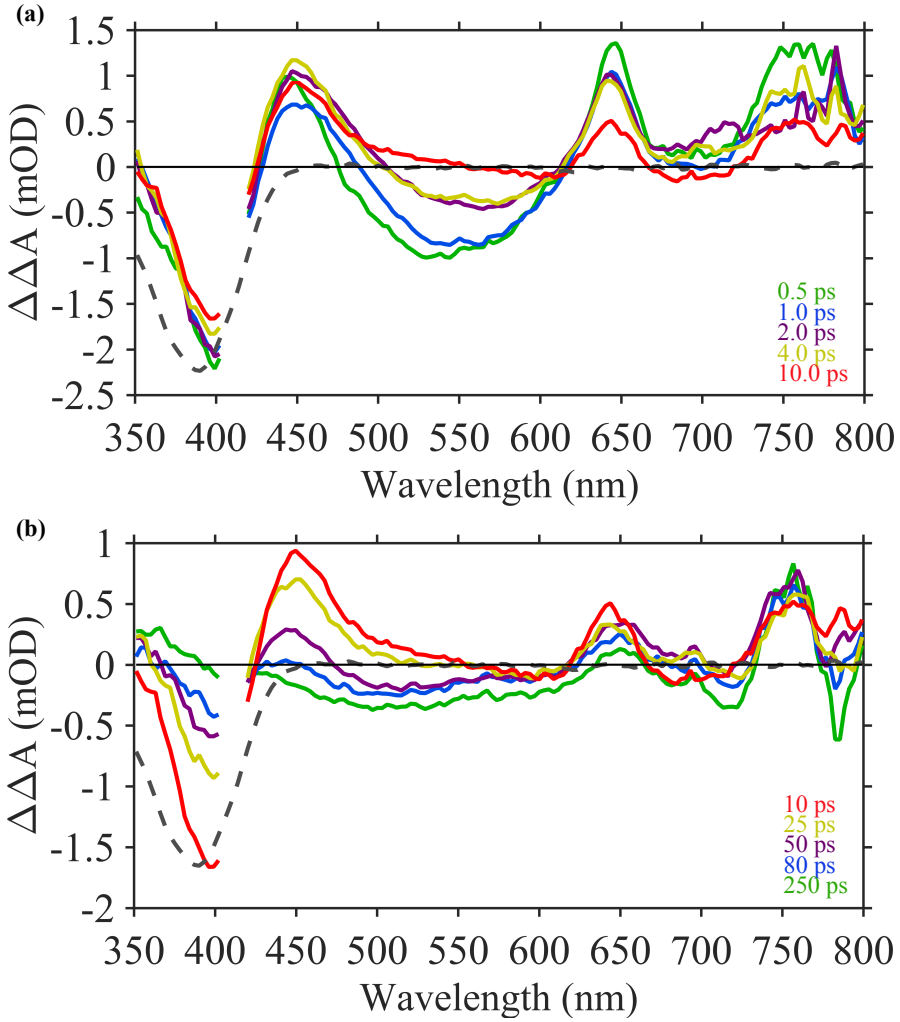

Figure 4.8. PrPP TA spectra of M-trans. (a) Spectra at early times: 0.5 ps (green), 1.0 ps (blue), 2.0 ps (purple), 4.0 ps (yellow), 10 ps (red), and inverted M-trans UV-vis spectra for comparison to the ground state bleach (grey dash). (b) Spectra at later times: 10 ps (red), 25 ps (yellow), 50 ps (purple), 80 ps (blue) and 250 ps (green), inverted M-trans UV-vis spectra for comparison to the ground state bleach (grey dash).

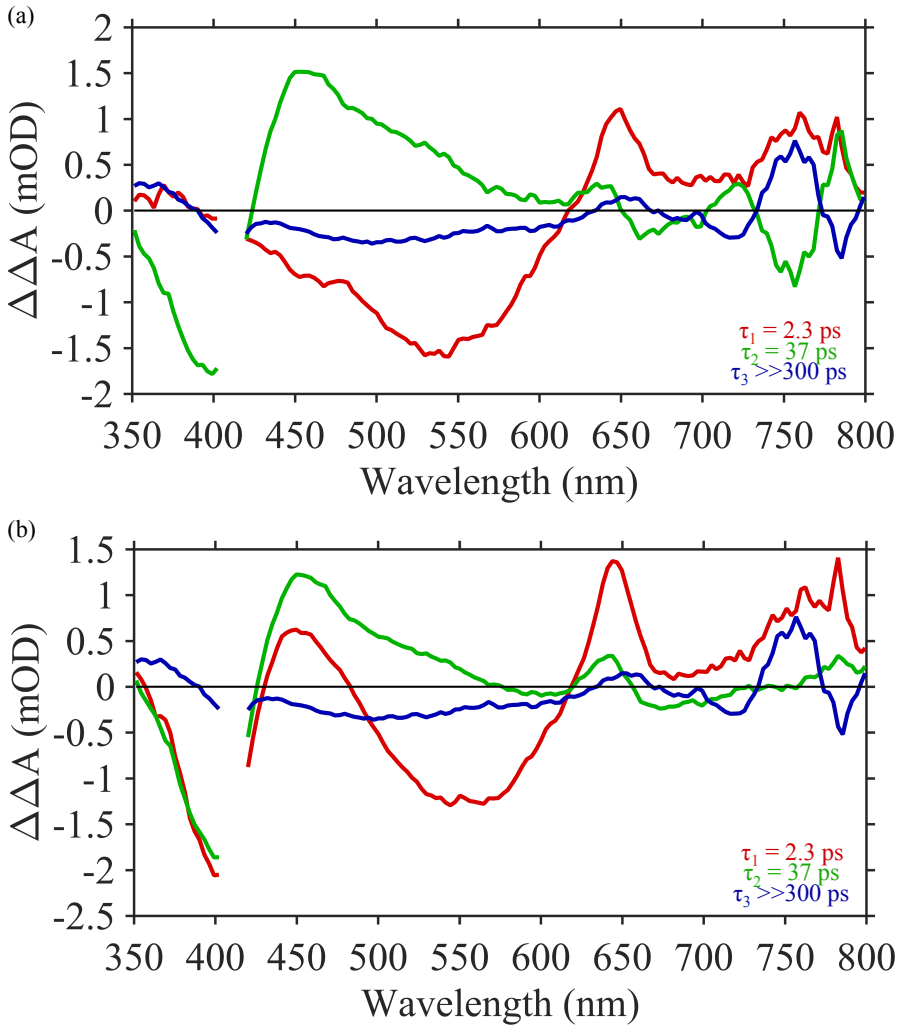

Figure 4.9. Global analysis results of the M-trans PrPP data, acquired by repumping P-cis at 300 ps after initial excitation. (a) Decay associated difference spectra DADS and (b) species associated difference spectra of the M-trans conformer, 2.3 ps component's amplitude (red) and 37 ps component's amplitude (green). A 3rd time independent component (blue) was used to account for any baseline issues. The SADS assume a sequential kinetic model.

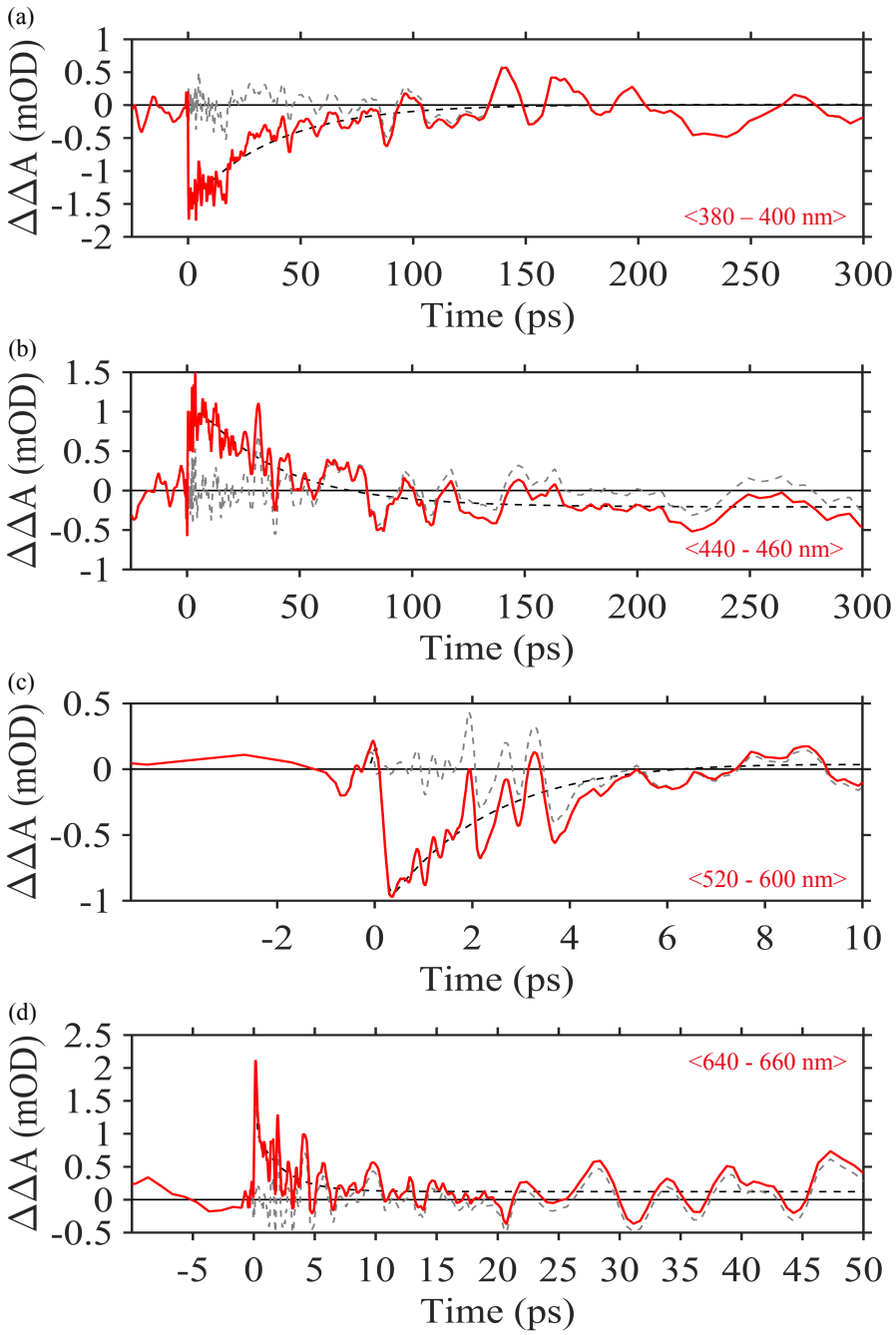

Figure 4.10. Kinetic lineouts of the M-trans PrPP data. (a) GSB signal integrated from 380 to 400 nm, (b) ESA signal integrated from 440 to 460 nm, (c) SE signal integrated from 520 to 600 nm, and (d) ESA signal integrated from 640 to 660 nm. Dashed black lines are the fits of the data and the grey lines are the residuals.

The 300 ps PrPP data were globally fit with a sum of two exponentials and a time independent amplitude. The lifetimes obtained from the fit were $\tau_1 = 2.3$ ps and $\tau_2 = 37$ ps if α is equal to one. If α is equal to 0.95, the lifetimes obtained from the fit are $\tau_1 = 2.6$ ps and $\tau_2 = 41$ ps. The DADS and SADS (assuming a sequential kinetic model) are shown in Figure 4.9 and kinetic lineouts showing the quality of the fit are shown in Figure 4.10. These results are in good agreement with the global analysis of the M-trans data in Chapter three Table 3.4, which are $\tau_1 = 2.3 \pm 0.1$ ps and $\tau_2 = 40 \pm 5$ ps.

Results – P-trans

P-trans – 404 nm dump at 1 ps. After 269 nm excitation the P-trans molecular motor quickly relaxes to its bright "B" state, whose lifetime is ~ 3.6 ps. A 404 nm dump pulse delayed by 1 ps depletes the "B" state by SE. The PDP spectra are shown in Figure 4.11. The PDP spectra resemble the TA spectra of P-trans shown in Chapter three Figure 3.10 (except for the usual inversion).

The PDP data were globally fit to a sum of three exponential decays and a time independent amplitude. The lifetimes obtained from the global analysis were $\tau_1 = 3.5$ ps. $\tau_2 = 11$ ps, $\tau_3 = 48$ ps, and $\tau_4 >> 300$ ps. These fit results are in excellent agreement with the 269 nm excitation TA data shown in Chapter three Table 3.3. The DADS and SADS (assuming a sequential model) obtained from this global analysis are shown in Figure 4.12. Figure 4.13 shows lineouts at key wavelengths in the dataset demonstrating the quality of the global analysis.

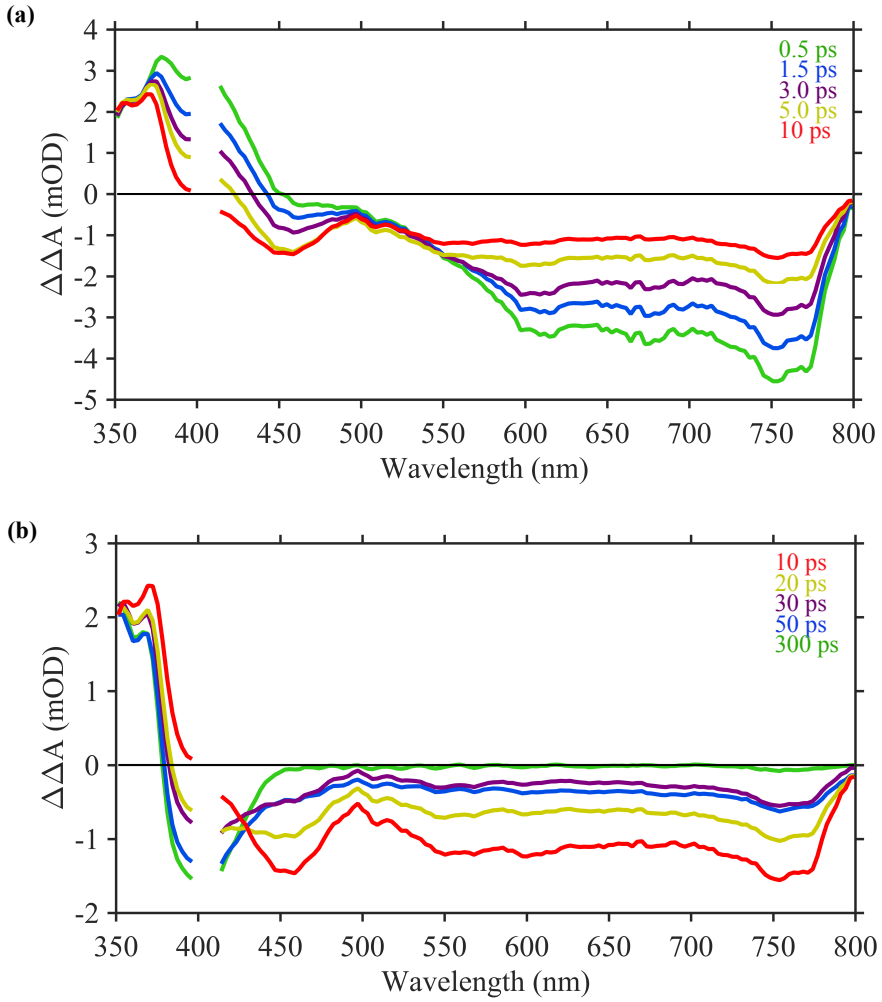

Figure 4.11. PDP spectra of P-trans. The excitation pulse was 269 nm and dump pulse was 404 nm, delayed by 1 ps. (a) PDP spectra at early times, 0.5 ps (green), 1.5 ps (blue), 3.0 ps (purple), 5.0 ps (yellow), and 10 ps (red). (b) PDP spectra at later times, 10 ps (red), 20 ps (yellow), 30 ps (purple), 50 ps (blue), and 300 ps (green).

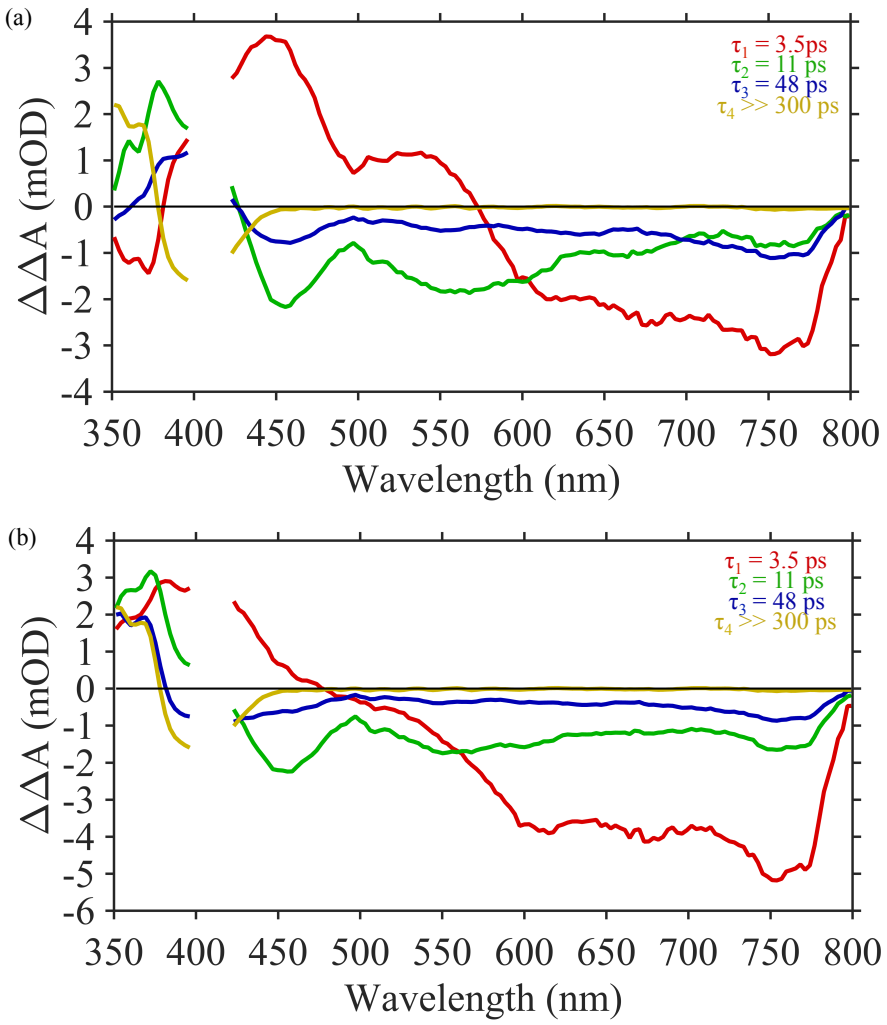

Figure 4.12. Results of global analysis of P-trans PDP data. (a) DADS and (b) SADS, assuming a sequential model. The lifetimes obtained from fitting the data are $\tau_1 = 3.5$ ps. $\tau_2 = 11$ ps, $\tau_3 = 48$ ps, and $\tau_4 >> 300$ ps.

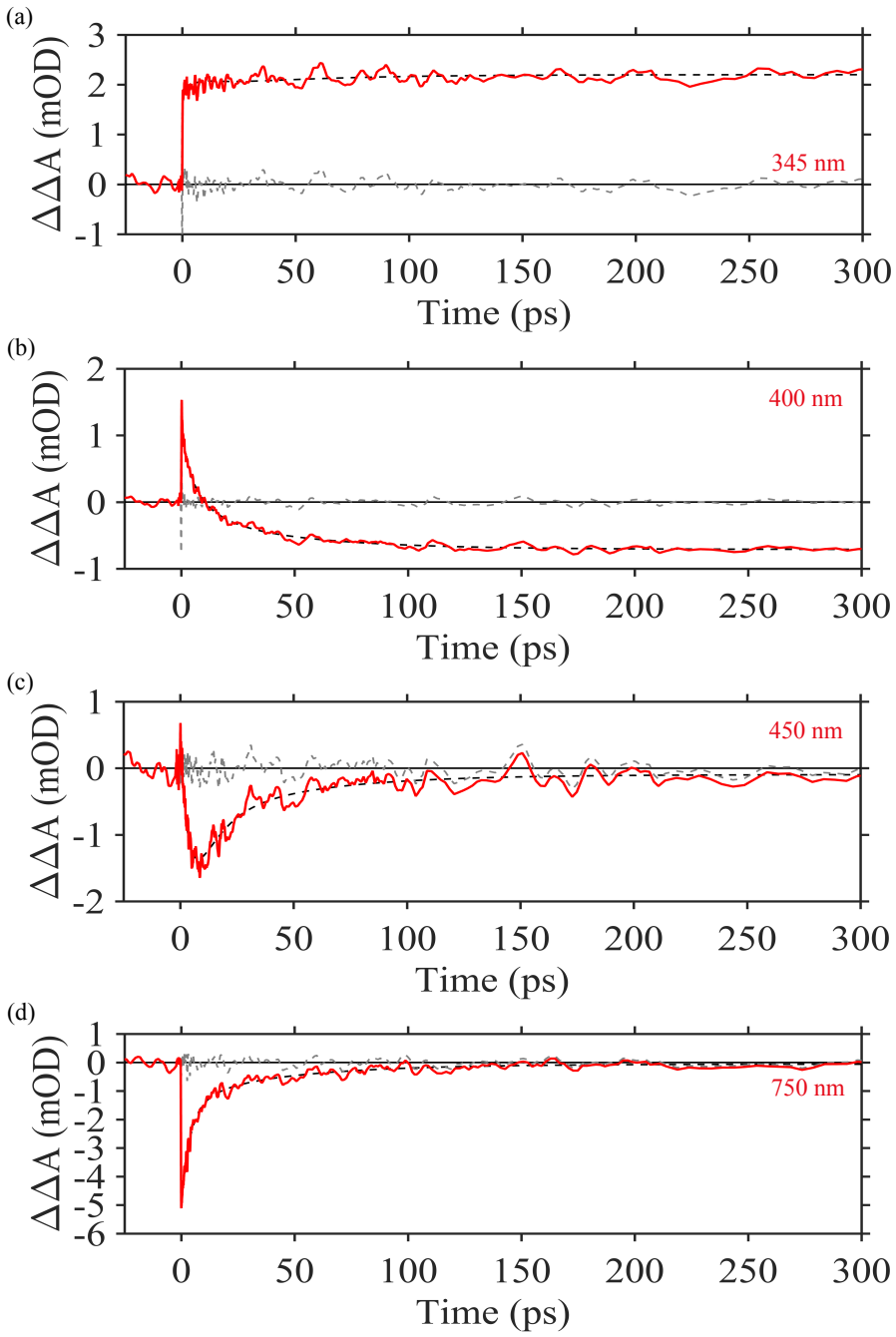

Figure 4.13. P-trans PDP kinetic lineouts (red), fits (black dash), and residuals (grey dash). (a) 345 nm tracks the GSB and depletion of photoproduct signal, (b) 400 nm tracks depletion of SE at early times and depletion of photoproduct at later times, (c) 450 nm tracks the GSB of the intermediate excited state "C", and (d) 750 nm tracks the bleach of the initial excited states "A" and "B."

P-trans – 404 nm repump pulse at 8 ps. 404 nm repump pulses at 8 ps after initial excitation re-excite the sample over the course of its excited state evolution. The 8 ps PrPP spectra are shown in Figure 4.14. At 8 ps after excitation, roughly 10% of the population in the bright "B" state, 60% of the population is in the "C" state, and 30% of the population is the M-cis photoproduct as shown in Figure 4.1b. The 8 ps PrPP data are similar to the PDP spectra in Figure 4.11, and the data are likely dominated by PDP contributions from the bright "B" state. If there are contributions from the "C" state or the M-cis photoproduct, they are difficult to discern. At long times (~ 300 ps), the PrPP spectra resemble bleaching of the M-cis photoproduct signal, in line with the PDP spectra in Figure 4.11.

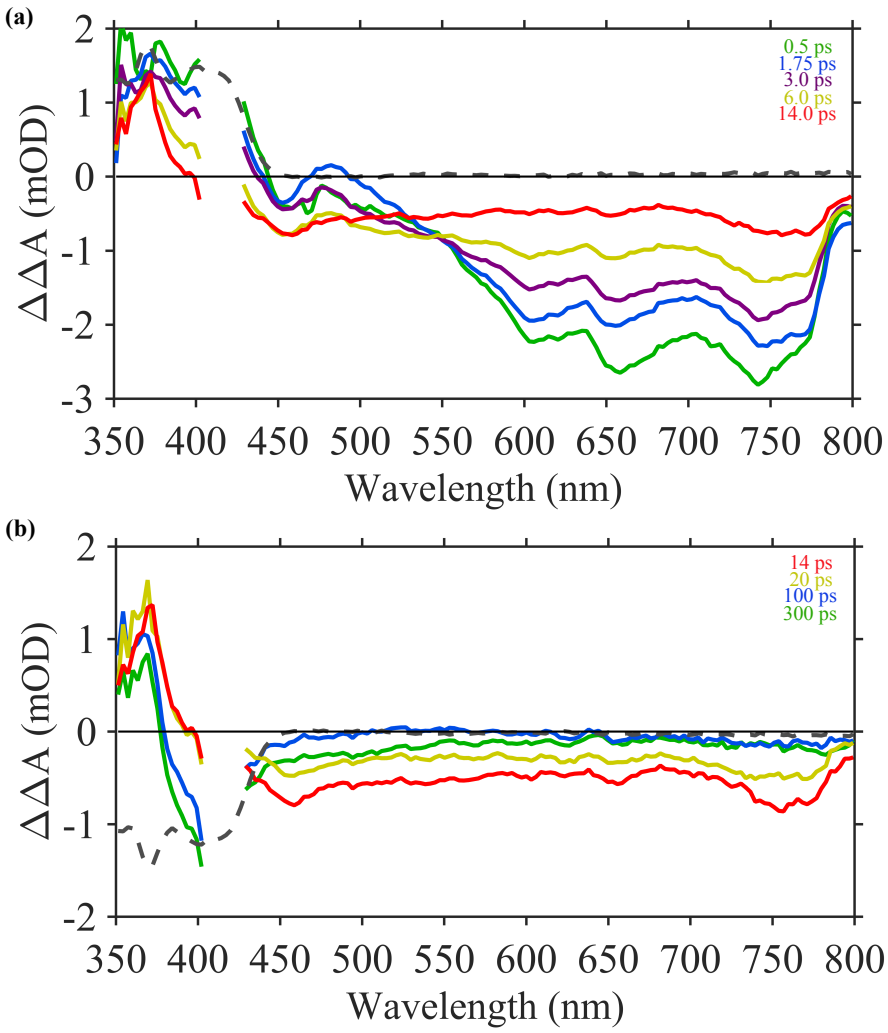

Figure 4.14. P-trans 8 ps PrPP spectra. (a) early times, 0.5 ps (green), 1.75 ps (blue), 3.0 ps (purple), 6.0 ps (yellow), and 14 ps (red). (b) Spectra at later times, 14 ps (red), 20 ps (yellow), 100 ps (blue), and 300 ps (green). M-cis UV-vis (grey dash).

P-trans – 404 nm repump at 65 and 300 ps (M-cis). After repumping the P-trans with 269 nm or 368 nm, M-cis is formed on a ~ 12 ps timescale. However, pumping with 269 nm gives an additional decay component with a ~ 45 ps lifetime and low amplitude across the entire range of the data. PrPP experiments were carried out on M-cis photoproducts with a 404 nm repump pulse at 65 ps and 300 ps. The double difference data are similar in both experiments, thus the ~ 45 ps timescale has a minor effect on the data. Perhaps the ~ 45 ps timescale constitutes a minor

conformational relaxation with little effect on the electronic state or overall dynamics. By 65 ps after excitation, the P-trans sample has completely formed M-cis as shown in Figure 4.1b.

Figure 4.15 shows the PrPP spectra for repumping the P-trans sample at 300 ps and Figure 4.15 shows the 65 ps PrPP spectra. The double difference spectra show a GSB centered around 405 nm, similar to the M-cis UV-vis spectrum. At early times, there is ESA around 700 nm running off of the red side of the spectral window. This ESA decays rapidly along with the SE signal from 550 to 650 nm. As the SE decays, it gives rise to a broad ESA peak, centered at ~ 550 nm. ESA centered at 455 nm appears within the IRF of the experiment, but decays with a longer timescale. At longer times, a double difference photoproduct spectrum forms. Interestingly, the PrPP spectrum indicates formation of photoproducts at long times which are constant for > 300 ps. Within the limited signal to noise and spectral range of the experiment, the photoproduct signal is in agreement with the formation of P-trans.

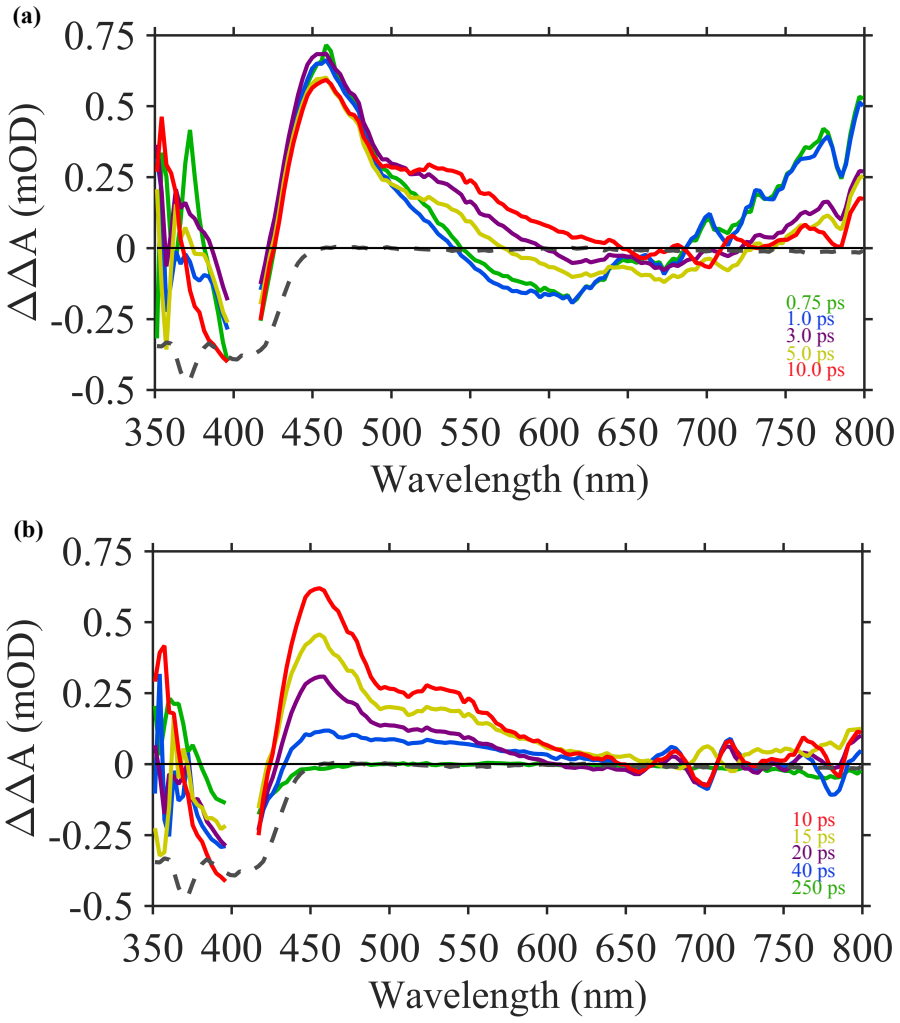

Figure 4.15. PrPP spectra of the M-cis conformer, acquired by repumping P-trans with 404 nm, 300 ps after excitation. (a) Spectra at early times: 0.75 ps (green), 1.0 ps (blue), 3.0 ps (purple), 5.0 ps (yellow),10 ps (red), and grey dash is an inverted UV-vis spectrum of M-cis. (b) Spectra at later times: 10 ps (red), 15 ps (yellow), 20 ps (purple), 40 ps (blue), and 250 ps (green), and grey dash is M-cis UV-vis.

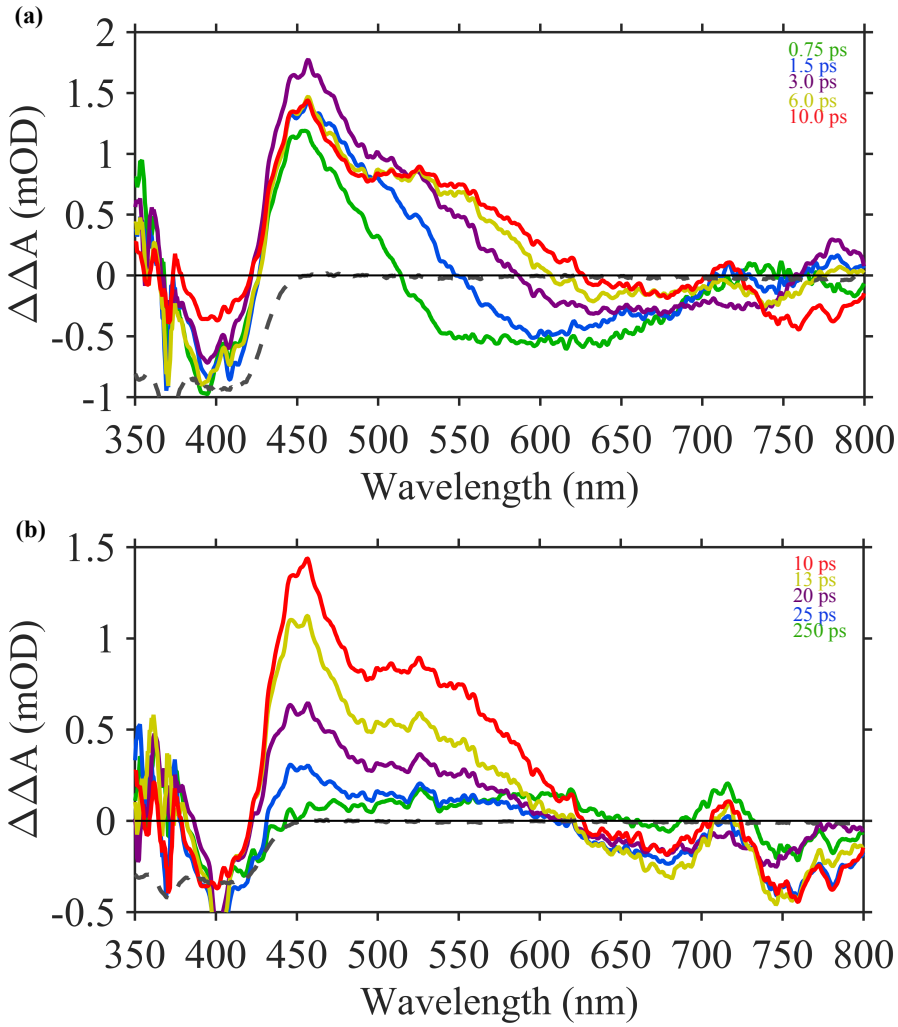

Figure 4.16. PrPP spectra of the M-cis conformer, acquired by repumping P-trans with 404 nm, 65 ps after excitation. (a) Spectra at early times: 0.75 ps (green), 1.0 ps (blue), 3.0 ps (purple), 5.0 ps (yellow),10 ps (red), and grey dash is an inverted UV-vis spectrum of M-cis. (b) Spectra at later times: 10 ps (red), 15 ps (yellow), 20 ps (purple), 40 ps (blue), and 250 ps (green), and grey dash is M-cis UV-vis.

The 300 ps PrPP data were globally fit to a sum of two exponential decay terms and a time independent amplitude. The fit results gave lifetimes of $\tau_1 = 1.2$ ps and $\tau_2 = 20$ ps. Interestingly, the M-cis conformation shows a non-zero quantum yield for isomerization unlike M-trans. The DADS and SADS (assuming a sequential model) are shown in Figure 4.17. Kinetic lineouts showing the quality of the global fit are shown in Figure 4.18.

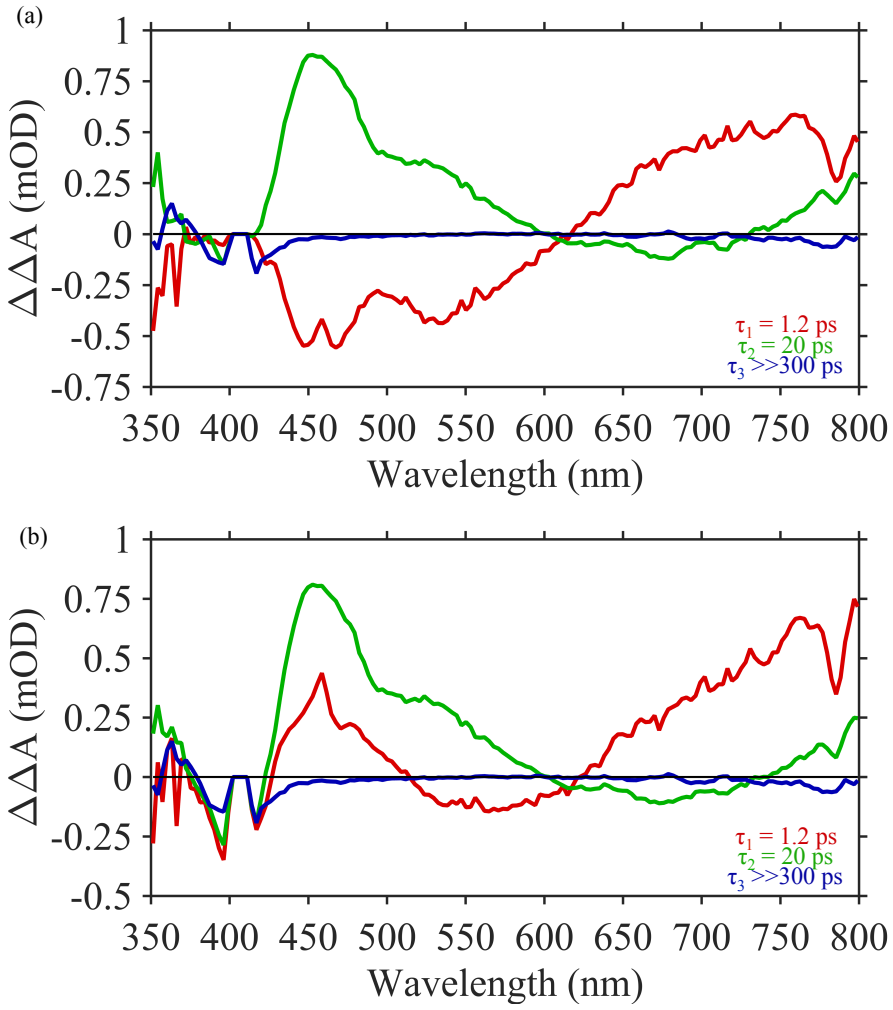

Figure 4.17. Global analysis results of PrPP data acquired by repumping M-cis with 404 nm. (a) DADS and (b) SADS assuming a sequential kinetic model.

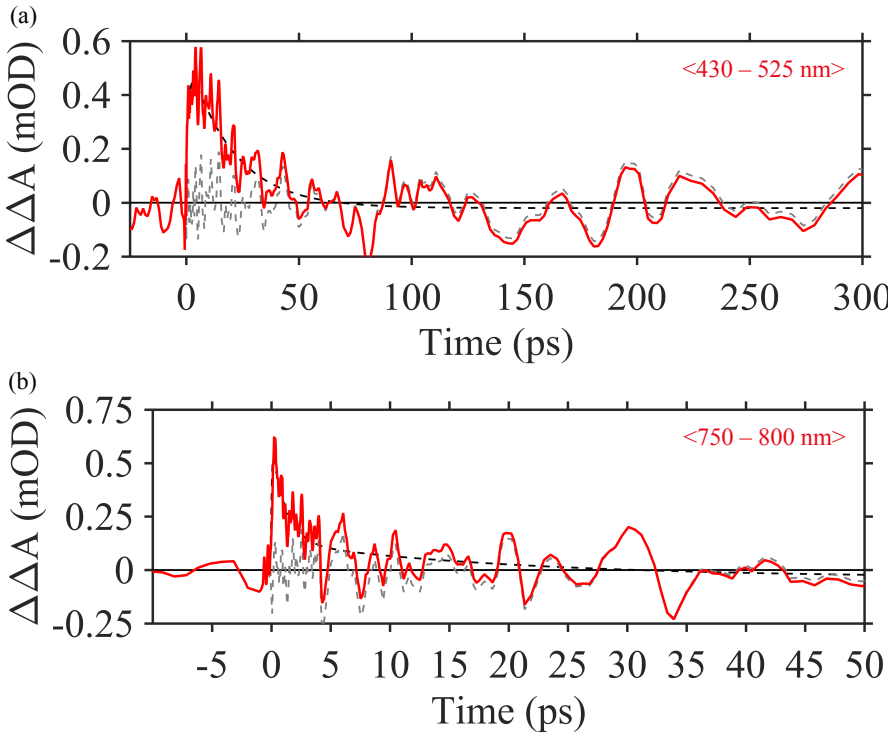

Figure 4.18. Kinetic lineouts of the M-cis PrPP data. (a) signal integrated over the ESA signal from 430 to 525 nm, (b) signal integrated over the ESA signal from 750 to 800 nm. Data shown in red, fits in black dash, and grey dash is residuals.

Discussion

P-trans molecular motor. The PrPP and PDP data on P-trans and its photoproduct (M-cis) give more detailed insight into the photoisomerization of P-trans. The PDP data in Figures 4.2, 4.3, and 4.4 indicate P-trans quickly relaxes to a bright state "A" after excitation with 269 nm. The 404 nm dump pulse depletes the bright excited state "B" in Figure 4.1b giving spectra resembling depleted P-trans TA data. If the PDP data are globally fit, the lifetimes are 3.5 ps, 11 ps, and 48 ps, plus a time independent amplitude corresponding to the steady state difference spectrum of P-trans and M-cis. The global fit results agree with 269 nm excitation TA data. Excitation of P-trans with 269 nm leads to fast relaxation to the same bright state 368 nm excitation produces.

P-trans PrPP data with repump pulse at 8 ps demonstrates the “B” state is also a bright state as shown in Figure 4.14. The PrPP data at 8 ps are dominated by a PDP signal similar to the 1 ps PDP experiment. 8 ps after excitation there ought to be about 10% of the population in the “B” state, which contributes a PDP signal to the data. Unfortunately, global analysis of these data is difficult since they are a mixture of “B”, “C”, and M-cis.

The P-trans PrPP data with the repump pulse at 65 ps and 300 ps probing the M-cis photoproducts give similar results. This indicates M-cis forms on an 11 ps timescale. The 45 ps timescale observed in the 269 nm excitation data is likely a minor conformational relaxation with little effect on the electronic state or overall dynamics. Interestingly, M-cis forms P-trans after excitation with 404 nm. This is clear if one compares the long time PrPP difference spectrum of M-cis to the long time difference spectrum of P-trans as shown in Figure 4.19. The M-trans photoproduct signal from the PrPP data multiplied by an arbitrary scale factor is in good agreement with the P-trans photoproduct signal from TA data.

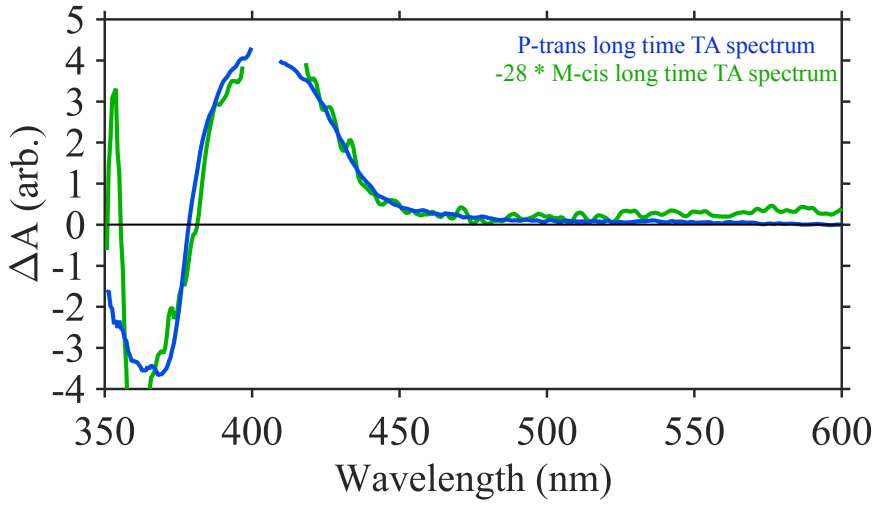

Figure 4.19. Comparison of P-trans photoproduct difference spectrum (blue) from TA and -28*M-cis photoproduct difference spectrum (green) from PrPP.

If one considers the low temperature photolysis of P-trans in Chapter three Figure 3.1, the M-cis spectrum appears to have traces of residual P-trans. The two vibronic peaks of P-trans at 368 and 352 nm are still present in the M-cis spectrum. If the peaks at 352 nm and 368 nm are signatures of residual P-trans, then the sample is likely forming a photostationary state between P-trans and M-cis. Taken together with the TA and PrPP data in Figure 4.19, it is likely that P-trans and M-cis form their respective photoproducts through the same conical intersection. Figure 4.20 shows a scheme for the excited states of P-trans and M-cis.

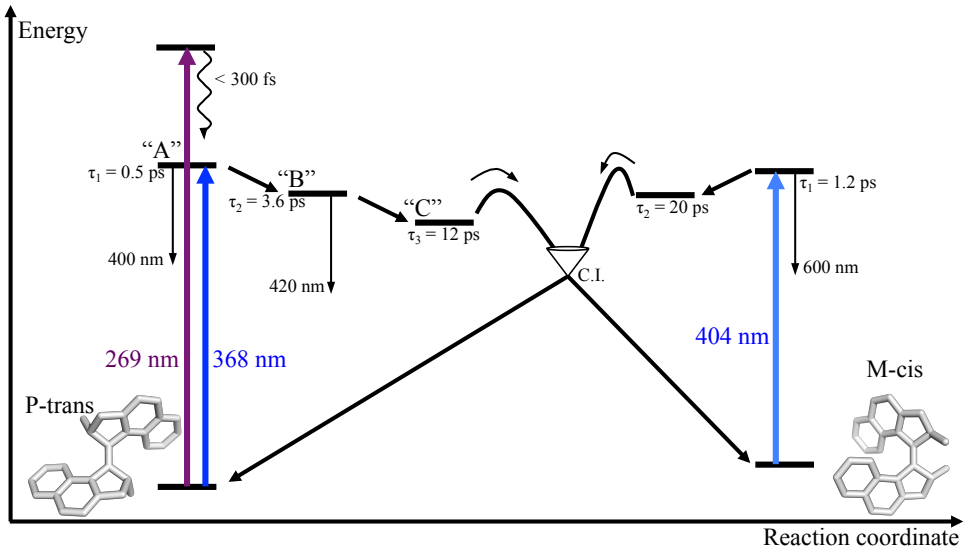

Figure 4.20. Scheme depicting the excited state dynamics of P-trans and M-cis. (*left hand side*) Excitation of P-trans with 269 nm produces a highly excited state, which quickly relaxes to the "A" state. Excitation of P-trans with 368 nm populates the "A" state, which relaxes from the Franck Condon region on a 500 fs timescale forming the "B" state. The "B" state relaxes to the "C" state on a 3.6 ps timescale, and the "C" reaches a conical intersection (CI) branching between P-trans and M-cis on a 12 ps timescale. (*right hand side*) Excitation of M-trans populates a bright state, which relaxes to form a dark state on a 1.2 timescale. The dark state reaches the same CI branching between P-trans and M-cis a on a 20 ps timescale.

P-cis molecular motor. PDP and PrPP data for P-cis give important details into the excited states of P-cis and M-trans. Unfortunately, the P-cis PDP and PrPP data are complicated by the P-cis ground state absorption of the repump. This leads to the need for a scale factor α when subtracting the repump background signal when calculating the double difference signal. The 1 ps PDP data indicate fast relaxation to the "A" state of P-cis because a 404 nm dump pulse depletes excited states giving spectra with timescales similar to P-cis TA data. The 10 ps PrPP data show the depletion of spectroscopically similar excited states to the excited state of M-trans. The 10 ps PrPP data in Figures 4.5, 4.6, and 4.7 show depletion of excited states spectroscopically similar to M-trans excited states. However, global analysis of the PrPP shows the lifetimes of these excited states are not the same as M-trans. The intermediate's spectra are similar to M-trans TA spectra, but the intermediate could be in different a conformation. This could explain the similar spectra and different lifetimes. The 300 ps PrPP data probed the TA of M-trans, confirming M-trans is present in equilibrium with P-trans in solution at room temperature. The 300 ps PrPP data agree with 404 nm excitation TA of M-trans shown in Chapter three Figure 3.14.

Low temperature photolysis of P-cis produces M-trans completely. In addition, the quantum yield for photoisomerization of M-trans is zero or below the signal to noise of TA experiments. Unless P-cis has a quantum yield of unity, there must be two conical intersections involved in the photoisomerization of P-cis. The first conical intersection P-cis encounters determines the overall quantum yield of the reaction, and the excited states branch between this pathway or going on to the next conical intersection. The second conical intersection produces M-trans with unit quantum yield. This conical intersection is responsible for the zero quantum yield for M-trans. A scheme for the photoisomerization of P-cis and M-trans is shown in Figure 4.21.

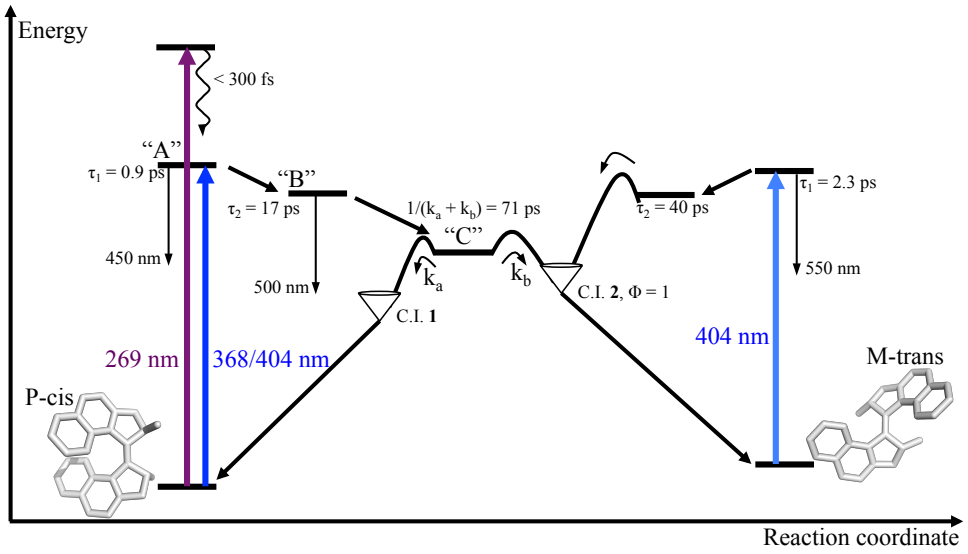

Figure 4.21. Scheme depicting the excited state dynamics of P-cis and M-trans. (*left hand side*) Excitation of P-cis with 269 nm produces a highly excited state, which relaxes to the "A" state quickly. "A" is a bright state, which decays to "B" another bright state, on a 0.9 ps timescale. "B" relaxes to a dark state "C" on a 17 ps timescale. At "C" there is branching between two pathways with separate conical intersections CI 1 and CI 2 with two rates k_a and k_b, whose sum is 1/(71 ps). CI 1 leads to recovery of P-cis while CI 2 leads to formation of M-trans with unit quantum yield. (*right hand side*) A small population of M-trans exists in equilibrium with P-trans in solution. M-trans absorbs 404 nm while P-trans does not. Excitation by 404 nm puts M-trans in a bright excited state with a lifetime of 2.3 ps. This state forms a dark excited state with a 40 ps lifetime reaching CI 2 to form M-trans with unit quantum yield.

Conclusions

Overall, the TA studies in Chapter three and the re8sults presented in this Chapter demonstrate two different excited state reactions paths for P-cis and P-trans. In the case of P-trans forming M-cis, there is one conical intersection through which P-trans forms M-cis and through which M-cis forms P-trans, as shown in Figure 4.20. This is demonstrated by two key findings: (1) PrPP of M-cis produces a long time photoproduct spectrum that is in good agreement with the difference between P-trans and M-cis, and (2) Low temperature photolysis of

P-trans produces a photostationary state of P-trans and M-cis. These findings indicate M-cis is photoactive and excitation of M-cis produces P-trans. On the other hand, the excited state pathway connected P-cis to M-trans has two conical intersections, supported by (1) TA of P-cis, (2) TA and PrPP of M-trans, and (3) low temperature photolysis of P-cis. It is clear from TA of P-cis that M-trans is the photoproduct. However, M-trans shows no long time photoproduct signal in either TA or PrPP. Low temperature photolysis completely converts P-cis to M-trans. These results demonstrate M-trans is not photoactive. Unless P-cis has an isomerization quantum yield of unity, there is likely a second nonproductive conical intersection involved in the isomerization of P-cis as shown in Figure 4.21. Since M-trans is not photoactive, P-cis can be fully converted to M-trans in steady state photolysis.

These results are useful for the design of future more efficient molecular motors. The excited state pathway for P-cis possesses a conical intersection with unity quantum yield for forming M-trans, whereas P-trans and M-cis branch between each other. The P-trans/M-cis scheme puts limits on the overall efficiency and unidirectionality of the molecular motor. Identifying the structural and electronic factors governing the two schemes will allow future molecular designs to incorporate more efficient and directional conical intersections.

Notes on Chapter 4

(1) Van Stokkum, I. H. M.; Larsen, D. S.; Van Grondelle, R. *Biochim. Biophys. Acta - Bioenerg.* **2004**, *1657* (2–3), 82–104.

(2) Papagiannakis, E.; Vengris, M.; Larsen, D. S.; Van Stokkum, I. H. M.; Hiller, R. G.; Van Grondelle, R. *J. Phys. Chem. B* **2006**, *110* (1), 512–521.

(3) Ward, C. L.; Elles, C. G. *J. Phys. Chem. Lett.* **2012**, *3* (20), 2995–3000.

(4) Ward, C. L.; Elles, C. G. *J. Phys. Chem. A* **2014**, *118* (43), 10011–10019.

(5) Nuernberger, P.; Ruetzel, S.; Brixner, T. *Angew. Chemie - Int. Ed.* **2015**, *54* (39), 11368–11386.

(6) Bradler, M.; Werhahn, J. C.; Hutzler, D.; Fuhrmann, S.; Riedle, E.; Iglev, H.; Kienberger, R.; Optik, B.; Heider, R.; Riedle, E.; Iglev, H.; Kienberger, R. *Osa* **2013**, *21* (17), 7261–7271.

(7) Redeckas, K.; Voiciuk, V.; Steponaviciute, R.; Martynaitis, V.; Sackus, A.; Vengris, M. *J. Phys. Chem. A* **2014**, *118* (30), 5642–5651.

(8) Fitzpatrick, A. E.; Lincoln, C. N.; Wilderen, L. J. G. W. Van; Thor, J. J. Van. *J. Phys. Chem. B* **2012**, *116* (3), 1077–1088.

(9) Buback, J.; Kullmann, M.; Langhojer, F.; Nuernberger, P.; Schmidt, R.; Würthner, F.; Brixner, T. *J. Am. Chem. Soc.* **2010**, *132* (46), 16510–16519.

(10) Conyard, J.; Addison, K.; Heisler, I.; Cnossen, A.; Browne, W. R.; Feringa, B. L.; Meech, S. R. *Nat. Chem.* **2012**, *4* (7), 547–551.

(11) Conyard, J.; Cnossen, A.; Browne, W. R.; Feringa, B. L.; Meech, S. R. *J. Am. Chem. Soc.* **2014**, *136* (27), 9692–9700.

(12) Amirjalayer, S.; Cnossen, A.; Browne, W. R.; Feringa, B. L.; Buma, W. J.; Woutersen, S. *J. Phys. Chem. A* **2016**, *120* (43), 8606–8612.

(13) Conyard, J.; Stacko, P.; Chen, J.; McDonagh, S.; Hall, C. R.; Laptenok, S. P.; Browne, W. R.; Feringa, B. L.; Meech, S. R. *J. Phys. Chem. A* **2017**, *121* (10), 2138–2150.

(14) Augulis, R.; Klok, M.; Feringa, B. L.; Van Loosdrecht, P. H. M. *Phys. Status Solidi Curr. Top. Solid State Phys.* **2009**, *6* (1), 181–184.

(15) van Delden, R. A.; ter Wiel, M. K. J.; Pollard, M. M.; Vicario, J.; Koumura, N.; Feringa, B. L. *Nature* **2005**, *437* (7063), 1337–1340.

(16) Chiang, P. T.; Mielke, J.; Godoy, J.; Guerrero, J. M.; Alemany, L. B.; Villagómez, C. J.; Saywell, A.; Grill, L.; Tour, J. M. *ACS Nano* **2012**, *6* (1), 592–597.

(17) Chu, P. L. E.; Wang, L. Y.; Khatua, S.; Kolomeisky, A. B.; Link, S.; Tour, J. M. *ACS Nano* **2013**, *7* (1), 35–41.

(18) Garcia-Lopez, V.; Chiang, P. T.; Chen, F.; Ruan, G.; Martin, A. A.; Kolomeisky, A. B.; Wang, G.; Tour, J. M. *Nano Lett.* **2015**, *15* (12), 8229–8239.

(19) Garcia-Lopez, V.; Jeffet, J.; Kuwahara, S.; Martin, A. A.; Ebenstein, Y.; Tour, J. M. *Org. Lett.* **2016**, *18* (10), 2343–2346.

(20) Feringa, B. L. *J. Org. Chem.* **2007**, *72* (18), 6635–6652.

(21) Klok, M.; Browne, W. R.; Feringa, B. L. *Phys. Chem. Chem. Phys.* **2009**, *11* (40), 9124–9131.

Chapter 5

Photochromic photoacids

The photochromic properties of spiropyran have long been utilized for light activated molecular devices[1]. Irradiation of spiropyran causes reversible ring opening to form merocyanine. Likewise, merocyanine can reversibly ring close to form spiropyran. These two species are chemically and spectroscopically distinct[2,3]. As a result, spiropyran has inspired technology ranging from optical data storage[4,5], photoswitchable hydrophobic coatings and membranes[6–9], light controlled fuel cells[10], to DNA photoswitches[11,12]. More recently, water-soluble spiropyran derivatives have garnered interest as photochromic photoacids[13–15].

Here we report an ultrafast spectroscopic study of two different merocyanine/spiropyran (MC/SP) photochromic switches that experience a large drop in pKa after photoexcitation[13–17], **2-[(E)-2-(2-hydroxyphenyl)ethenyl]-3,3-dimethyl-1-(3-sulfopropyl)-3H-indol-1-ium** "phenylhydroxy-MCH" and **2-[(E)-2-(1H-indazol-7-yl)ethenyl]-3-(3-sulfopropyl)-1,3-benzothiazol-3-ium** "indazole-MCH". The purpose of the following transient absorption (TA) investigations was to examine the role of solvent in the formation of photoproducts. Figure 5.1 contains the structures and absorption spectra of phenylhydroxy-MCH and indazole-MCH as well as their respective spiropyran forms.

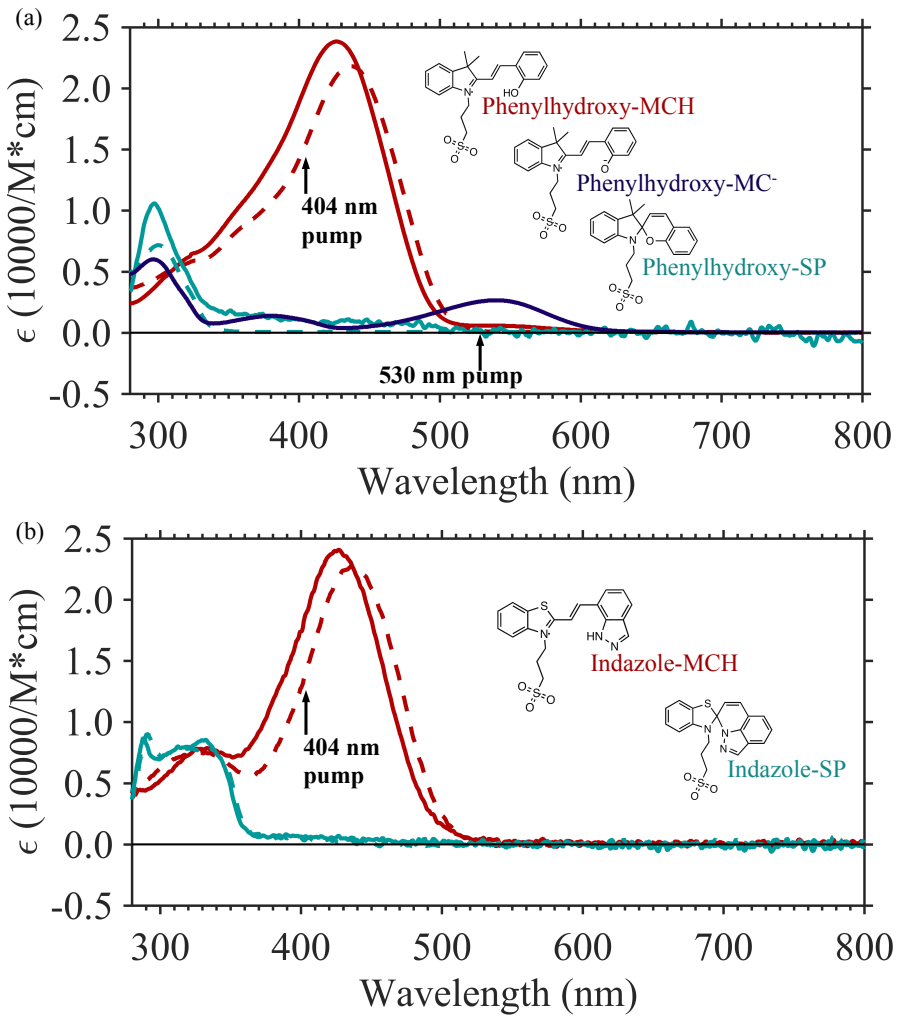

Figure 5.1. (a) Phenylhydroxy-MCH UV-vis in aqueous solution buffered at 5 (red, solid) and DMSO (red, dash), phenylhydroxy-MC$^-$ in aqueous solution buffered at pH 10 (dark blue), and phenylhydroxy-SP in aqueous solution buffer at pH 5 (light blue, solid) and DMSO (light blue, dash). (b) Indazole-MCH UV-vis in aqueous solution buffered at pH 7.4 (red, solid) and DMSO (red, dash), and indazole-SP in aqueous solution buffered at pH 7.4 (light blue, solid) and DMSO (light blue, dashed). TA pump wavelengths marked with black arrows.

Here the photochemical formation of the spiropyran form by isomerization and ring closure of the ring open merocyanine form has been investigated by ultrafast transient absorption in the UV-visible region. The results are compared with theoretical simulations performed using DFT and TDDFT methods. The key findings from this study show photoexcitation of the indazole-MCH produces a long-lived photoproduct on a timescale of ~ 30 ps, consistent with formation of indazole-SP. This reaction occurs both in phosphate buffered saline (PBS) solution at pH 7.4 and in dimethylsulfoxide (DMSO). In contrast, the TA results for the phenylhydroxy-MCH are solvent dependent. In pH 5.5 citrate buffer, a long-lived *ring-open* photoproduct forms on a ~ 10 ps timescale and persist for >> 3.5 ns. In steady state photolysis of phenylhydroxy-MCH, phenylhydroxy-SP forms relatively promptly in ≤ 1 second. TDDFT calculations support the assignment of this long-lived species to a deprotonated *cis* isomer of the phenylhydroxy-MC$^-$. In DMSO, the phenylhydroxy-MCH forms a long-lived photoproduct on ~ 50 ps timescale which persists for >> 3.5 ns, consistent with the formation of either phenylhydroxy-SP or a *protonated cis*-phenylhydroxy-MCH.

Sample Handling

Prof. Yi Liao's group synthesized phenylhydroxy-MCH[13,14] and indazole-MCH[15] and generously shared the samples. The phenol group of the phenylhydroxy-MCH has a pKa of about 7.8. Buffers were used to maintain ~ 99% phenylhydroxy-MCH or ~ 99% phenylhydroxy-MC$^-$. Experiments were either carried out in 11 mM pH 5.5 aqueous citrate buffer (for phenylhydroxy-MCH), 11 mM pH 10 aqueous carbonate buffer (for phenylhydroxy-MC$^-$), 11 mM pH 7.4 phosphate buffer saline (for indazole-MCH), or in DMSO (for phenylhydroxy-MCH and indazole-MCH)[13–16]. Solids were sonicated in 2 mL DMSO for one minute, and then 18 mL of aqueous buffer (either citrate, phosphate buffered saline, or

carbonate, depending on the experiment) was added to the solution. The reagents used in these experiments were obtained from Sigma-Aldrich and used without further purification. The solutions were prepared to have an OD between 0.3 and 1.0 in a 1 mm cuvette at the pump wavelength of the TA experiment (either 404 or 530 nm). The following TA experiments were conducted at ~ 19° C using a 404 nm pump pulse or a 530 nm pump pulse and a continuum probe ranging from either ~ 350 – 800 nm or ~ 260 – 600 nm. All TA measurements were carried out holding the pump polarization at magic angle (54.7°) with respect to the probe. Time points and step sizes similar to those in Chapter three Table 3.1 were chosen. UV-vis spectra of the samples were collected at one hour intervals during the course of an experiment to monitor the build-up of photoproducts.

Computational Methods

Density functional theory calculations were performed using the Q-CHEM suite of packages[18]. Geometry optimizations of all 9 conformations (SP, TTC, TTT, CTC, CTT, CCC, TCT, CCT, and TCC) of each photoacid and their conjugate base were performed with the B3LYP/6-311G** level of theory in combination with the integral equation formalism polarizable continuum model (IEF-PCM)[19–21]. The IEF-PCM calculations used the dielectric constant of water (n = 80.4) and the default Bondi radii multiplied by 1.2. The propyl sulfonate group of the photoacids was truncated with a methyl group to facilitate geometry optimization because, besides increasing the water solubility of the merocyanine moieties, it does not significantly affect the photophysics or reaction mechanism. Explicit water solvent molecules were also included, when specified, to account for the local solvation effects of the hydrogen bond[22].

Vibrational frequency analyses in the harmonic approximation were performed at the same level of theory, and thermochemical data were evaluated at 298 K. The existence of the stationary points was checked by inspection of the Hessian matrix eigenvalues. All geometries were stationary points except: CCT-indazole-MC$^-$, TCC-indazole-MC$^-$, TCT-indazole-MC$^-$, CTC-indazole-MC$^-$, CTT-indazole-MC$^-$, TTT-indazole-MC$^-$, and TCT-phenylhydroxy-MC$^-$, even after re-optimization with the exact Hessian. However, the imaginary frequencies of the final geometry were small, and only TCT-phenylhydroxy-MC$^-$ is relevant to the conclusions presented.

Vertical excitations were calculated at the optimized geometries using time dependent density functional theory (TDDFT) within the Tamm-Damcoff approximation and the B3LYP/6-311G** level of theory[23]. The non-equilibrium solvation of the excited states was taken into account using the state specific (SS) and linear response (LR) approaches[24].

The transition state between CCC-phenylhydroxy-MC$^-$ and phenylhydroxy-SP was located with the growing string method (GSM) at the B3LYP/6-31G** level of theory in vacuum[25,26]. The thermochemical data for the critical points was evaluated at the IEF-PCM (n = 80.4) B3LYP/6-311G** level of theory, at 298 K.

Results

Steady state photolysis. In the case of the phenylhydroxy-MCH in buffer or DMSO, irradiation promptly produces the ring-closed spiropyran (phenylhydroxy-SP). The UV-vis spectrum of phenylhydroxy-SP shows a prominent peak at ~ 293 nm and no absorption at wavelengths longer than 300 nm as shown in Figure 5.1a. If left in the dark, the sample reverts to phenylhydroxy-MCH as demonstrated by formation of the phenylhydroxy-MCH spectrum. The

same is true for the indazole-MCH. Irradiation of the indazole-MCH form, in either aqueous buffer or DMSO, promptly produces the indazole-SP. Indazole-SP absorbs at ~ 325 nm with no absorptions at wavelengths greater than 350 nm as shown in Figure 5.1b. The indazole-SP also reverts to indazole-MCH if left in the dark. Finally, the phenylhydroxy-MC^- in carbonate buffer produces no detectable phenylhydroxy-SP^- formation after irradiation with a 450 W Xe arc lamp.

Phenylhydroxy-MCH in citrate buffer. The UV-vis TA spectra of the phenylhydroxy-MCH in Figure 5.2 were measured after excitation with 404 nm. The GSB is centered at ~ 425 nm and only approximately matches the UV-vis absorption. Stimulated emission (SE) is featured from 540 – 750 nm and excited state absorption (ESA) appears at 290, 375, and 480 nm. At ~ 50 ps, peaks at 500 and 560 nm corresponding to photoproducts grow in and remain constant for the next 3.5 ns. The 430 nm GSB amplitude increases at early times, reaches a maximum amplitude at ~ 1 ps, decreases in amplitude on a longer timescale, and reaches a constant value by 10 ps. The early changes in the GSB could be a result of fast decay of overlapping ESA and subsequent slow rise of overlapping photoproduct signals. ESA at 375 nm appears within the instrument response (IRF, ~ 150 fs) of the experiment and decays within 2 ps. The 375 nm ESA eventually reaches a steady state with a negative value, which is accounted for by residual GSB. The blue and red extremes of the SE signal, ~ 575 and 750 nm, appear within the IRF, while a portion at ~ 675 nm grows in from 0.5 to 3.0 ps. There is likely an overlapping ESA at 675 nm responsible for this apparent growth of SE. ESA at 480 nm grows in to a maximum around 1.75 ps, and decays to a steady state by 50 ps. The steady state photoproduct spectrum has a residual GSB as well as photoproduct absorption peak on the red side of the GSB, at ~ 475 – 600 nm, which persists for 3.5 ns.

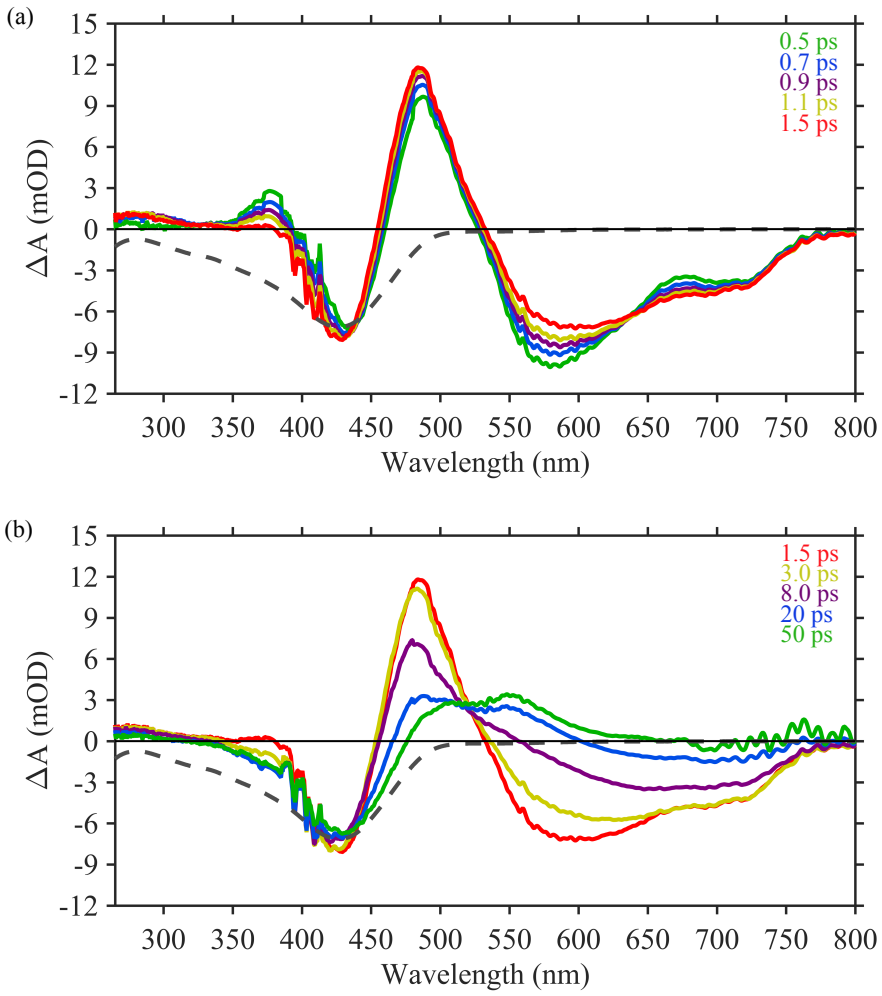

Figure 5.2. (a) TA spectra of phenylhydroxy-MCH at 0.5 ps (green), 0.7 ps (blue), 0.9 ps (purple), 1.1 ps (yellow), 1.5 ps (red), and scaled UV-vis of phenylhydroxy-MCH (grey dash). (a) TA spectra of phenylhydroxy-MCH at 1.5 ps (red), 3.0 ps (yellow), 8.0 ps (purple), 20 ps (blue) and 50 ps (green), scaled UV-vis of phenylhydroxy-MCH (grey dash).

The phenylhydroxy-MCH TA data are best globally fit with a sum of three exponential decays and corresponding amplitudes and an additional amplitude to account for the long-lived signal of the photoproduct as shown in Table 5.1. The lifetimes obtained from the fit are τ_1 = 630 fs, τ_2 = 3.3 ps, and τ_3 = 10 ps. The wavelength dependent amplitudes of each decay term

in the global fit ("Decay Associated Difference Spectra", DADS) are plotted in Figure 5.3. Assuming a particular kinetic model, such as A* → B → C → photoproduct, one can transform the DADS into species associated difference spectra or SADS. The details of this transformation are given in Chapter 2 Methods. Kinetic lineouts demonstrating the necessity of the three rate constants are shown in Figure 5.4.

Table 5.1. Global fitting results of Phenylhydroxy-MCH and indazole-MCH in aqueous citrate buffer and anhydrous DMSO.

Phenylhydroxy-MCH	$\tau_{1\ (ps)}$	$\tau_{2\ (ps)}$	$\tau_{3\ (ps)}$	$\tau_{4\ (ps)}$	$\tau_{5\ (ns)}$
Citrate Buffer pH 5.5	0.63	3.3	10		>>3.5
DMSO	1.2	5.5	49	~1800	>>3.5
Indazole-MCH					
Phosphate Buffer pH 7.4	1.2		23	127	>>3.5
DMSO	0.31	3.1	28	128	>>3.5

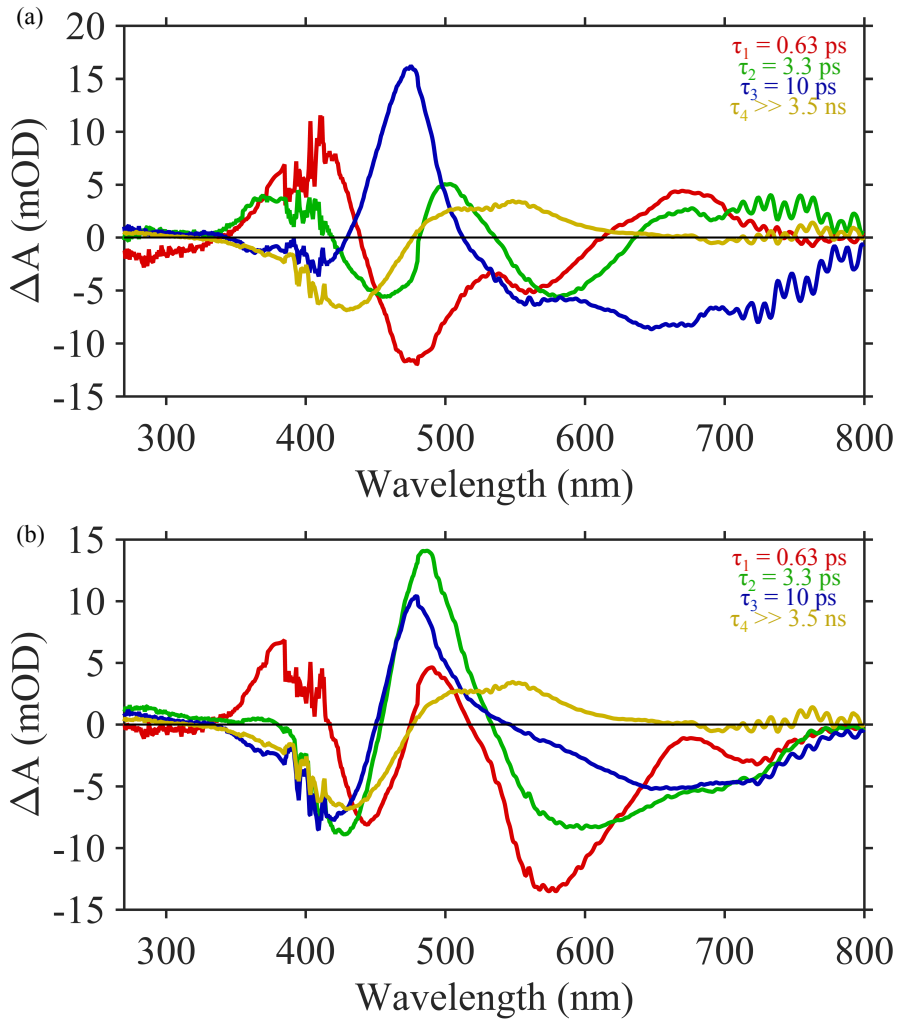

Figure 5.3 (a) Decay associated difference spectra (DADS) of phenylhydroxy-MCH in citrate buffer, (b) Species associated difference spectra (SADS) of phenylhydroxy-MCH assuming a sequential model.

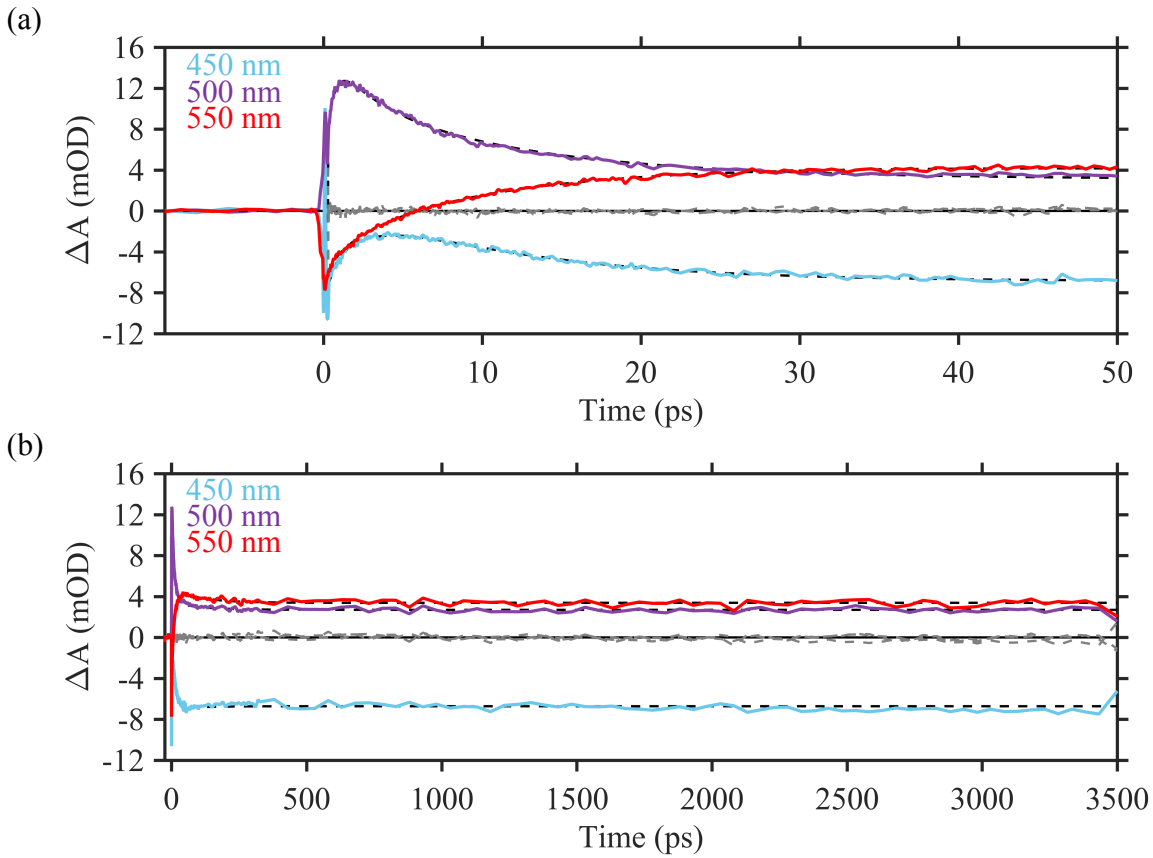

Figure 5.4. Kinetic lineouts of phenylhydroxy-MCH in 11 mM pH 5.5 citrate buffer after 404 nm excitation, data in color, fit is black dash, residuals in grey. 450 nm in blue, 500 nm in purple, 550 nm in red. (a) Early times from 0 to 50 ps, (b) all times from 0 to 3500 ps.

Indazole-MCH in buffer. The indazole-MCH was investigated with TA, steady state photolysis, and DFT in aqueous buffer and DMSO. The pKa of indazole-MCH is ~ 10, so the sample was prepared in pH 7.4 PBS solution with ~ 5% (v/v) DMSO, favoring the acidic form. The data were collected with a UV continuum (260 – 600 nm) and a visible continuum (350 – 800 nm) and combined into one dataset. The UV continuum data was scaled by a constant factor of 0.22 to match the intensities of the signals in the visible continuum data.

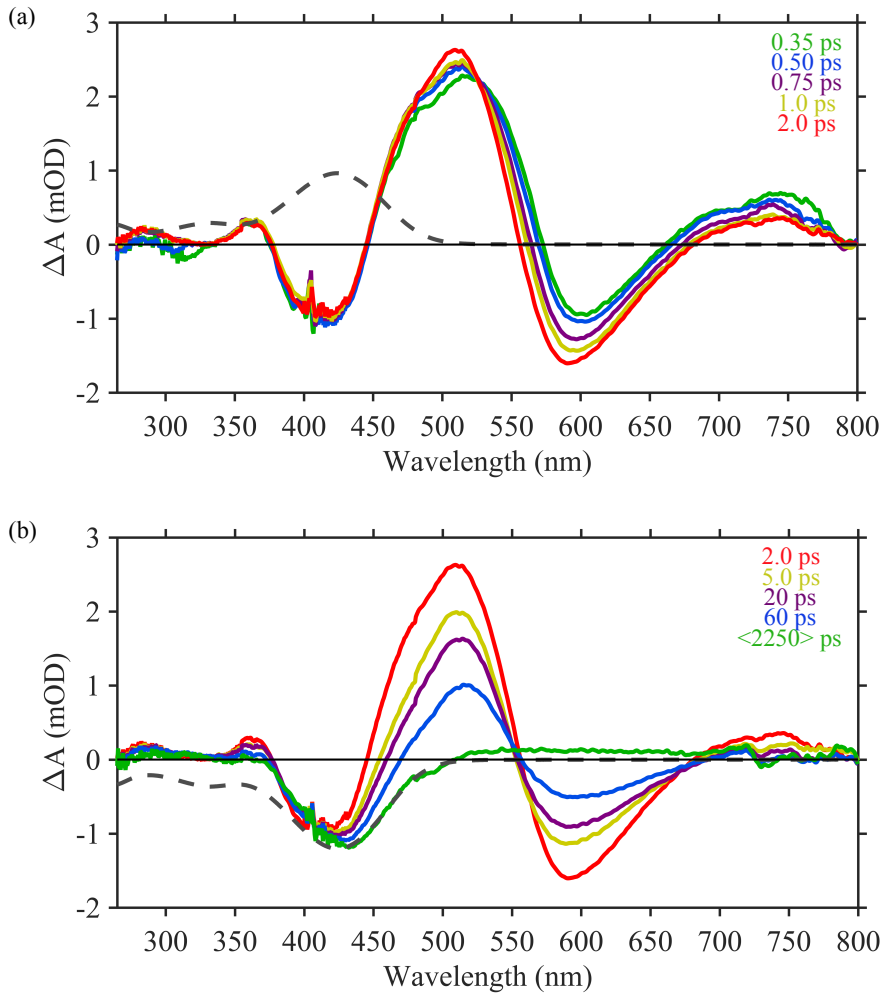

Figure 5.5. (a) TA spectra of indazole-MCH at 350 fs (green), 500 fs (blue), 750 fs (purple), 1.0 ps (yellow) and 2.0 ps (red), scaled UV-vis of indazole-MCH (grey dash). (b) TA spectra of indazole-MCH at 2.0 ps (red), 5.0 ps (yellow), 20 ps (purple), 60 ps (blue) and averaged from 1 – 3.5 ns (green), scaled UV-vis of indazole-MCH (grey dash). Spectra are a result of combining two datasets, one using a visible probe (~350 – 800 nm) and one using a UV probe (~270 – 600 nm). The UV continuum dataset was scaled by 0.22 to match the intensities of the visible dataset.

The TA spectra in Figure 5.5 show a GSB centered on 420 nm, SE ranging from 550 – 670 nm, and ESA in several areas: 350 – 360 nm, 450 – 550 nm, and 670 – 800 nm. The GSB

appears within IRF (~ 80 fs). The GSB recovers slightly on a ~ 1 ps timescale, probably due to an overlapping ESA that decays quickly. The GSB remains a constant value for the subsequent ~ 3.5 ns, indicating near unit quantum yield for the conversion of the indazole-MCH to a long-lived photoproduct as seen in Figure 5.5. There is a weak positive absorption peak at ~ 525 nm that persists for ~ 3.5 ns.

The indazole-MCH TA data in PBS are best globally fit with a sum of three exponential decays and corresponding amplitudes as well as an additional time independent amplitude. The fit of the data was started at 0.5 ps to avoid complications caused by coherent signals such as two photon absorption, stimulated Raman scattering, and cross-phase modulation. The global fitting results gave τ_1 = 1.2 ps, τ_2 = 23 ps, τ_3 = 127 ps, τ_4 >> 3.5 ns. Kinetic lineouts with fits and residuals at 440, 525, and 585 nm shown in Figure 5.6 demonstrate quality of the analysis. DADS constructed from the amplitudes of the terms in the fit are plotted in Figure 5.7. The DADS are transformed into SADS for a sequential kinetic model (A* → B → C → photoproduct) and are plotted in Figure 5.7.

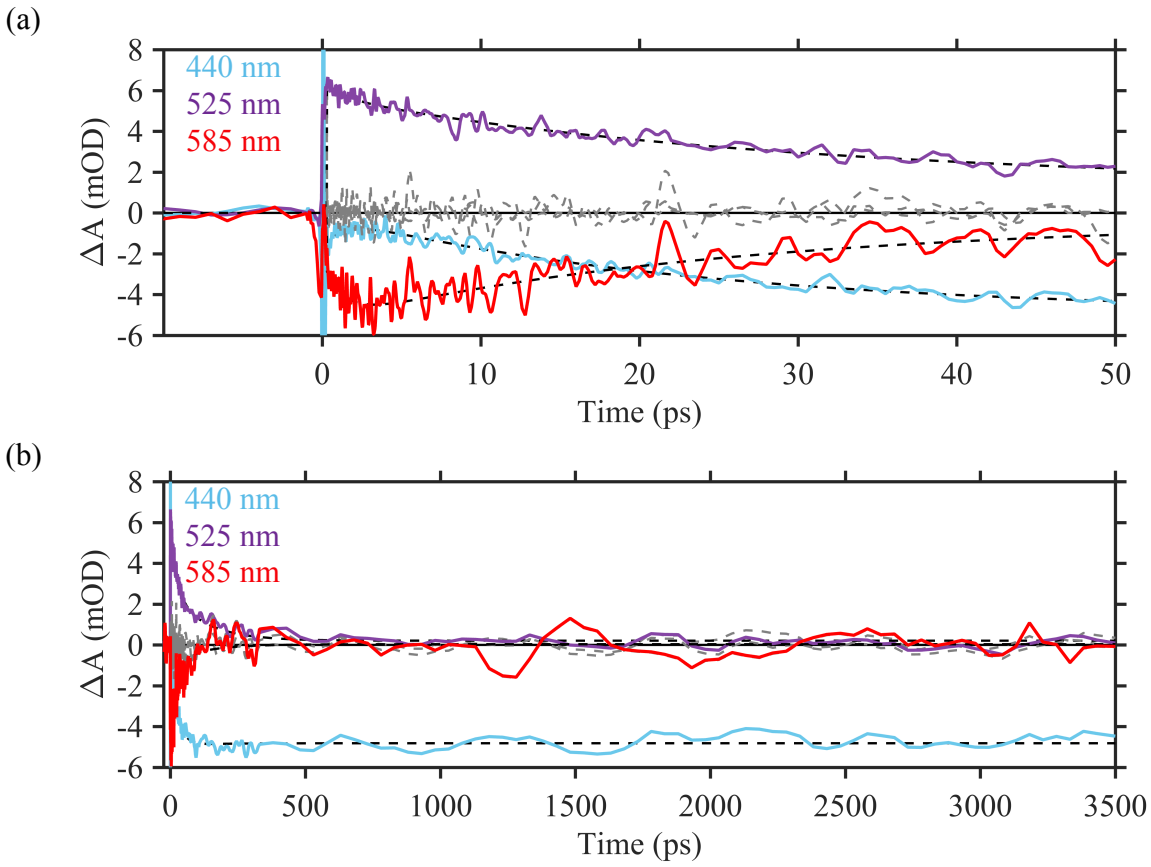

Figure 5.6. Kinetic lineouts of indazole-MCH at select wavelengths in PBS after excitation with 404 nm. Colorful traces are the measured data, dashed lines are the fits, and the grey lines are residuals. 440 nm tracks the GSB in blue, 525 nm tracks the ESA in purple, 585 nm track the SE in red. (a) Early times from 0 to 50 ps, (b) all time delays from 0 to 3500 ps.

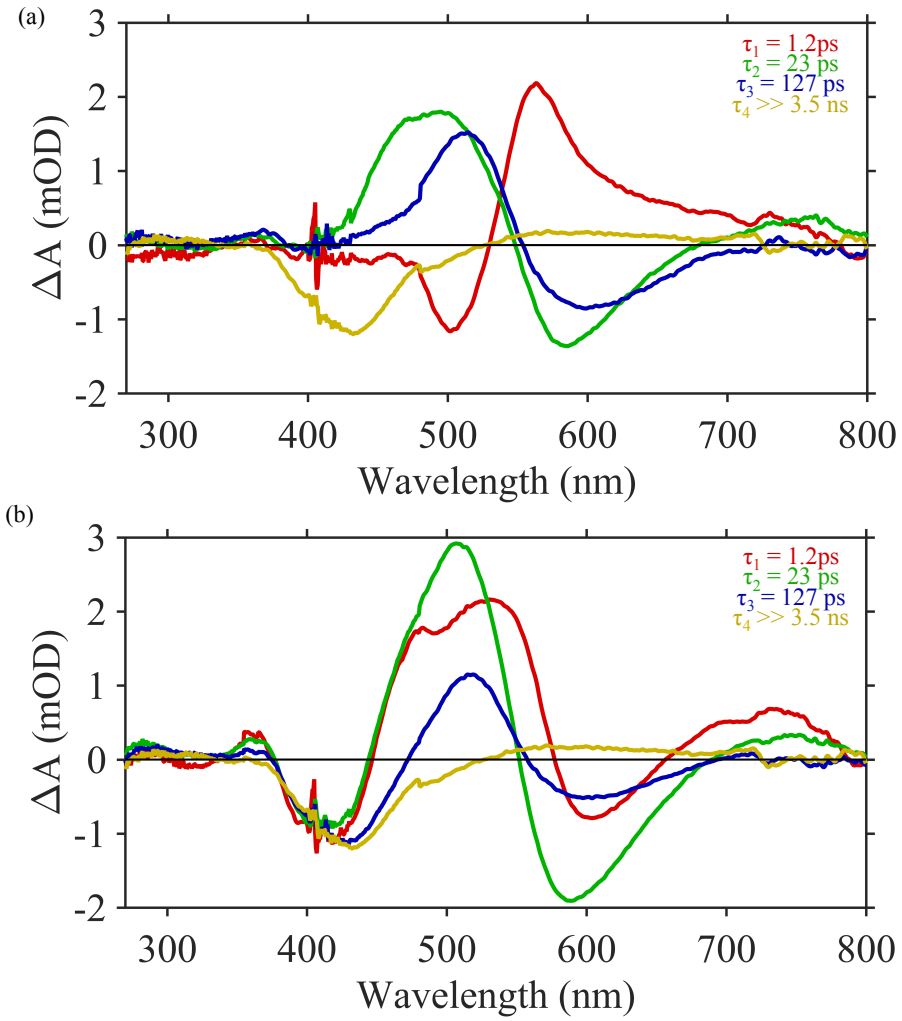

Figure 5.7 (a) Decay associated difference spectra (DADS) of indazole-MCH in PBS, (b) Species associated difference spectra (SADS) of indazole-MCH assuming a sequential model.

Phenylhydroxy-MCH in DMSO. The 404 nm excitation TA spectra of the phenylhydroxy-MCH were measured in DMSO using a UV continuum (260 – 600 nm) and shown in Figure 5.8. Data at early times are characterized by a GSB at ~ 425 nm, three ESA peaks around 300, 400 and 500 nm, and SE from ~ 540 nm to the red. At longer times, the ESA at ~ 500 nm and SE decay to baseline by ~ 300 ps, leaving behind a residual GSB and positive

photoproduct absorption from ~ 280 – 320 nm. This steady state photoproduct TA spectrum persists for > 3.5 ns. While ESA and SE at early times are qualitatively similar to the TA data obtained in aqueous buffer, the steady state photoproduct signal measured in DMSO is significantly different. The photoproduct signal spectrum has a positive signal in the UV (~ 260 – 320 nm), and little to no absorption in the visible (> 540 nm).

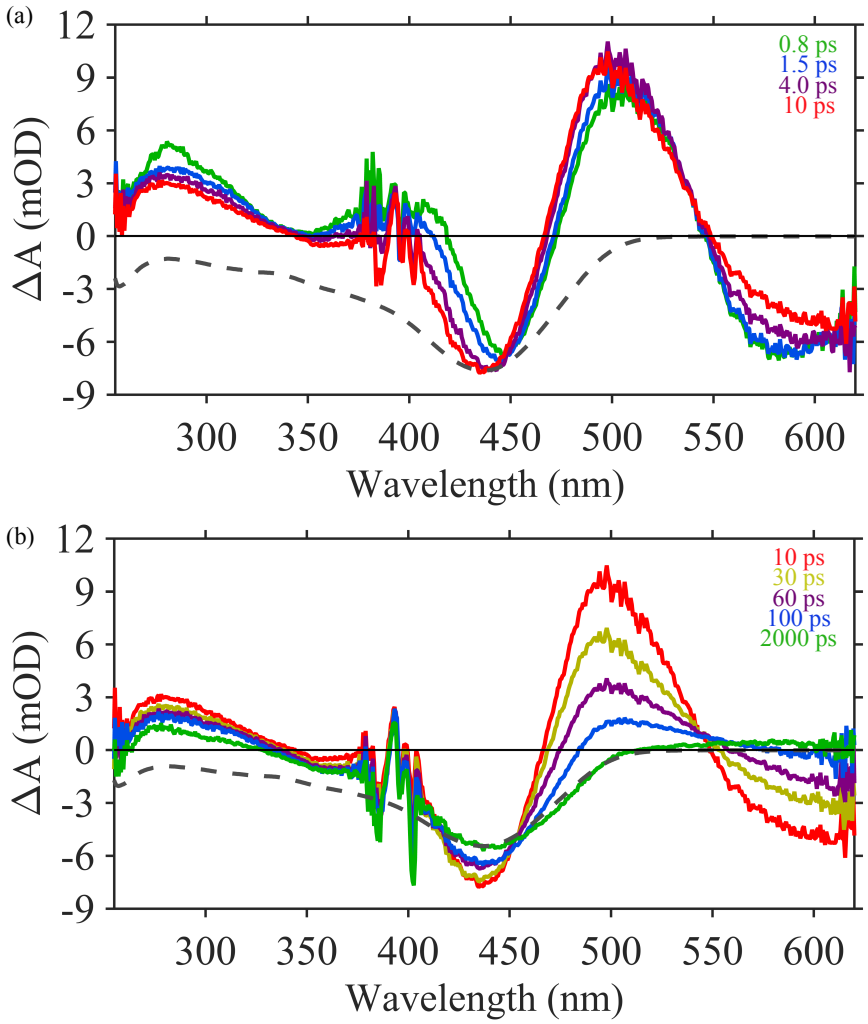

Figure 5.8. TA spectra of phenylhydroxy-MCH in DMSO at early times (a) 0.8 ps (green), 1.5 ps (blue), 4.0 ps (purple), 10 ps (red). Longer times (b) 10 ps (red), 30 ps (yellow), 60 ps (purple), 100 ps (blue) and 2000 ps (green). Scaled UV-vis of phenylhydroxy-MCH (grey dash).

The phenylhydroxy-MCH TA data in DMSO are best globally fit to a sum of four exponential decay model, associated amplitudes, and an additional amplitude to account for the long-lived photoproduct signal summarized in Table 5.1. The lifetimes obtained from the global fit are: τ_1 = 1.2 ps, τ_2 = 5.5 ps, τ_3 = 48.9 ps, τ_4 = 1.8 ns, and τ_5 >> 3.5 ns. The 1.8 ns component is poorly defined owing to lack of a large amount of relative time delay. TA experiments with a much longer delay stage would be necessary to distinguish between systematic drifts in the data and a rate on this order of magnitude. In addition, this component is low in amplitude and closely resembles the profile of the fifth component, which suggests there may be a small systematic drift in the data causing the signal to drop over the length of the delay stage. Kinetic lineouts at 290, 435, 500 and 600 nm are given in Figure 5.9 to show the quality of the fit. The DADS from the fit are shown in Figure 5.10, as well as the SADS that one obtains after assuming a sequential kinetic model.

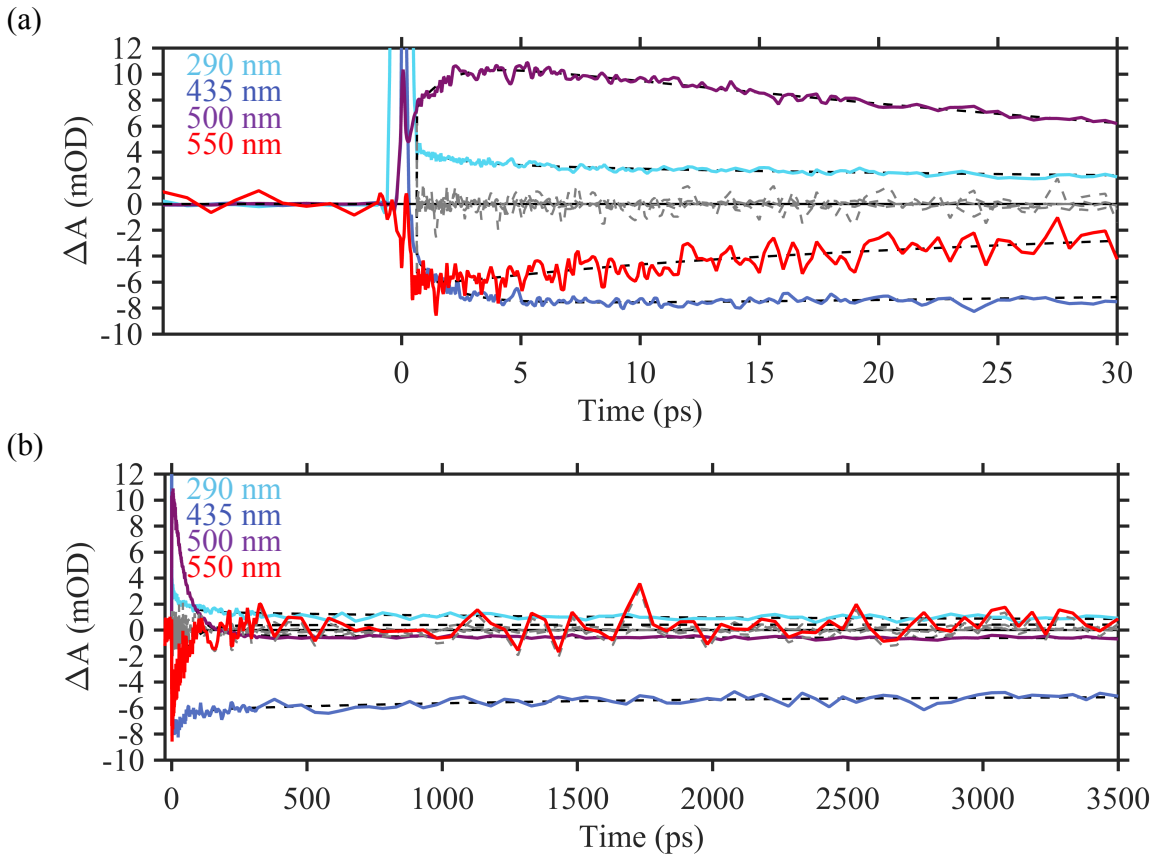

Figure 5.9. TA lineouts of the phenylhydroxy-MCH dissolved in DMSO at selected wavelengths at (a) early times and (b) longer times. 290 nm (light blue) tracks early ESA and later photoproduct absorption in light blue, 435 nm (dark blue) tracks early ESA and GSB, 500 nm (purple) tracks ESA, and 600 nm (red) tracks SE.

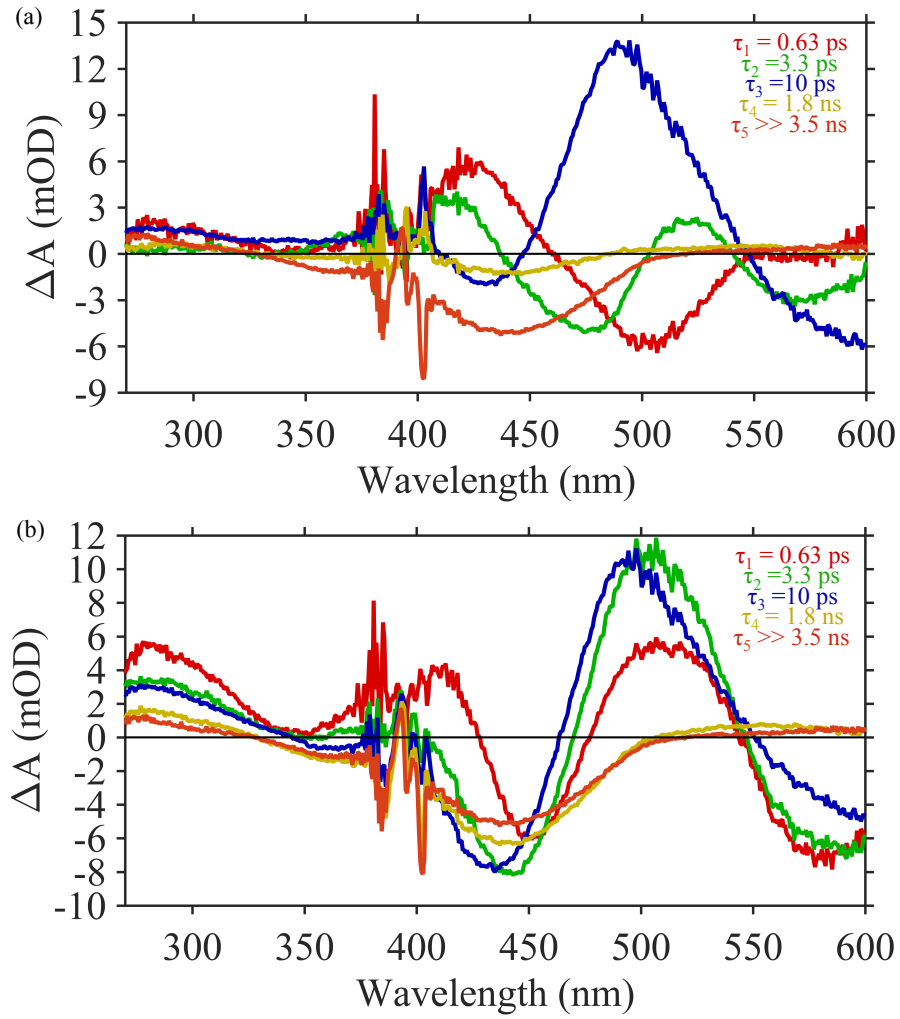

Figure 5.10 (a) Decay associated difference spectra (DADS) of phenylhydroxy-MCH in DMSO, (b) Species associated difference spectra (SADS) of phenylhydroxy-MCH assuming a sequential model.

Indazole-MCH. The TA data of the indazole-MCH in DMSO has a GSB centered at 420 nm, SE ranging from 550 – 600 nm, and ESA at 350 – 360 nm and 450 – 550 nm. At early times there are large coherent signals in the UV that persist for ~ 500 fs making analysis of the first 500 fs of the dataset difficult. The GSB differs greatly from the UV-vis spectrum of the sample, indicating overlapping ESA in this region. The GSB reaches a constant value by 1 ns and

remains constant for the subsequent 3.5 ns, forming a long-lived photoproduct as shown in Figure 5.11. The long-time photoproduct spectrum is characterized by a residual GSB, a positive absorption from ~ 275 – 325 nm and a weak positive absorption from ~ 550 – 600 nm. The residual GSB is centered at 450 nm while the peak center of the UV-vis spectrum is centered at 435 nm.

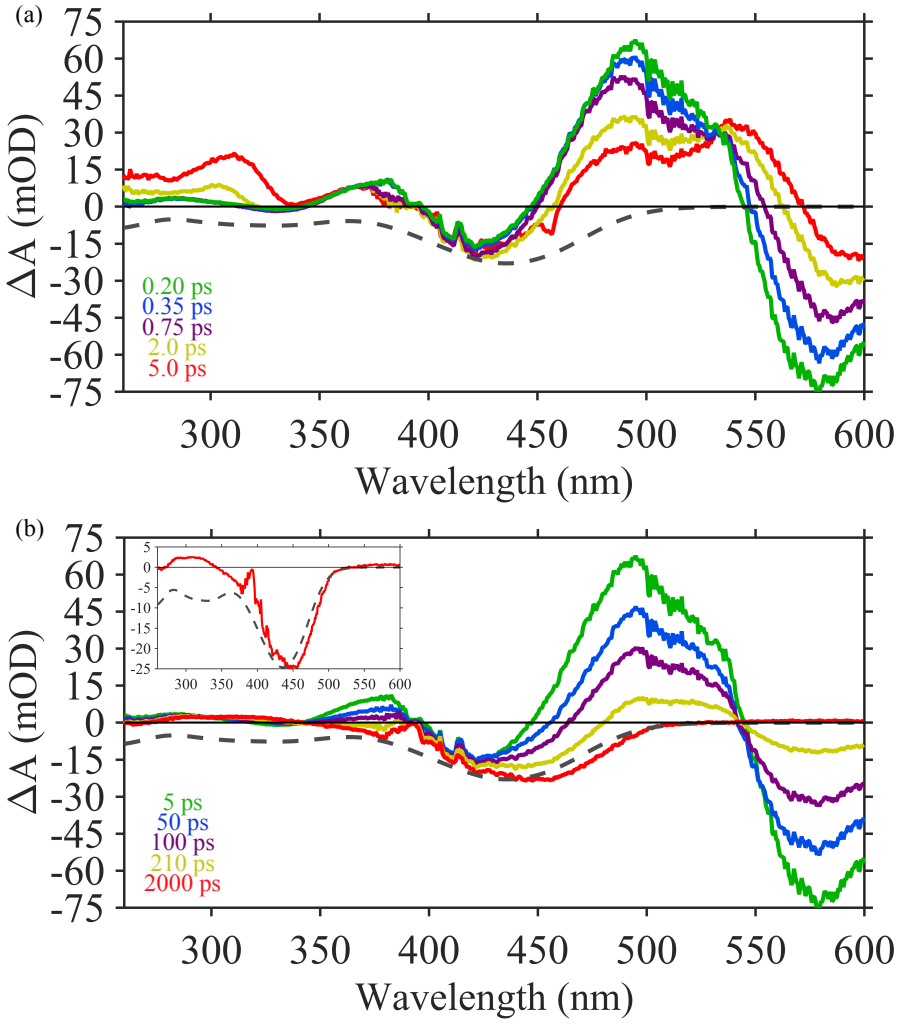

Figure 5.11. (a) TA spectra of indazole-MCH in DMSO at 0.2 ps (red), 0.35 ps (yellow), 0.75 ps (purple), 2.0 ps (blue), 5.0 ps (green). (b) 5.0 ps (green), 50 ps (blue), 100 ps (purple), 210 ps (yellow) and 2000 ps (red), and scaled UV-vis (grey dash). INSET: 3000 ps spectrum.

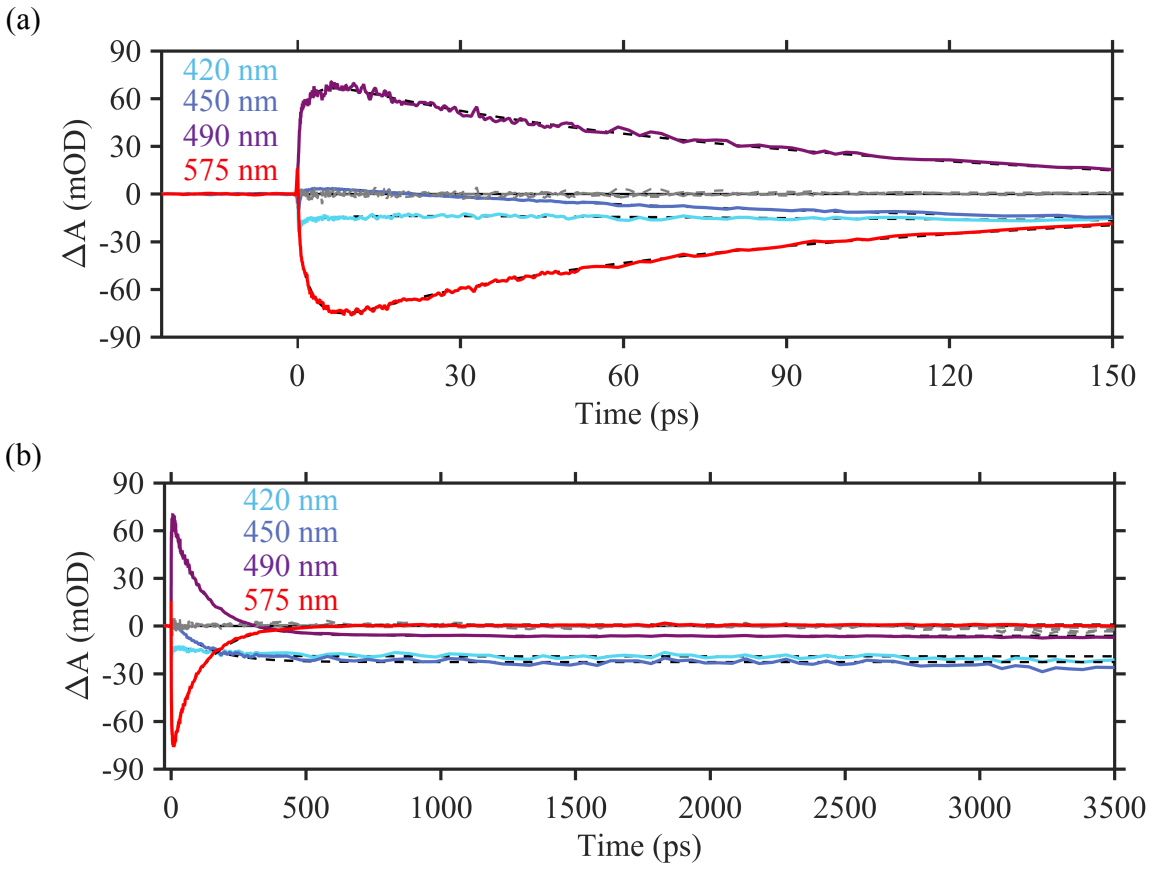

Figure 5.12. TA lineouts, fits and residuals at select wavelengths of indazole-MCH in DMSO after excitation with 404 nm. 420 and 450 nm (light blue and dark blue, respectively) track the GSB, 490 nm (purple) tracks ESA, 575 nm (red) tracks SE. (a) Early time delays and (b) longer time delays.

The indazole-MCH TA data in DMSO are best globally fit to a sum of four exponential decay components, associated amplitudes, and an additional time independent amplitude term. Coherent signals in the data around time zero make the data difficult to fit before 500 fs. The rates obtained from the fit are: τ_1 = 0.31 ps, τ_2 = 3.1 ps, τ_3 = 28.3 ps, τ_4 = 128 ps, and τ_5 >> 3.5 ns, summarized in Table 5.1. Lineouts of the data at 420, 450, 490, and 575 nm are

shown in Figure 5.12. The DADS obtained from the global fit are transformed into SADS assuming a sequential kinetic model and shown in Figure 5.13.

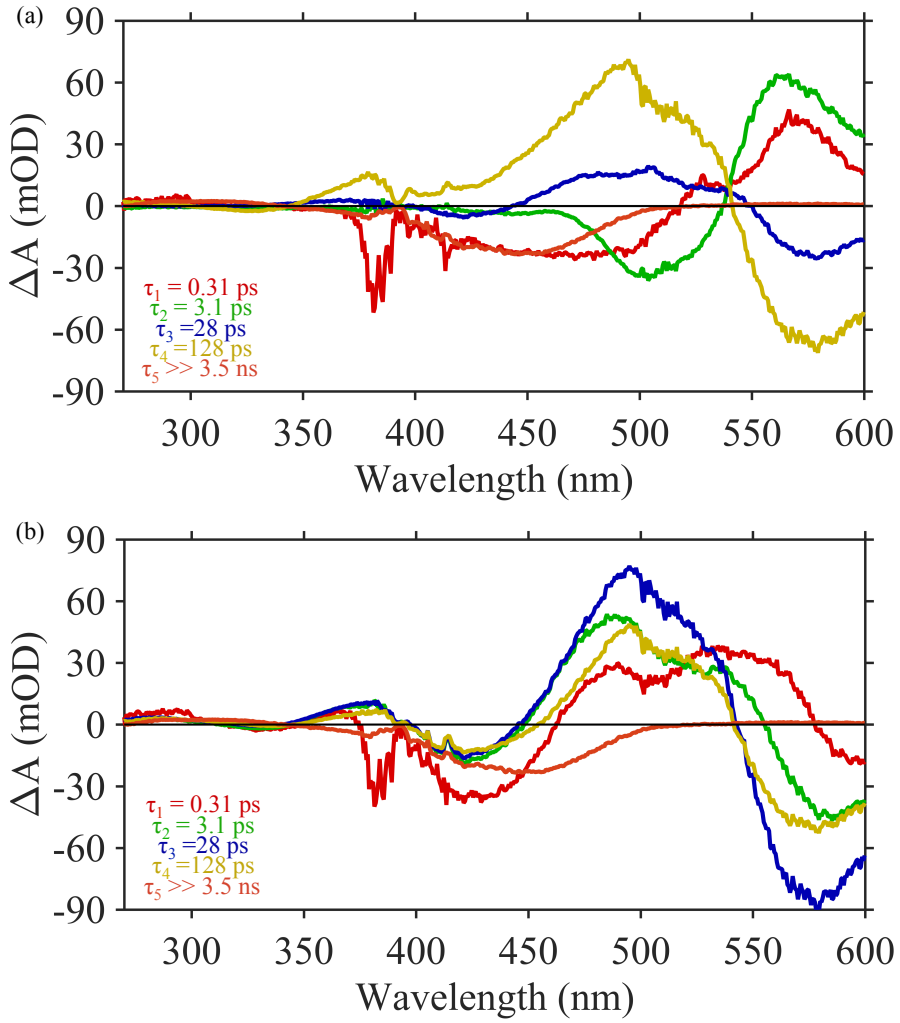

Figure 5.13 (a) Decay associated difference spectra (DADS) of indazole-MCH in DMSO, (b) Species associated difference spectra (SADS) of indazole−MCH assuming a sequential model.

Phenylhydroxy-MC$^-$. The TA spectrum of phenylhydroxy-MC$^-$ was measured after excitation by 530 nm with either a visible continuum from 350 – 800 nm or a UV continuum from 260 - 600 nm as shown in Figure 5.14. The TA spectra show GSB at 350 and 530 nm, ESA at

470 nm, SE from 580 – 800 nm, a very weak (-5 x 10^{-5} OD) residual GSB, and a very weak (0.1 mOD) photoproduct peak at 380 nm. The GSB increases in magnitude at short times (< 500 fs), most likely due to overlapping ESA, reaching a maximum magnitude of -9.5 mOD at 1 ps. The GSB decays to a steady state value of -5.0 x 10^{-5} OD by 60 ps, and remains constant for ~ 3.5 ns. At early times (< 1 ps), SE narrows, red-shifts, and decays to baseline. ESA at 470 nm blue-shifts and broadens at early times (< 1 ps) and then decays along with the SE signal. At long times (> 500 ps), a 1 x 10^{-4} OD signal can be seen at 375 – 425 nm as shown in Figure 5.14.

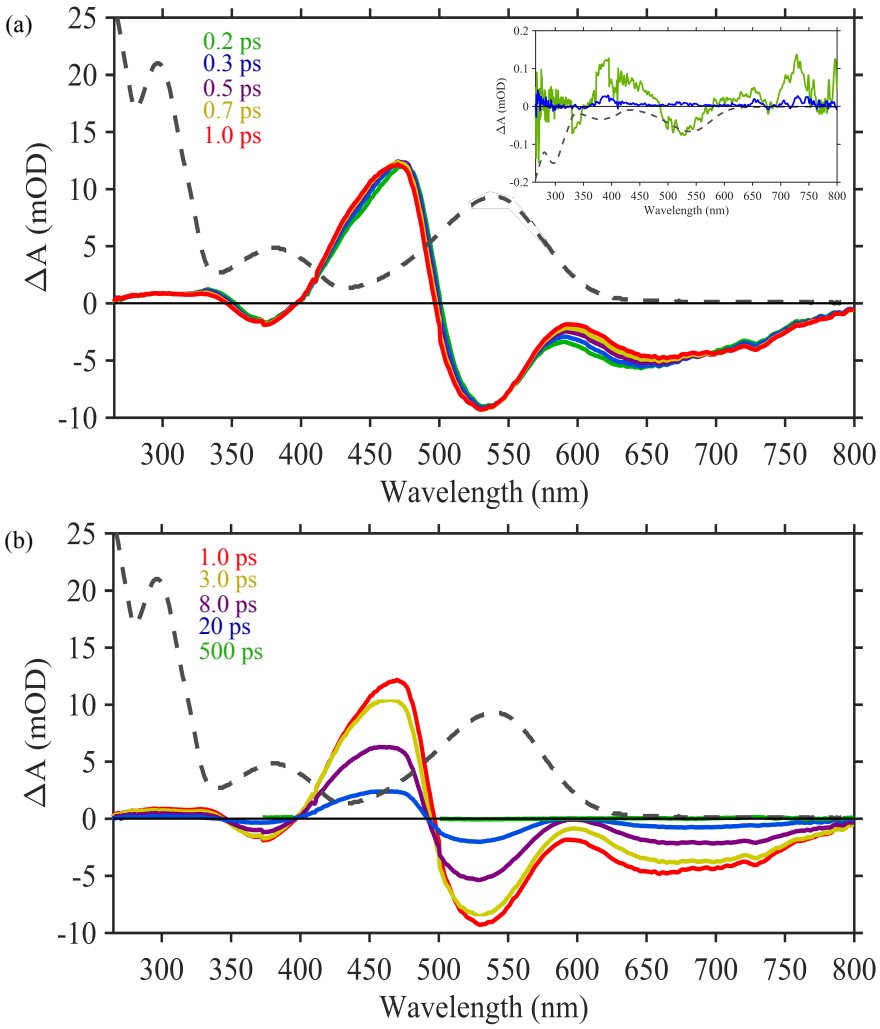

Figure 5.14. (a) TA spectra of phenylhydroxy-MC$^-$ in buffer excited with 530 nm at 200 fs (green), 300 fs (blue), 500 fs (purple), 700 fs (yellow), 1.0 ps (red), and scaled UV-vis (grey dash). (b) TA spectra at 1.0 ps (red), 3.0 ps (yellow), 8.0 ps (purple), 20 ps (blue), 500 ps (green), and scaled UV-vis (grey dash). INSET: difference spectra averaged from 250 to 3400 ps (green), baseline signal (blue), scaled UV-vis (grey dash).

Density functional theory. DFT calculations incorporating a polarizable continuum model (PCM) with the dielectric constant of water were used to determine the free energies of all of the *trans* MC conformers and the SP conformers, summarized in Table 2. The phenylhydroxy-MCH

trans conformers are 8 – 9 kcal/mol lower in free energy than the phenylhydroxy-SP, and the indazole-MCH trans conformers are 5 – 6 kcal/mol lower in free energy than the indazole-SP. This is in agreement with existing results[13–16] showing the SP form reverting back to the *trans*-MCH form when left in the dark. Regardless of solvent model, the free energies obtained from DFT calculations indicate there is a mixture of trans conformations at room temperature. The two dominant conformers for the phenylhydroxy-MCH are TTT and CTT with 44.7% and 32.2% relative populations, respectively. The two dominant conformers for the indazole-MCH are TTT and TTC with 71.5 % and 18.7%, respectively as shown in Figure 5.15.

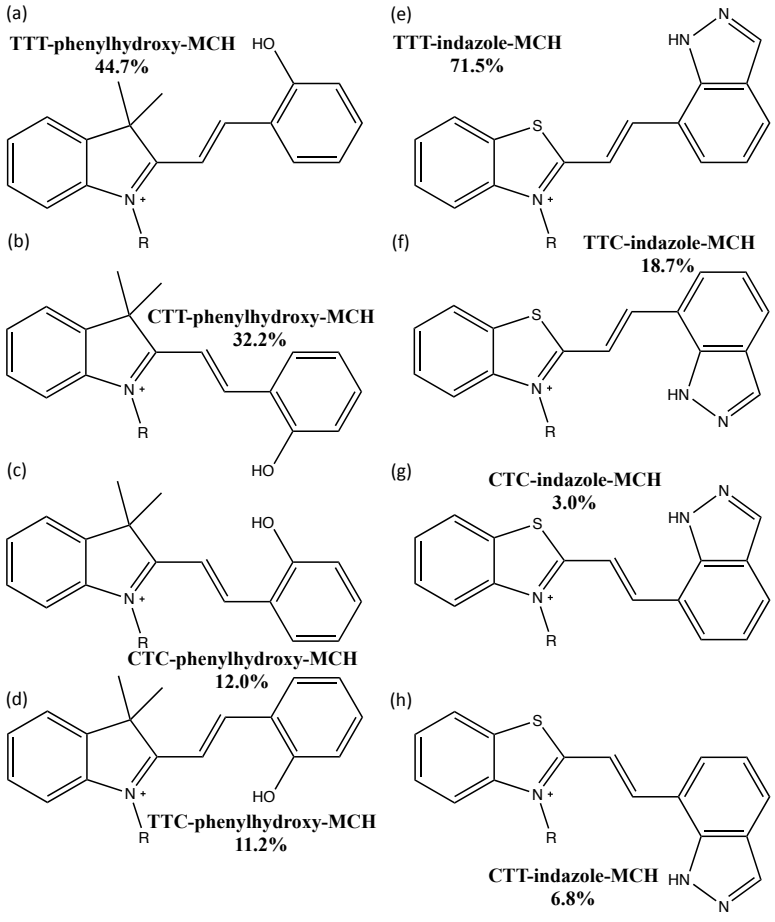

Figure 5.15. Structures from DFT optimizations, R = CH_3.

Table 5.2. Free energies obtained from DFT frequency calculations, using B3LYP/6-311G in a polarizable continuum (n = 80.4, water)**

Conformer	ΔH (kcal/mol)	ΔS (kcal/(mol*K))	ΔG (kcal/mol)	relative *trans* populations
TTT-Phenylhydroxy-MCH	229.972	0.139236	189.294	44.7%
CTT-Phenylhydroxy-MCH	229.767	0.137868	189.489	32.2%
TTC-Phenylhydroxy-MCH	230.062	0.136737	190.114	11.2%
CTC-Phenylhydroxy-MCH	229.895	0.136300	190.075	12.0%
Phenylhydroxy-SP	220.847	0.131287	182.492	
TTT-Indazole-MCH	184.813	0.135736	145.158	71.5%
CTT-Indazole-MCH	184.903	0.131274	146.551	6.8%
TTC-Indazole-MCH	184.869	0.133203	145.954	18.7%
CTC-Indazole-MCH	185.014	0.129980	147.040	3.0%
Indazole-SP	176.159	0.124593	139.759	

Time dependent density functional theory (TDDFT) calculations using a LR-PCM model were carried out as well. The lowest energy vertical transition energies of the most relevant species are summarized in Table 5.3. In the case of the phenylhydroxy-MC, the only species, which displays red-shifted absorptions with respect to the trans-conformers are the deprotonated *cis* conformers.

Table 5.3. Vertical excitation maxima and intensities for relevant structures calculated with TDDFT, PCM (n = 80.4), B3LYP/6-311G.**

Conformer	Vertical transition (nm)	Oscillator Strength	Observed transition (nm)
TTT-Phenylhydroxy-MCH	431.0	0.6366	425
CTT-Phenylhydroxy-MCH	426.5	0.6012	
TTC-Phenylhydroxy-MCH	422.3	0.5750	
CTC-Phenylhydroxy-MCH	414.8	0.5361	
CCC-Phenylhydroxy-MCH	404.3, 357.7	0.2068, 0.2886	
TCT-Phenylhydroxy-MCH	480.1, 425.1	0.3285, 0.2730	
CCT-Phenylhydroxy-MCH	424.0, 364.3	0.2660, 0.1764	
TCC-Phenylhydroxy-MCH	397.6, 328.0	0.0431, 0.1068	
CCC-Phenylhydroxy-MC$^-$	506.0	0.1338	
TCT-Phenylhydroxy-MC$^-$	499.4	0.6728	
CCT-Phenylhydroxy-MC$^-$	515.7	0.4458	
TCC-Phenylhydroxy-MC$^-$	327.7	0.0154	
TTT-Indazole-MCH	456.6	0.8415	425
CTT-Indazole-MCH	443.4	0.7802	
TTC-Indazole-MCH	438.3	0.8315	
CTC-Indazole-MCH	428.3	0.7960	
Phenylhydroxy-SP	328.2	0.0145	294
Indazole-SP	408.2, 238.9	0.0007, 0.1214	331

Discussion

Phenylhydroxy-MCH. The results presented demonstrate a solvent dependence in the formation of intermediates connecting phenylhydroxy-MCH to phenylhydroxy-SP. Steady state photolysis in either citrate buffer or DMSO leads to prompt (< 1 sec) formation of SP. However, picosecond to nanosecond TA data in citrate buffer produces a long-lived difference spectrum inconsistent with the formation of SP on a nanosecond timescale. Phenylhydroxy-SP has no visible absorption bands, and the 3.5 ns TA spectra collected in citrate buffer has a positive peak from 475 – 600 nm. The TA data indicate the formation of an intermediate that cannot be phenylhydroxy-SP as shown in Figure 5.16.

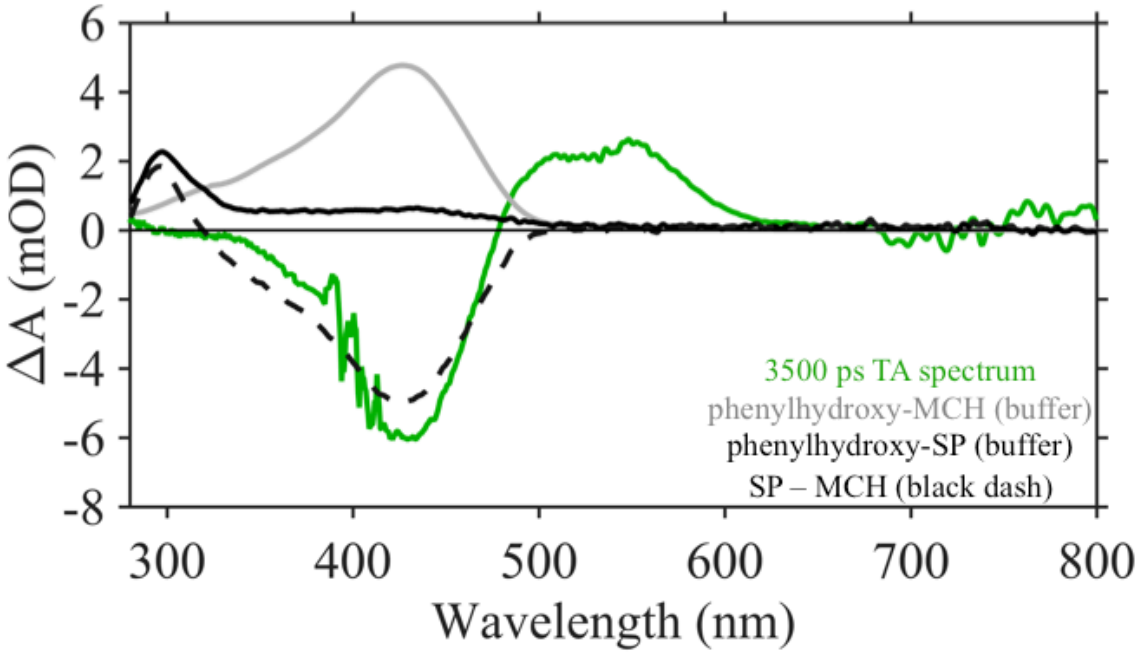

Figure 5.16. Comparison of 3500 ns TA spectrum (green) of *trans*-phenylhydroxy-MCH in citrate buffer excited with 404 nm to the steady state difference spectra (black dash) between phenylhydroxy-SP (black) and *trans*-phenylhydroxy-MCH (grey).

Time dependent density functional theory (TDDFT) was used to identify possible intermediates. All reasonable structures of the phenylhydroxy-MCH were optimized both as isolated molecules and using a PCM with a dielectric of water (n = 80.4) or DMSO (n = 46.7) to mimic the solvent environments. Vertical excitation energies were calculated and are summarized in Table 5.3. The calculated wavelengths of the *trans*-phenylhydroxy-MCH conformations and phenylhydroxy-SP are in reasonable agreement with the measured UV-visible spectra. Furthermore, if Gaussian line shapes with 1600 cm^{-1} widths are assumed for each of the transitions, the simulated spectra agree with the measured UV-visible spectrum of *trans*-phenylhydroxy-MCH as shown in Figure 5.17a. The only structures with significant vertical excitation intensity in the range of 475 – 600 nm are deprotonated *cis* (CCC, TCT, CCT) conformations. Thus, the intermediate is likely one of the cis conformations. The fourth *cis* conformation, TCC, was not stable, converging instead on spiropyran.

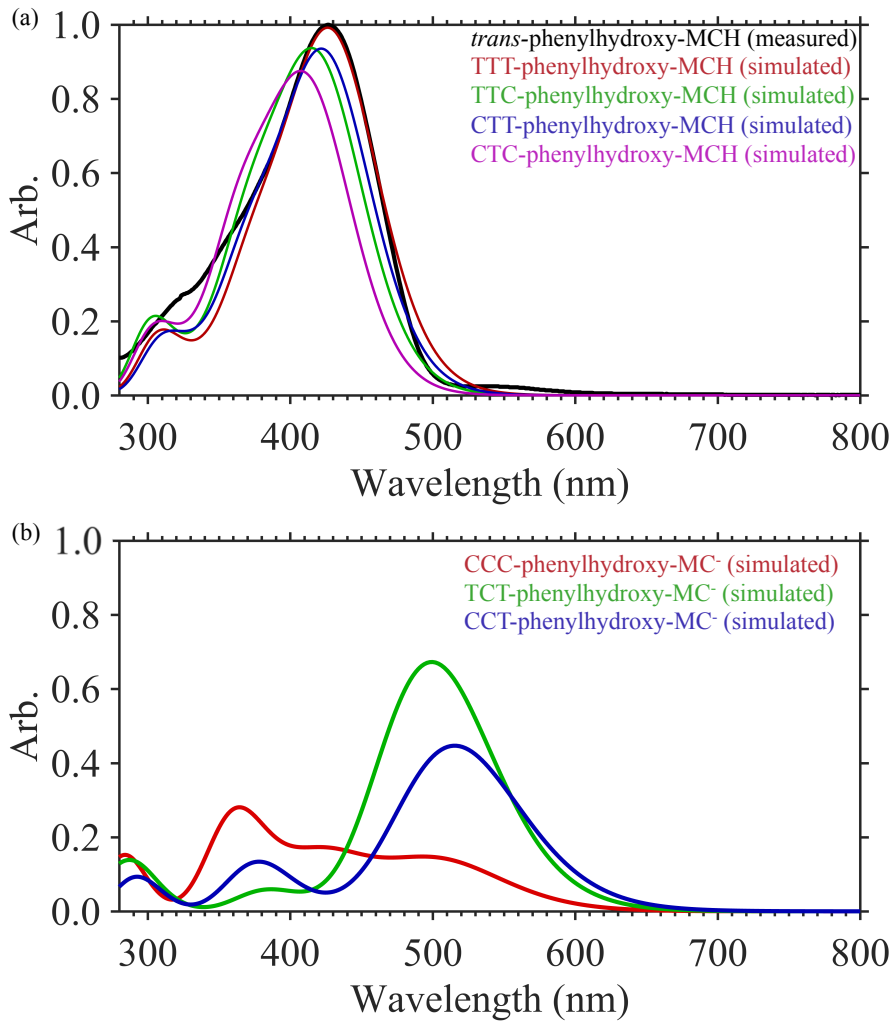

Figure 5.17. (a) Comparison of UV-vis of *trans*-phenylhydroxy-MCH in buffer to simulated spectra of trans conformation using 0.2 eV Gaussian functions centered at vertical transition energies calculated by TDDFT. TTT is red, TTC is green, CTT is blue and CTC is magenta. (b) Simulated *cis*-phenylhydroxy-MC$^-$ spectra, CCC conformer is red, TCT conformer is green, and CCT conformer is blue.

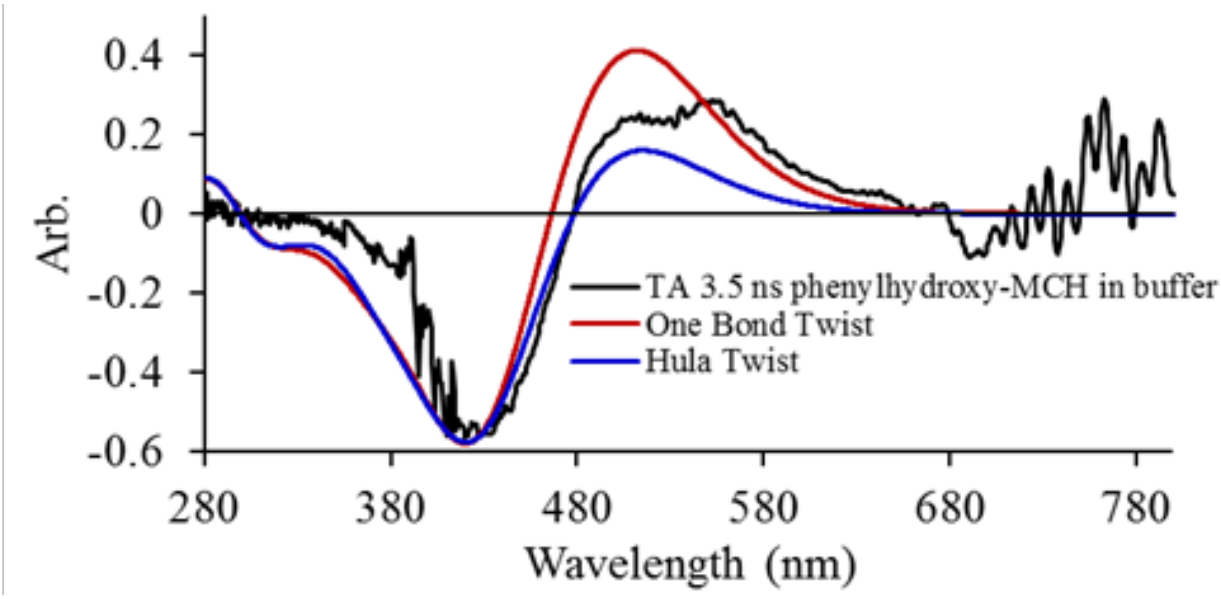

Figure 5.18. Simulated difference spectrum between *cis*-phenylhydroxy-MC⁻ and *trans*-phenylhydroxy-MCH (red and blue) in comparison to 3.5 ns TA spectrum of phenylhydroxy-MCH in citrate buffer (black).

One can simulate the 3.5 ns TA spectrum as the difference each *cis*-phenylhydroxy-MC⁻ conformation and each of the *trans*-phenylhydroxy-MCH conformation. There are eight reasonable pathways, four corresponding to a one bond flip isomerization: TTT→TCT, TTC→TCC, CTT→CCT, and CTC→CCC, and four corresponding to a hula twist isomerization: TTT→ TCC, TTC→ TCT, CTT→ CCC, and CTC→CCT. These calculations suggest more than one initial conformation is present at equilibrium and this is a common property of merocyanines. If the initial population is a mixture of the *trans*-phenylhydroxy-MCH conformations with the calculated weights in Table 5.2, a reasonable estimate of the photoproduct difference spectrum is obtained for both the hula twist and one-bond flip mechanisms as shown in Figure 5.18. All of the existing literature on merocyanines in solution

indicates that there are at least two conformations present in solution[27–35,35,36]. To further address the possibility of multiple trans conformers in solution, one would need to do more experiments. For example, two dimensional electronic spectroscopy by Nuernberger et al.[29] and TA spectroscopy Wohl et al.[27] on nitro- and dinitro-substituted merocyanines scanned the pump wavelength across the absorption band of the molecules and found wavelength dependent photoproduct formation concluding inhomogeneity of the ground state molecule. Unfortunately, the absorption peak of *trans*-phenylhydroxy-MCH is situated in a region of the visible spectrum (300 – 480 nm), which is quite difficult to scan with our instrument. Future studies will rely on collaboration with other labs to scan these pump wavelengths.

Different TA results are obtained for *trans*-phenylhydroxy-MCH when it is dissolved in anhydrous DMSO rather than aqueous solution. The 3.5 ns TA spectrum more closely resembles the spectrum one would expect if phenylhydroxy-SP were formed as shown in Figure 5.19. The photoproduct absorption peak in the UV from 270 – 330 nm is in reasonable agreement with the steady-state difference spectrum between SP and MC. The GSB matches the peak center and red side of the state UV-vis spectrum of the *trans*-phenylhydroxy-MCH, but the magnitude of the GSB from ~ 330 – 420 nm is consistently higher than the steady state difference spectrum. This could be the result of inhomogeneity in the ground state as stated previously. Again, future work will attempt to investigate this using a range of pump wavelengths to scan over the ground state absorption.

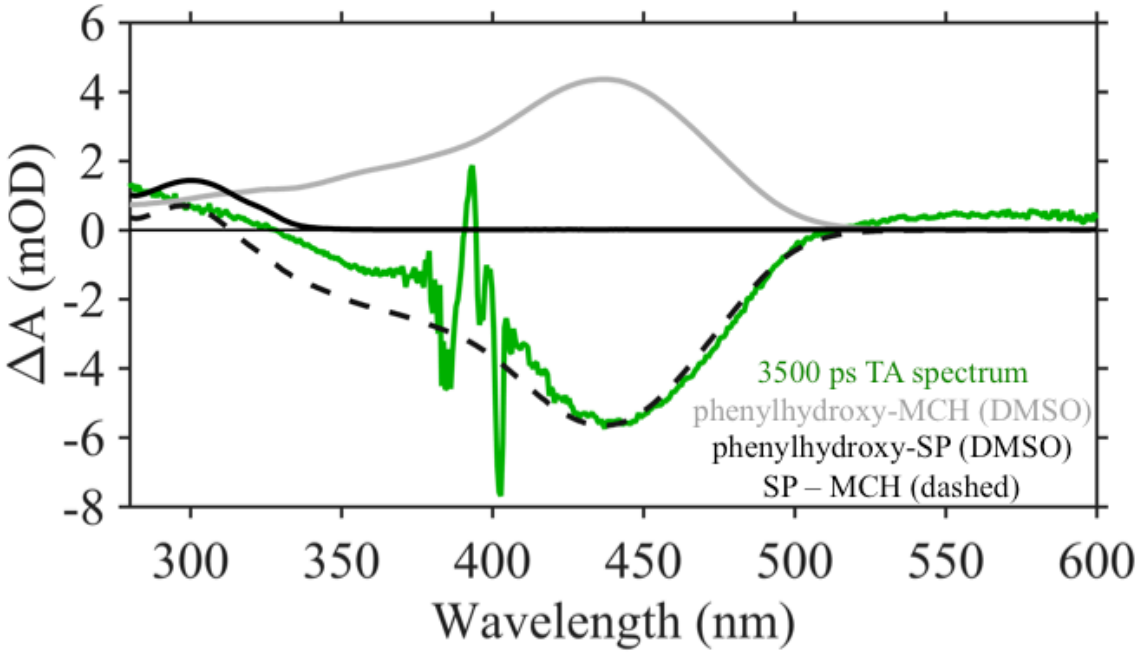

Figure 5.19. Comparison of 3500 ns TA spectrum (green) of *trans*-phenylhydroxy-MCH in DMSO excited with 404 nm to the steady state difference spectra (black dash) between phenylhydroxy-SP (black) and *trans*-phenylhydroxy-MCH (grey).

The differences between the results in aqueous buffer and DMSO lead to the formation of a hypothesis that hydrogen bonding could extend the lifetime of a cis intermediate before ring closure to form spiropyran. This would account for the difference between the long-lived species in aqueous buffer photoproduct and DMSO. Simulations were performed to test this hypothesis. The growing string method[25] was used to estimate the transition states and barriers between CCC-phenylhydroxy-MC$^-$ and phenylhydroxy-SP in vacuum and incorporating a single water molecule hydrogen bonded to the phenylhydroxy side of the molecule as shown in Figure 5.20. Indeed, adding one water molecule hydrogen bonded to the CCC conformer increases the barrier for ring closure from ~ 2.3 kcal/mol to ~ 4.5 kcal/mol. This would translate to a ~ 41 fold

increase in rate in a hydrogen bonded solvent relative to a solvent without hydrogen bonding, assuming the same Arrhenius pre-factor for both instances. Of course, this is a crude estimate, but an accurate simulation of the transition state interacting with many explicit water molecules is beyond the scope of the lab's repertoire.

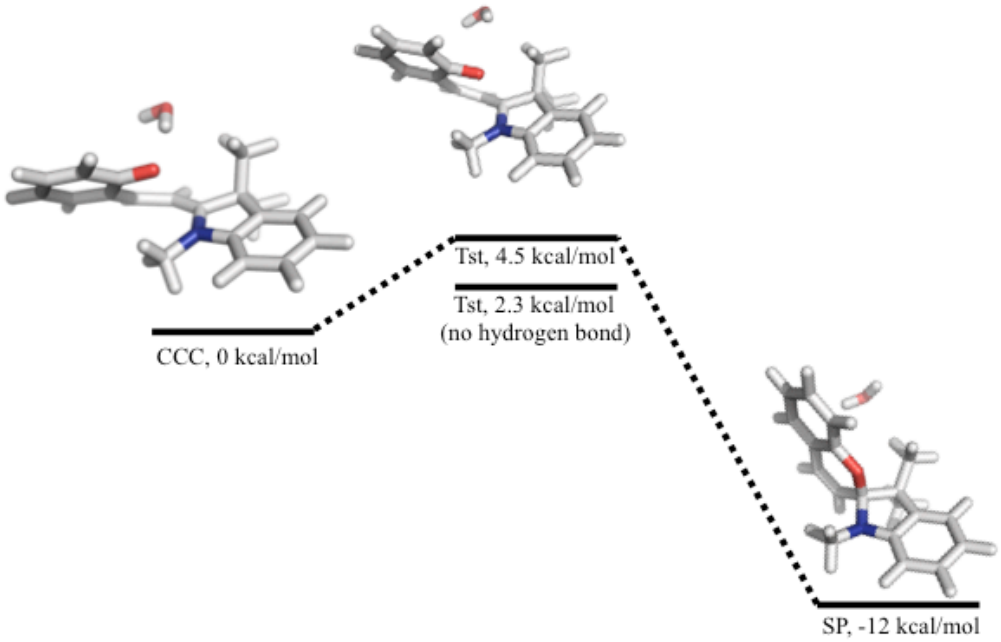

Figure 5.20. Results of transition state search between CCC-phenylhydroxy-MC$^-$ and phenylhydroxy-SP using growing string method. The activation energy is 4.5 kcal/mol when a hydrogen bond is present, relative to 2.3 kcal/mole when there is no hydrogen bond present.

Indazole-MCH. SE from 550 – 700 nm persists across all timescales in the TA data in PBS or DMSO. Therefore, all excited states involved are optically coupled to the ground state. The long time difference spectrum shows a permanent GSB for >> 3.5 ns, with weak product absorption at wavelengths ≤ 350 nm. The residual GSB imperfectly matches the steady state UV-vis spectrum shown in Figure 5.21. It is likely the photoproducts are ring closed indazole-SP, and

discrepancies between the steady difference spectrum and long time TA GSB results from ground state inhomogeneity of *trans*-indazole-MCH. The indazole-MCH photoproducts are insensitive to solvent in these experiments. This is likely due to the absence of hydrogen bond interactions in this system.

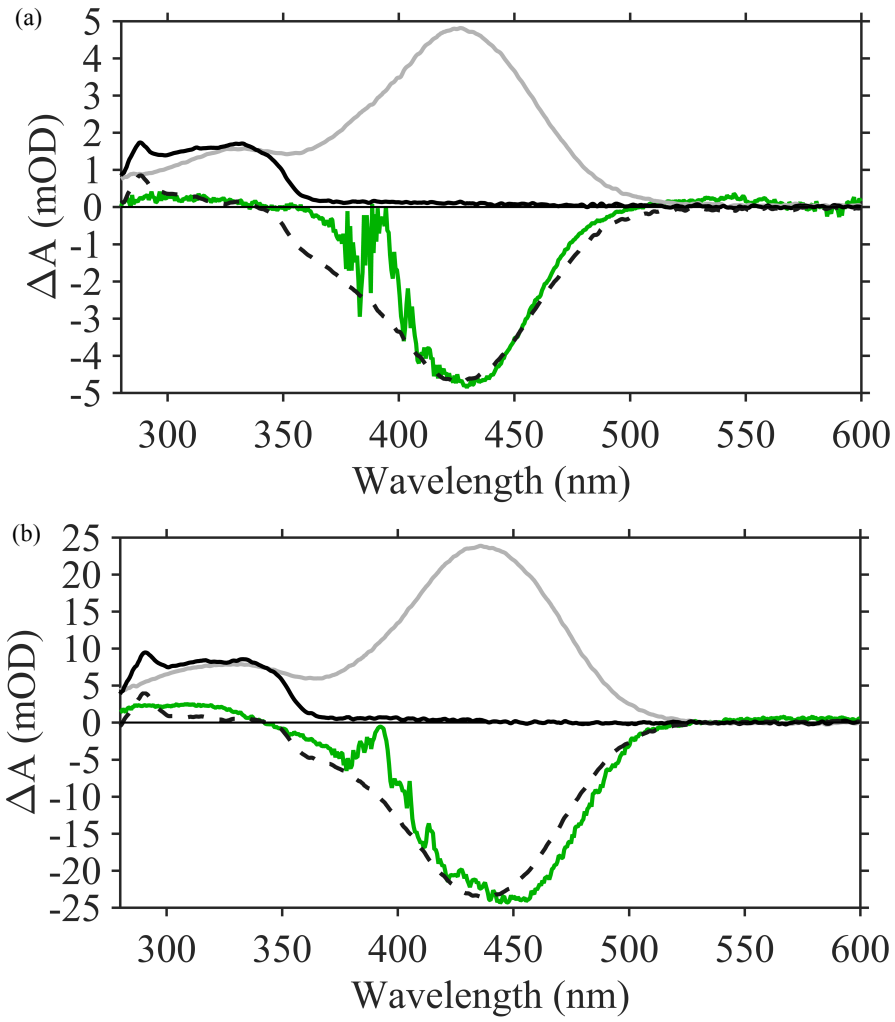

Figure 5.21. Indazole-MCH in (a) PBS or (b) DMSO. 3500 ns TA spectrum (green), *trans*-indazole-MCH UV-vis (grey), indazole-SP UV-vis (black), SP-MCH (black dash).

Phenylhydroxy-MC$^-$. All of the excited states involved are optically coupled to the ground state because SE signals decay to zero concurrently with the recovery of the GSB. The long time difference spectrum shows little to no photoproduct formation. If there is photoproduct formation, then the quantum yield is no more than 0.5 %. There is no evidence for the formation of SP in the TA data, because there is no peak at 293 nm. In addition, there is no steady state photolysis evidence of SP formation after irradiation of *trans*-phenylhydroxy-MC$^-$.

This result is contrary to the reported claim[13] that irradiation with ≥ 530 nm of the *trans*-phenylhydroxy-MC$^-$ does produce phenylhydroxy-SP. On the other hand, this result is in line with many existing ultrafast investigations showing that deprotonated nitro-substituted merocyanines are less and less likely to form spiropyran with decreasing number of nitro-substitutions. Work by Brixner et al.[29,32,37], Wohl et al.[27], and Kohl-Landgraf et al.[33] show that dinitro-substituted merocyanine ring closes with about 40% quantum yield and singly nitro-substituted merocyanine does not undergo ring closure at all.

Conclusions

Interesting solvent effects on the photochemical formation of phenylhydroxy-SP have been found. When the *trans*-phenylhydroxy-MCH is dissolved in a protic solvent such as water, photoexcitation of the molecule produces a species with red-shifted absorption with respect to the *trans*-phenylhydroxy-MCH on a ~ 10 ps timescale which does not change for at least 3.5 ns. However, this intermediate does eventually form phenylhydroxy-SP, because phenylhydroxy-SP is readily produced in steady state photolysis experiments. The intermediate is assigned to a *cis*-phenylhydroxy-MC$^-$ on the basis of TDDFT calculations. When the *trans*-phenylhydroxy-MCH is dissolved in a polar aprotic solvent, such as DMSO,

photoexcitation produces a species with no visible absorption bands on a 50 ps timescale. It is hypothesized that hydrogen bonding extends the lifetime of the deprotonated cis species in water, preventing the formation of phenylhydroxy-SP on a timescale observable in our TA experiments. In DSMO, there is no hydrogen bonding and phenylhydroxy-SP is able to form much faster. Growing string calculations find a two-fold increase in the barrier for forming phenylhydroxy-SP from CCC-phenylhydroxy-MC- when a hydrogen bonded water molecule is present give support to this hypothesis. There are other possibilities, however. For example, the protonated *cis*-phenylhydroxy-MCH conformers do not have visible absorption either. The photoproducts in DMSO could be *cis*-phenylhydroxy-MCH, rather than phenylhydroxy-SP.

The deprotonated *trans*-phenylhydroxy-MC$^-$ does not appear to produce phenylhydroxy-SP in transient absorption or steady state photolysis whatsoever. This is a surprise because Liao et al. report that visible irradiation of this species will produce phenylhydroxy-SP[15]. In addition, this is in contrast to recent results on a very similar water soluble MC/SP molecule that does undergo ring-closure when excited with 520 nm[33].

Unlike the phenylhydroxy-MCH, the indazole-MCH photoproducts observed in TA show little dependence on solvent. In both water and DMSO, photoproducts with essentially no visible absorption are observed. It is likely that indazole-SP is formed within the time window of our TA experiments in both solvents. This insensitivity to protic versus aprotic solvent is likely due to the indazole group not being a hydrogen bond donor or acceptor.

Notes to Chapter 5

(1) Bouas-Laurent, H.; Dürr, H. *Photochromism : Molecules and systems*; 2003.

(2) R. Heiligman-Rim, Y. Hirshberg, E. F. *J. Chem. Soc.* **1961**, *297*, 156–163.

(3) Ernsting, N. P.; Arthen-Engeland, T. *J. Phys. Chem.* **1991**, *95* (14), 5502–5509.

(4) Zhu, M. Q.; Zhu, L.; Han, J. J.; Wu, W.; Hurst, J. K.; Li, A. D. Q. *J. Am. Chem. Soc.* **2006**, *128* (13), 4303–4309.

(5) Mahvidi, S.; Takeuchi, S.; Kusumoto, S.; Sato, H.; Nakagawa, T.; Yokoyama, Y. *Org. Lett.* **2016**, *18* (19), 5042–5045.

(6) Rosario, R.; Gust, D.; Hayes, M.; Jahnke, F.; Springer, J.; Garcia, A. A. *Langmuir* **2002**, *18* (21), 8062–8069.

(7) Rosario, R.; Gust, D.; Garcia, A. A.; Hayes, M.; Taraci, J. L.; Clement, T.; Dailey, J. W.; Picraux, S. T. *J. Phys. Chem. B* **2004**, *108* (34), 12640–12642.

(8) London, G.; Chen, K. Y.; Carroll, G. T.; Feringa, B. L. *Chem. - A Eur. J.* **2013**, *19* (32), 10690–10697.

(9) Johns, V. K.; Patel, P. K.; Hassett, S.; Calvo-Marzal, P.; Qin, Y.; Chumbimuni-Torres, K. Y. *Anal. Chem.* **2014**, *86* (13), 6184–6187.

(10) Bao, H.; Li, F. F.; Lei, L. C.; Yang, B.; Li, Z. J. *Rsc Adv.* **2014**, *4* (52), 27277–27280.

(11) Andersson, J.; Li, S. M.; Lincoln, P.; Andreasson, J. In *Chemistry of Nucleic Acid Components*; 2008; Vol. 10, pp 305–306.

(12) Beyer, C.; Wagenknecht, H. A. *Synlett* **2010**, No. 9, 1371–1376.

(13) Shi, Z.; Peng, P.; Strohecker, D.; Liao, Y. *J. Am. Chem. Soc.* **2011**, *133* (37), 14699–14703.

(14) Johns, V. K.; Wang, Z.; Li, X.; Liao, Y. *J. Phys. Chem. A* **2013**, *117* (49), 13101–13104.

(15) Abeyrathna, N.; Liao, Y. *J. Am. Chem. Soc.* **2015**, *137* (35), 11282–11284.

(16) Johns, V. K.; Peng, P.; Dejesus, J.; Wang, Z.; Liao, Y. *Chem. - A Eur. J.* **2014**, *20* (3), 689–692.

(17) Klajn, R. *Chem. Soc. Rev.* **2014**, *43* (1), 148–184.

(18) Shao, Y.; Gan, Z.; Epifanovsky, E.; Gilbert, A. T. B.; Wormit, M.; Kussmann, J.; Lange, A. W.; Behn, A.; Deng, J.; Feng, X.; Ghosh, D.; Goldey, M.; Horn, P. R.; Jacobson, L. D.; Kaliman, I.; Khaliullin, R. Z.; Kuś, T.; Landau, A.; Liu, J.; Proynov, E. I.; Rhee, Y. M.; Richard, R. M.; Rohrdanz, M. A.; Steele, R. P.; Sundstrom, E. J.; Woodcock, H. L.; Zimmerman, P. M.; Zuev, D.; Albrecht, B.; Alguire, E.; Austin, B.; Beran, G. J. O.; Bernard, Y. A.; Berquist, E.; Brandhorst, K.; Bravaya, K. B.; Brown, S. T.; Casanova, D.; Chang, C.-M.; Chen, Y.; Chien, S. H.; Closser, K. D.; Crittenden, D. L.; Diedenhofen, M.; DiStasio, R. A.; Do, H.; Dutoi, A. D.; Edgar, R. G.; Fatehi, S.; Fusti-Molnar, L.; Ghysels, A.; Golubeva-Zadorozhnaya, A.; Gomes, J.; Hanson-Heine, M. W. D.; Harbach, P. H. P.; Hauser, A. W.; Hohenstein, E. G.; Holden, Z. C.; Jagau, T.-C.; Ji, H.; Kaduk, B.; Khistyaev, K.; Kim, J.; Kim, J.; King, R. A.; Klunzinger, P.; Kosenkov, D.; Kowalczyk, T.; Krauter, C. M.; Lao, K. U.; Laurent, A. D.; Lawler, K. V.; Levchenko, S. V.; Lin, C. Y.; Liu, F.; Livshits, E.; Lochan, R. C.; Luenser, A.; Manohar, P.; Manzer, S. F.; Mao, S.-P.; Mardirossian, N.; Marenich, A. V.; Maurer, S. A.; Mayhall, N. J.; Neuscamman, E.; Oana, C. M.; Olivares-Amaya, R.; O'Neill, D. P.; Parkhill, J. A.; Perrine, T. M.; Peverati, R.; Prociuk, A.; Rehn, D. R.; Rosta, E.; Russ, N. J.; Sharada, S. M.; Sharma, S.; Small, D. W.; Sodt, A.; Stein, T.; Stück, D.; Su, Y.-C.; Thom, A. J. W.; Tsuchimochi, T.; Vanovschi, V.; Vogt, L.; Vydrov, O.; Wang, T.; Watson, M. A.; Wenzel, J.; White, A.; Williams, C. F.; Yang, J.; Yeganeh, S.; Yost, S. R.; You, Z.-Q.; Zhang, I. Y.; Zhang, X.; Zhao, Y.; Brooks, B. R.; Chan, G. K. L.; Chipman, D. M.; Cramer, C. J.; Goddard, W. A.; Gordon, M. S.; Hehre, W. J.; Klamt, A.; Schaefer, H. F.; Schmidt, M. W.; Sherrill, C. D.; Truhlar, D. G.; Warshel, A.; Xu, X.; Aspuru-Guzik, A.; Baer, R.; Bell, A. T.; Besley, N. A.; Chai, J.-D.; Dreuw, A.; Dunietz, B. D.; Furlani, T. R.; Gwaltney, S. R.; Hsu, C.-P.; Jung, Y.; Kong, J.; Lambrecht, D. S.; Liang, W.; Ochsenfeld, C.; Rassolov, V. A.; Slipchenko, L. V.; Subotnik, J. E.; Van Voorhis, T.; Herbert, J. M.; Krylov, A. I.; Gill, P. M. W.; Head-Gordon, M. *Mol. Phys.* **2015**, *113* (2), 184–215.

(19) Cancès, E.; Mennucci, B.; Tomasi, J. *J. Chem. Phys.* **1997**, *107* (8), 3032–3041.

(20) Lange, A. W.; Herbert, J. M. *J. Chem. Phys.* **2011**, *134* (11).

(21) Lange, A. W.; Herbert, J. M. *Chem. Phys. Lett.* **2011**, *509* (1–3), 77–87.

(22) Mewes, J. M.; You, Z. Q.; Wormit, M.; Kriesche, T.; Herbert, J. M.; Dreuw, A. *J. Phys. Chem. A* **2015**, *119* (21), 5446–5464.

(23) Hirata, S.; Head-Gordon, M. *Chem. Phys. Lett.* **1999**, *314* (3–4), 291–299.

(24) Cossi, M.; Barone, V. *J. Chem. Phys.* **2001**, *115* (10), 4708–4717.

(25) Zimmerman, P. *J. Chem. Theory Comput.* **2013**, *9*, 3043–3050.

(26) Zimmerman, P. M. *J. Chem. Phys.* **2013**, *138* (18).

(27) Wohl, C. J.; Kuciauskas, D. *J. Phys. Chem. B* **2005**, *109* (47), 22186–22191.

(28) Tamai, N.; Miyasaka, H. *Chem. Rev.* **2000**, *100* (5), 1875–1890.

(29) Nuernberger, P.; Ruetzel, S.; Brixner, T. *Angew. Chemie - Int. Ed.* **2015**, *54* (39), 11368–11386.

(30) Hobley, J.; Pfeifer-Fukumura, U.; Bletz, M.; Asahi, T.; Masuhara, H.; Fukumura, H. *J. Phys. Chem. A* **2002**, *106* (10), 2265–2270.

(31) Hammarson, M.; Nilsson, J. R.; Li, S.; Beke-Somfai, T.; Andréasson, J. *J. Phys. Chem. B* **2013**, *117* (43), 13561–13571.

(32) Buback, J.; Nuernberger, P.; Kullmann, M.; Langhojer, F.; Schmidt, R.; Würthner, F.; Brixner, T. *J. Phys. Chem. A* **2011**, *115* (16), 3924–3935.

(33) Kohl-Landgraf, J.; Braun, M.; Özçoban, C.; Gonçalves, D. P. N.; Heckel, A.; Wachtveitl, J. *J. Am. Chem. Soc.* **2012**, *134* (34), 14070–14077.

(34) Rini, M.; Holm, A. K.; Nibbering, E. T. J.; Fidder, H. *J. Am. Chem. Soc.* **2003**, *125* (10), 3028–3034.

(35) Cottone, G.; Noto, R.; La Manna, G. *Chem. Phys. Lett.* **2004**, *388* (1–3), 218–222.

(36) Sheng, Y.; Leszczynski, J.; Garcia, A. A.; Rosario, R.; Gust, D.; Springer, J. *J. Phys. Chem. B* **2004**, *108* (41), 16233–16243.

(37) Buback, J.; Kullmann, M.; Langhojer, F.; Nuernberger, P.; Schmidt, R.; Würthner, F.; Brixner, T. *J. Am. Chem. Soc.* **2010**, *132* (46), 16510–16519.

Chapter 6

Hydroxocobalamin and Aquocobalamin

The following contribution covering the photostability of hydroxocobalamin is adapted from the paper "Photostability of hydroxocobalamin: Ultrafast Excited State Dynamics and Computational Studies" published in the Journal of Physical Chemistry Letters (DOI: 10.1021/acs.jpclett.5b02333)[1]. The chapter will conclude with unpublished work concerning the comparison of the ultrafast dynamics of aquocobalamin to hydroxocobalamin, examining the effects of solvent polarity, pH, and excitation wavelength on the excited state dynamics.

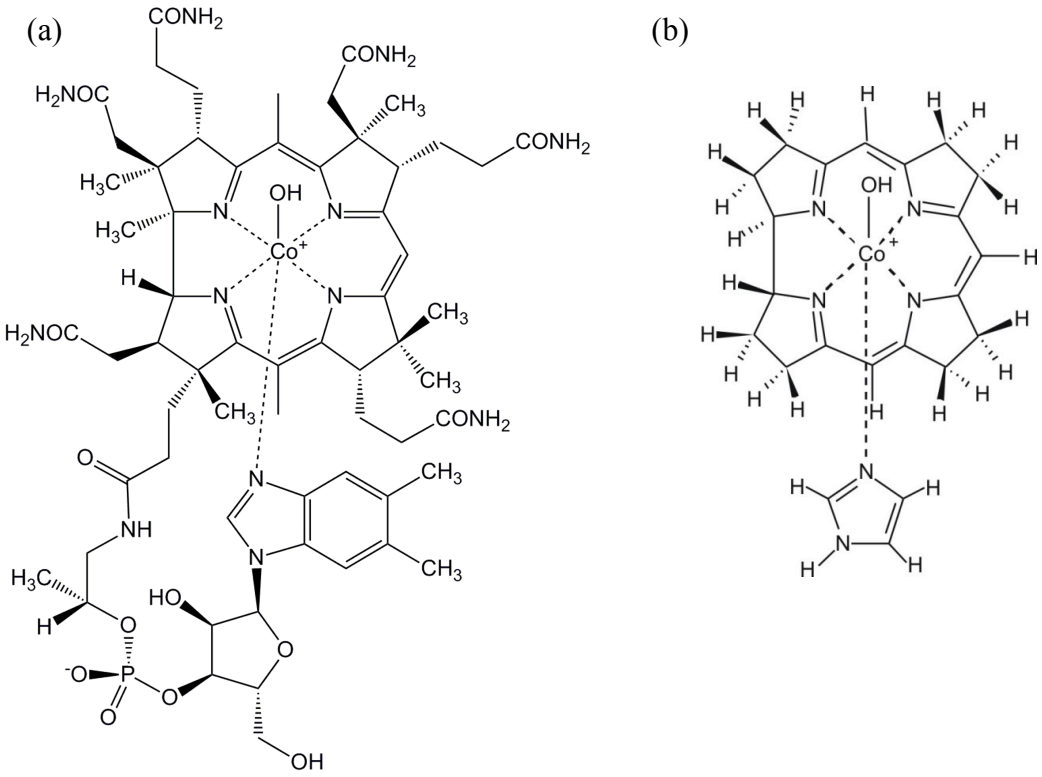

Figure 6.1. (a) Molecular structure of hydroxocobalamin (HOCbl), and (b) truncated structure of hydroxocobalamin used in TDDFT calculations.

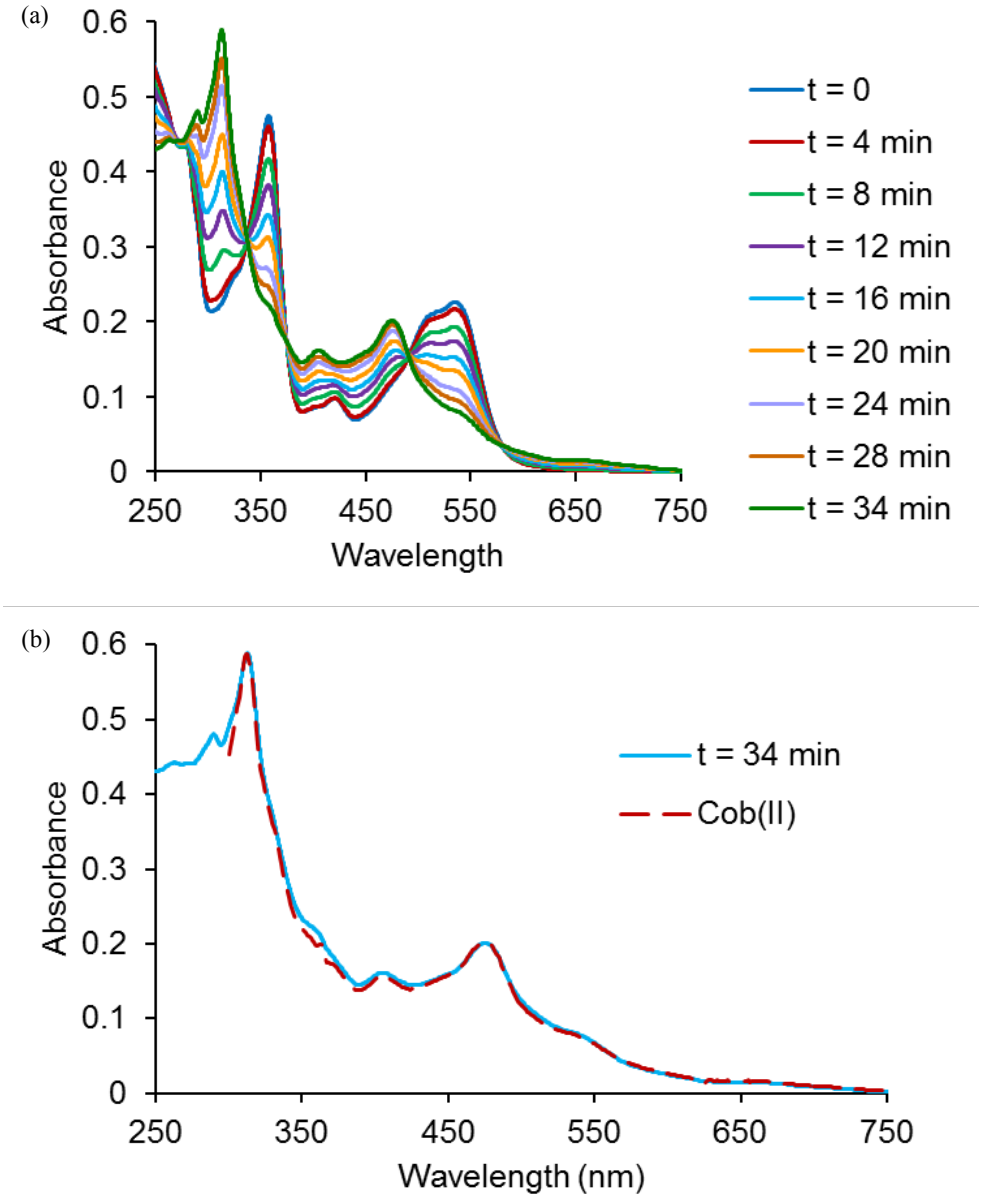

Figure 6.2 (a) Photolysis of HOCbl using an unfiltered mercury pen lamp. (b) The final spectrum is consistent with the cob(II)alamin spectrum obtained following excitation of alkylcobalamins (red dashed line), indicating that the photolysis has gone to completion.

Hydroxocobalamin Photochemistry. Hydroxocobalamin (HOCbl, Figure 6.1) a biologically inactive form of vitamin B_{12} has generated considerable interest since the recent work of Shell

and Lawrence, where photolysis of HOCbl in the presence of oxygen was used to cleave plasmid DNA.[2] Application of hydroxyl radicals generated photochemically via homolytic cleavage of the Co-OH offers many advantages in comparison to standard methods, such as the Fenton reaction using Fe^{II} EDTA and H_2O_2. One of the most important advantages to using HOCbl is the possibility of intracellular temporal control of light dependent photoinitiated reactions, in contrast to chemical methods, where initiation and termination of the radical reaction cannot be precisely controlled. However, the mechanism for the photochemical production of hydroxyl radical from HOCbl is unclear. Although alkylcobalamins undergo ready photolysis to produce radicals, non-alkylcobalamins are generally photostable.[3] HOCbl is no exception. Anaerobic photolysis in the presence of a radical scavenger such as sodium benzoate or sorbitol exhibits no measurable photolysis for wavelengths >350 nm. In contrast, photolysis to cob(II)alamin is readily observed following excitation at 253 nm. Photolysis is also observed with a Xe lamp using a Pyrex filter to limit the UV, but the rate is ~2000 times slower than the comparable photolysis of adenosylcobalamin. The threshold for photolysis falls between 300 nm and 350 nm, Figure 6.2.

To explore the mechanism for photochemical production of hydroxyl radicals from HOCbl, broadband femtosecond UV-Visible transient absorption spectroscopy was used to characterize the excited electronic states of HOCbl and the results compared with TDDFT calculations of the potential energy surface of the lowest excited electronic states. An earlier measurement of HOCbl was performed at a pH where the sample was a mixture of DOCbl and D_2OCbl complicating the interpretation.[4] The excited state lifetime of H_2OCbl is substantially shorter than that of HOCbl.[3–5] The sample used here was buffered at pH 10.3 where 99+% of the compound is expected to be HOCbl (pK_a ~8).[6] The measurements were performed using 404 nm

excitation where no photolysis is expected and 269 nm excitation where photolysis to cob(II)alamin is observed in steady state measurements. The probe was a white light continuum (350 nm to 800 nm) and (270 nm to 600 nm) allowing characterization of transient species in the UV-visible region of the spectrum. Typical transient spectra are plotted in Figure 6.3.

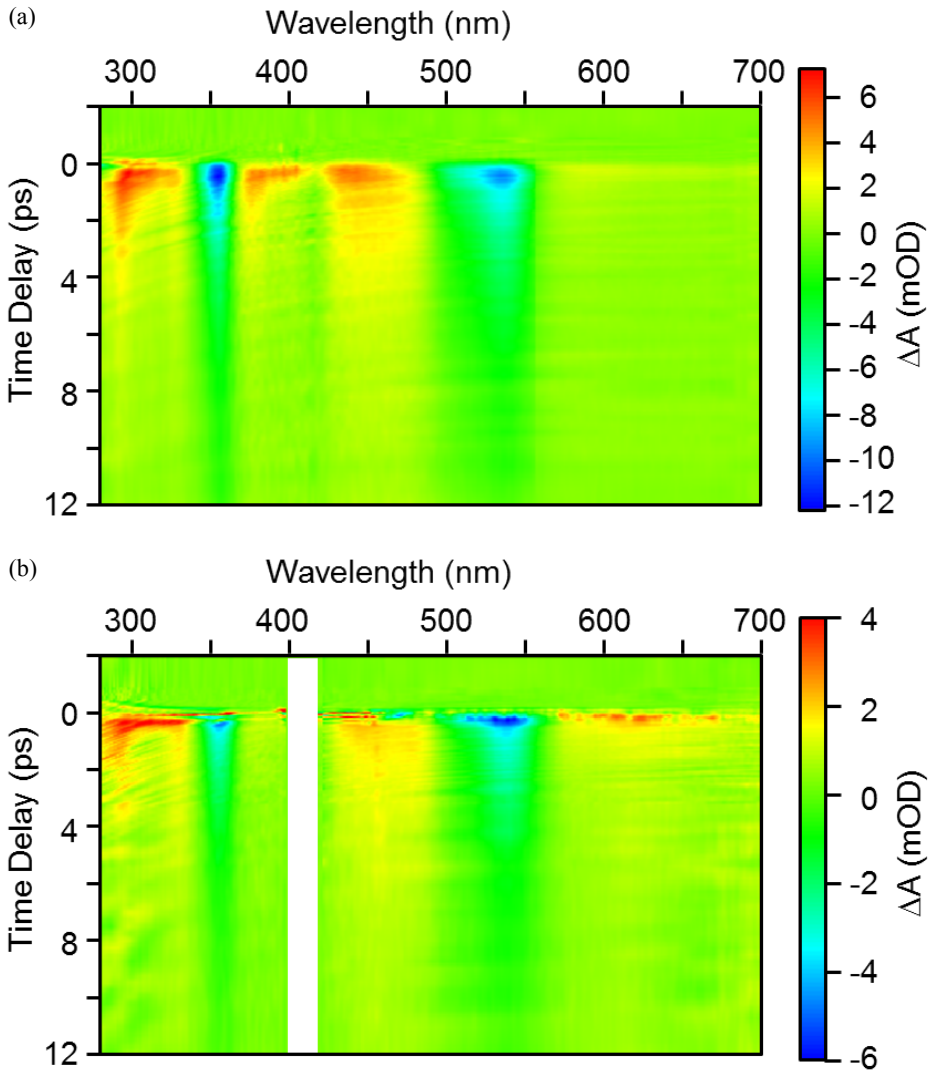

Figure 6.3. (a) Contour plot of the transient absorption data following excitation at 269 nm. (b) Contour plot of the transient absorption data following excitation at 404 nm.

The data were fit to a sum of exponentials using a global analysis program.[7] In all cases the data are well modeled using two exponential decay components: $\tau_1 = 0.32 \pm 0.08$ ps and

τ_2 = 5.50 ± 0.17 ps. There may be a faster component as well, but analysis at short time-delays is complicated by coherent signals from both solvent and solute. The fits are summarized in Figure 6.4 and Figure 6.5.

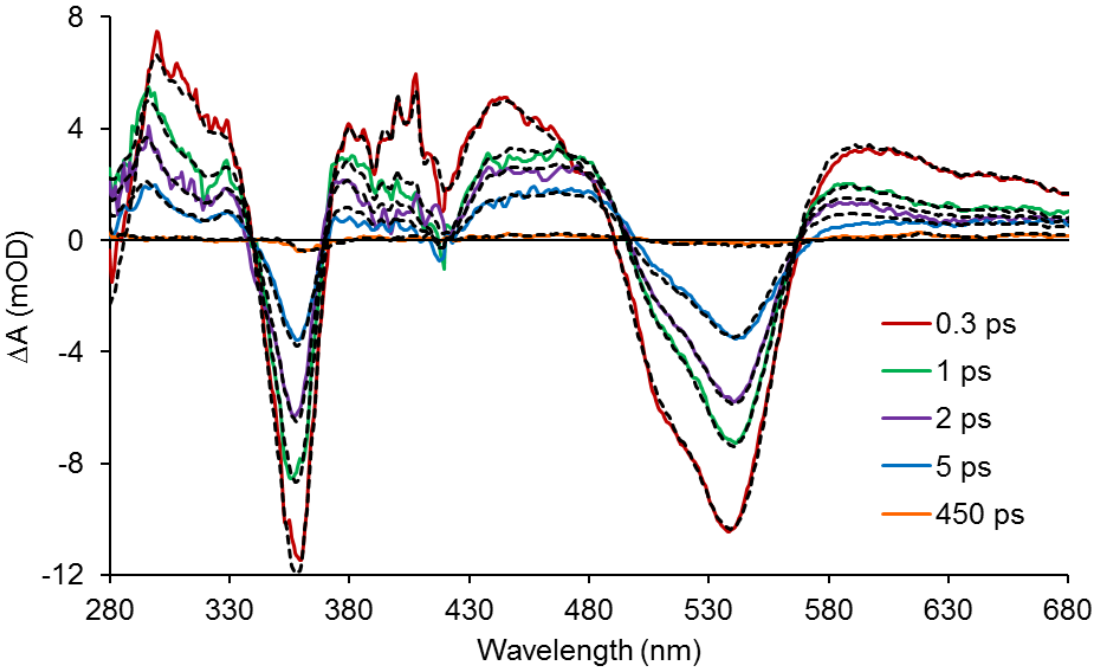

Figure 6.4. Fits to the transient absorption data following excitation at 269 nm at select time delays. Although there may be a small residual photoproduct yield following 269 nm excitation (<1.5%), overall the transient data are similar for both excitation wavelengths.

Following 404 nm excitation the transient absorption signal decays to baseline. The noise level of the measurement sets an upper limit of <1% on the photolysis yield. Following 269 nm there is evidence for a photolysis yield of ca. 1.5% in a persistent, long-lived component which has spectral signatures consistent with cob(II)alamin formation, Figure 6.6. The steady state photolysis measurements set an upper limit much less than 1% following 404 nm excitation but are consistent with a 1 to 2% yield following 269 nm excitation.

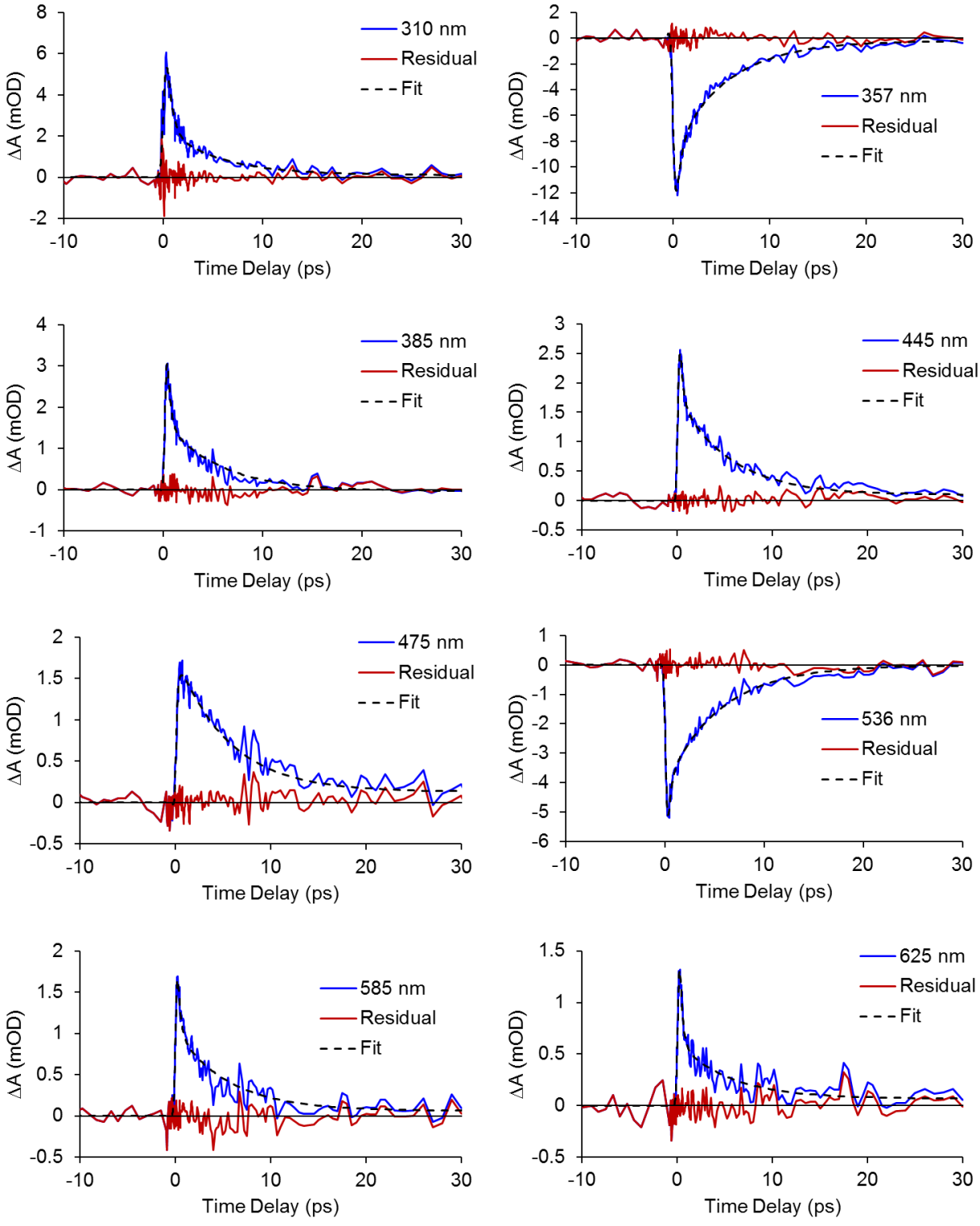

Figure 6.5. Select kinetic traces and fits following excitation at 269 nm.

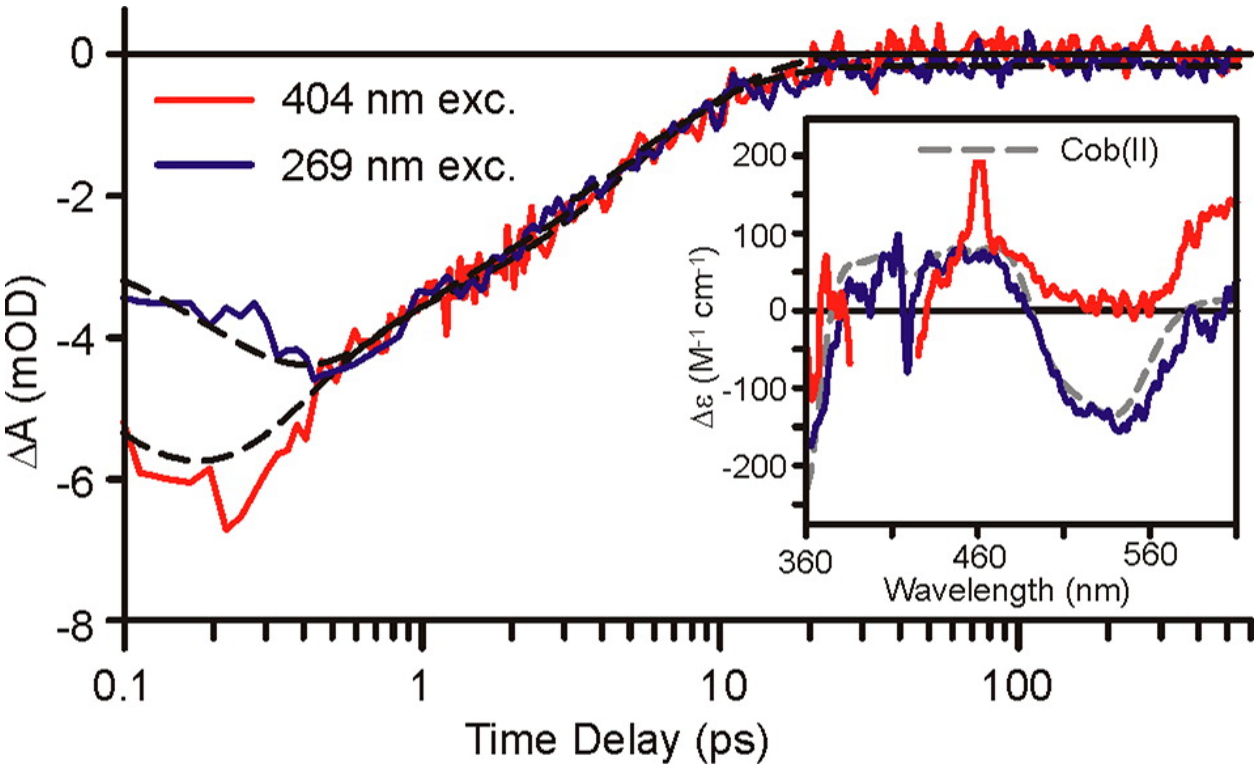

Figure 6.6. Comparison of time traces at 540 nm following 269 nm excitation and 404 nm excitation. The inset compares the residual difference spectrum at time delays >100 ps with the steady state difference spectrum for photolysis to cob(II)alamin. These data set an upper limit of <1% photolysis yield following 404 nm excitation and 1.5% ± 0.5% photolysis yield following 269 nm excitation.

To interpret the transient spectra we assume a sequential model where excitation produces an excited state, i.e., S_n, either directly or following rapid (<100 fs) internal conversion and the S_n state decays to populate the lowest excited singlet state S_1 in 0.32 ± 0.08 ps. The S_1 state decays back to the ground state in 5.50 ± 0.17 ps. The decay associated difference spectra (DADS) obtained from the amplitudes of the fit to the data can be used to construct the species associated difference spectra (SADS) as described in Chapter two. The SADS for the S_n and S_1 state are summarized in Figure 6.6. The difficulty in separating a coherent component from the S_n contribution following 404 nm excitation results in the larger noise level observed in this SADS.

The SADS can be used to estimate the species associated excited state spectra by adding the appropriate ground state contribution back into the difference spectra: $A(\lambda) = \Delta A(\lambda) + \alpha A_{GS}(\lambda)$ where α is the fraction of the ground state excited by the pump pulse.[5,8,9] These estimated spectra are placed on an absolute scale using the known extinction coefficients for HOCbl and plotted in Figure 6.6.

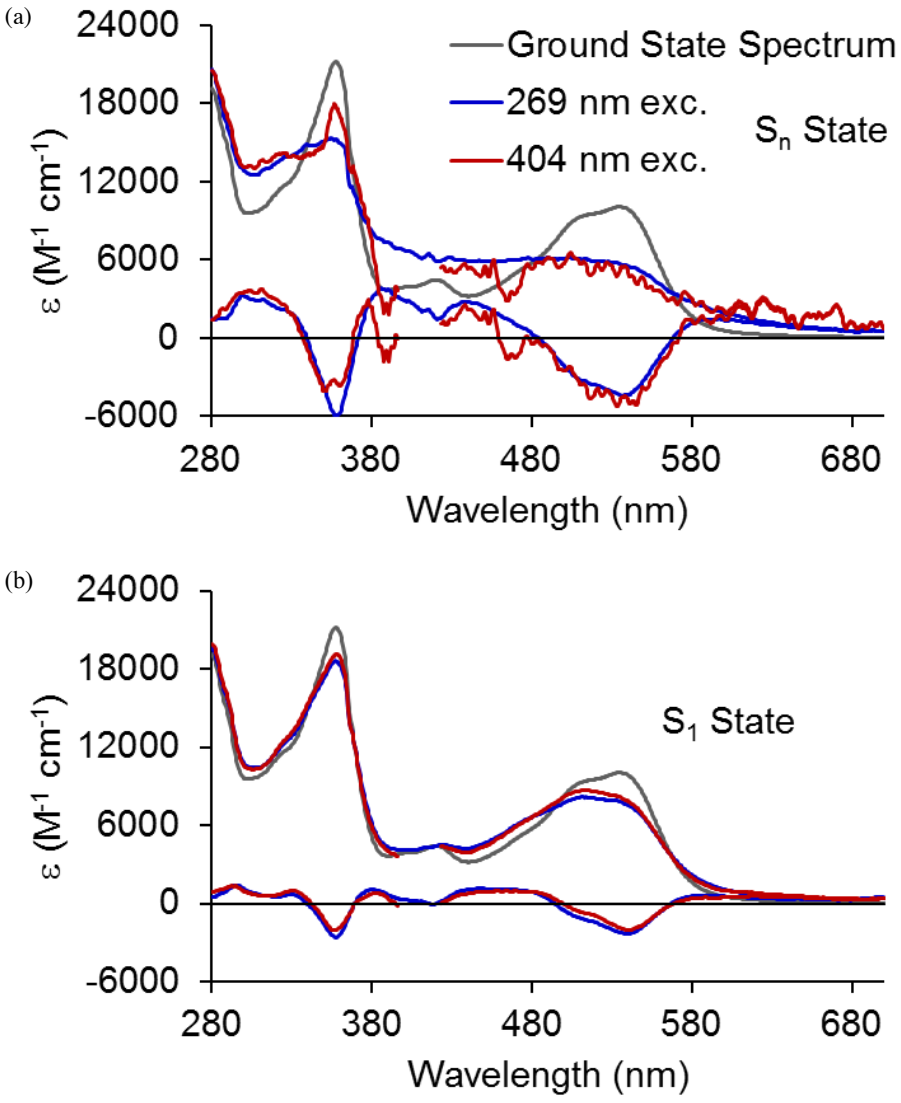

Figure 6.7. Excited state spectra estimated from the SADS for the (a) S_n state and the (b) S_1 state. The excited population is ca. 8% following 404 nm excitation and 13% following 269 nm excitation

The spectrum of the S_n state is broad, extending across the entire spectral window. The S_1 spectrum is structured, resembling the ground state spectrum. The excited state spectra suggest that the S_n state is characterized by significant elongation of the axial bonds while the S_1 state has a geometry similar to that of the ground state. This is in contrast to the significant displacement observed for the S_1 state of cyanocobalamin.[5,8,9]

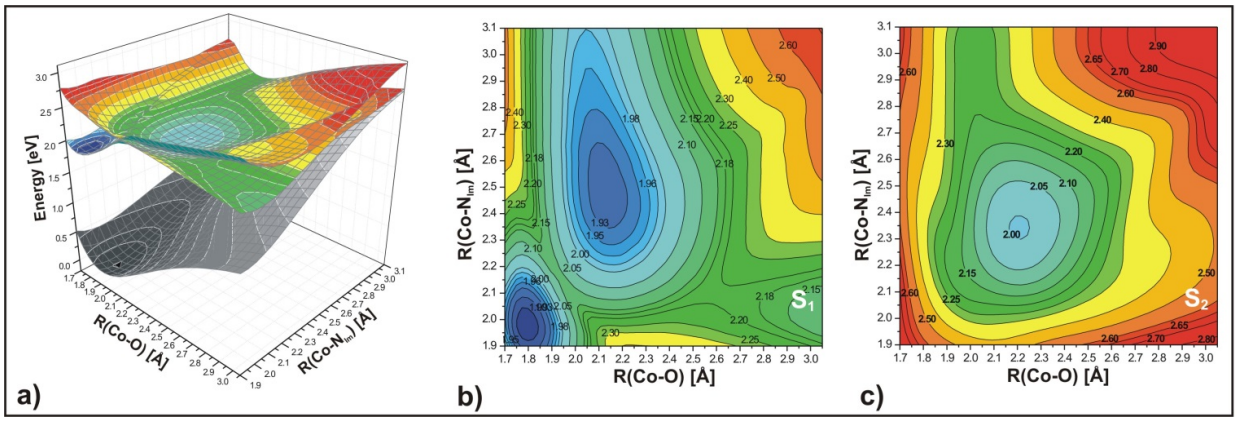

Figure 6.8. (a) Potential energy surfaces for the ground and two lowest singlet states of the Im-[Co^{III}(corrin)]-OH$^+$ model complex generated as vertical excitations and plotted as a function of axial bond lengths (expressed in Å). (b) Vertical projections of the S1 potential energy surface. (c) Vertical projections of the S2 potential energy surface.

Comparison with theory. The following section of the published work, "Photostability of hydroxocobalamin: Ultrafast Excited State Dynamics and Computational Studies," is based on theoretical simulations by our collaborators: Piotr Lodowski, Maria Jaworska, and Pawel M. Kozlowski. Their work involves calculating the ground and excited state potential energy surfaces for hydroxocobalamin using TDDFT.

To explore the nature of the low-lying excited states of HOCbl, density functional theory (DFT) and time-dependent DFT (TDDFT) were applied to obtain corresponding potential energy surfaces (PESs). Figure 6.8 shows these PESs as a function of axial bond lengths. These surfaces

were generated using a structural model of HOCbl truncated with respect to side chains (Figure 6.1), employing the BP86/TZVPP level of theory (TZVP basis sets for hydrogen) in all calculations. The energy surfaces corresponding to the lowest excited state (S_1) consists of at least three different electronic states. The involvement of two of them is apparent from the presence of two energy minima, one at shorter Co-OH and Co-N_{Im} distance, and the second at just a slightly elongated Co-OH distance and much longer Co-N_{Im} length. The third state appears on the PES at a Co-OH distance of about 2.5 – 2.6 Å and within a Co-N_{Im} range of 1.9 – 2.3 Å, (i.e., the lower right corner of Figure 6.8b). This part of the S_1 PES has dissociative character, consistent with R(Co-OH) energy curves reported previously[10] and involves higher excited states, Figure 6.8. Due to the instability of the wavefunction associated with TD-DFT calculations, this section of the PES cannot be computationally characterized. The minimum energy of the S_1 state has dominant $p_{OH}/d \rightarrow \pi^*$ character at short Co-OH distance. Upon Co-OH bond elongation, the S_1 state crosses with higher excited states with dominant σ^* contributions and changes character from $p_{OH}/d \rightarrow \pi^*$ to $p_{OH}/d \rightarrow \sigma^*$. For long Co-OH distances S_1 surface has mainly $p_{OH} \rightarrow \sigma^*$ character with small contribution from d orbital of cobalt.

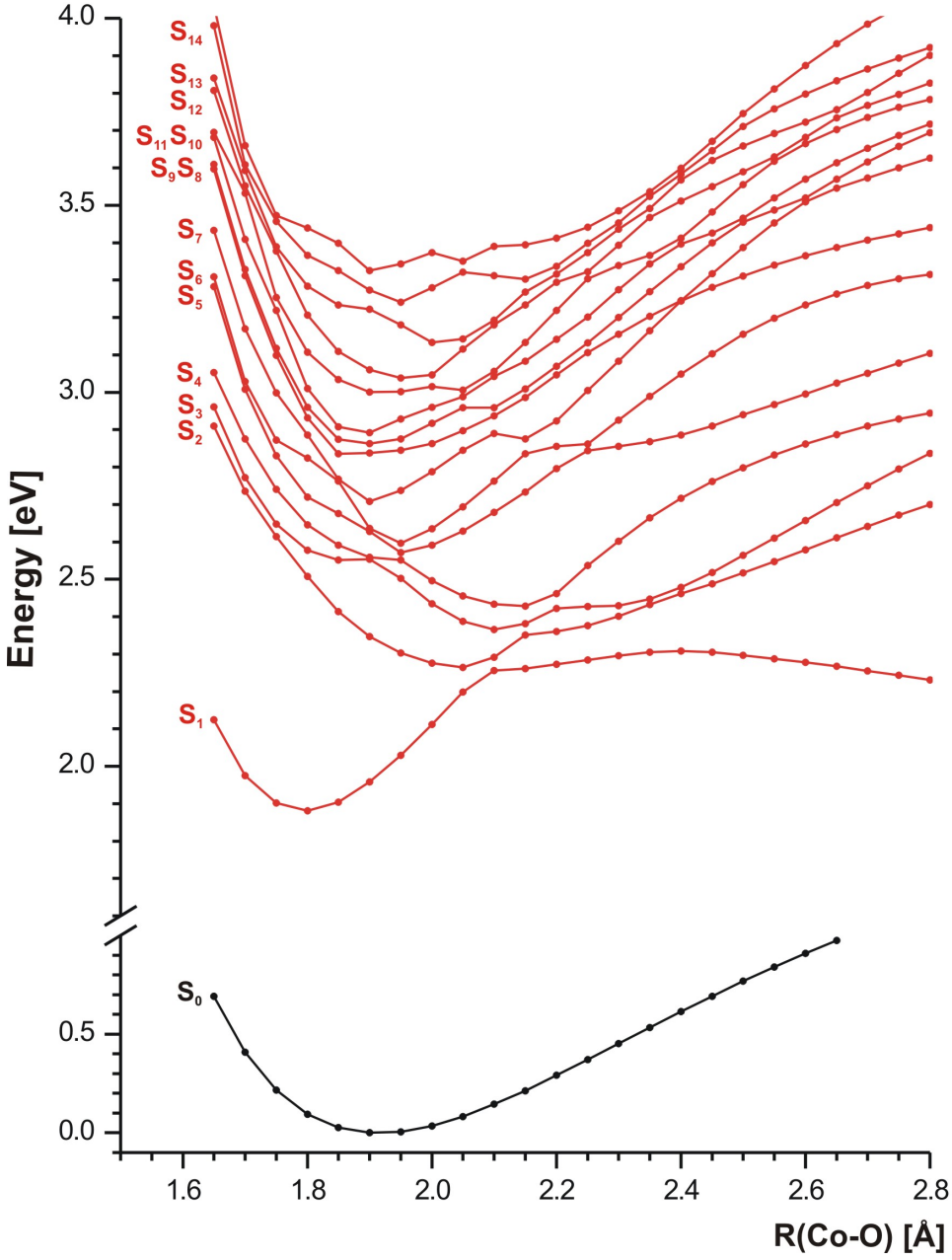

Figure 6.9. Potential energy curves of the ground and lowest singlet excited states of the Im-[Co^{III}(corrin)]-OH^+ model complex along the Co-C bond stretch computed at the ground state optimized geometry. (Figure reproduced from ref 1 supplemental information Fig. S9)

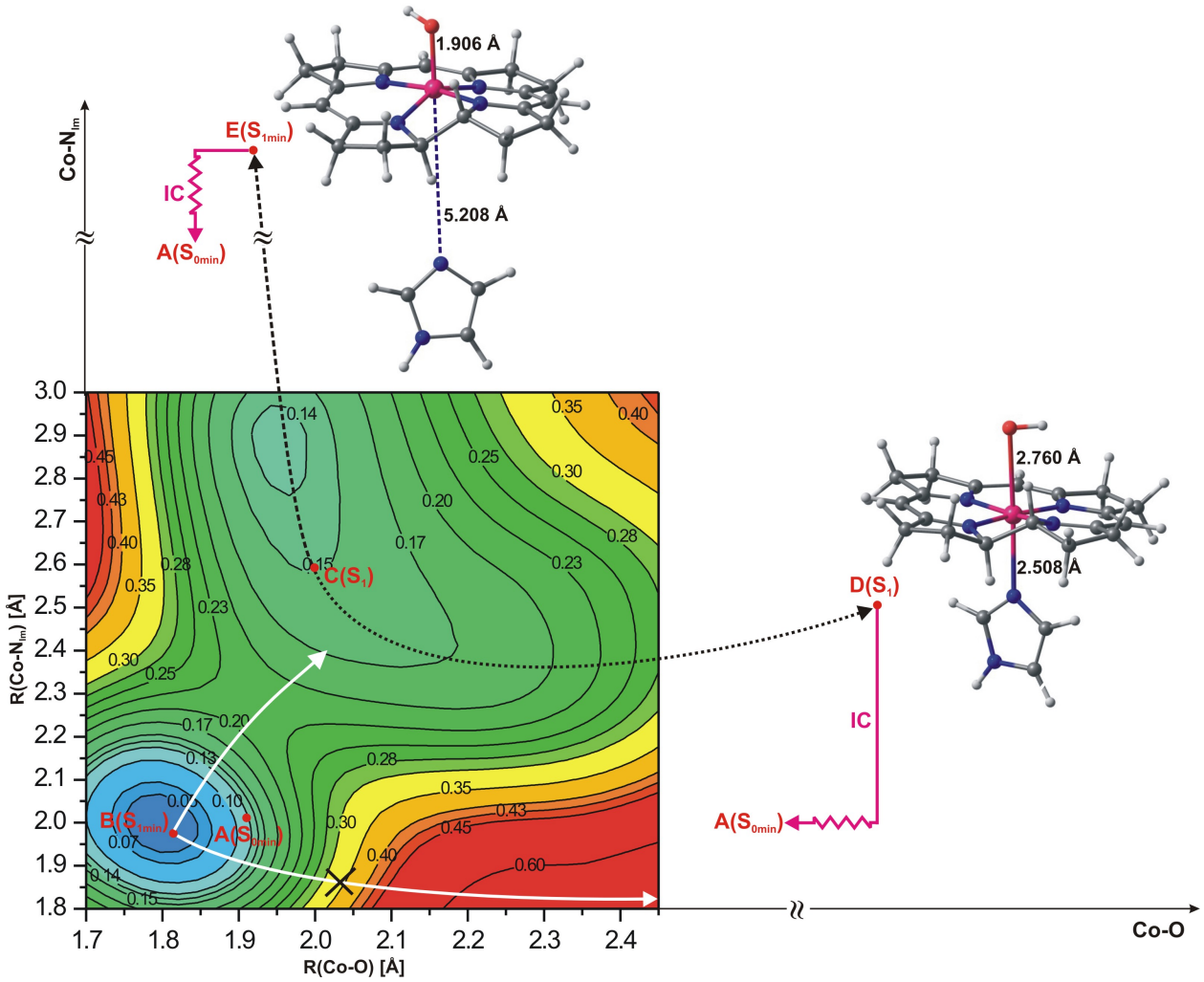

Figure 6.10. Potential energy surface for the S_1 electronic state of the Im-[Co^{III}(corrin)]-OH^+ model complex in the optimized geometry of the excited state plotted as a function of axial bond lengths.

(Figure reproduced from ref. 1 Supplemental Information Figure S10)

To obtain a more realistic description of the PES associated with the S_1 state, the geometry of the lowest excited state was optimized as a function of axial bond lengths, for ranges where it was possible, Figure 6.9. Overall, the PES corresponding to an adiabatic description of S_1 state does not differ significantly from one generated via vertical excitations. Optimized S_1 axial bond lengths do not differ significantly from those of the ground state as summarized in Figure 6.10. This is indeed in sharp contrast with CNCbl, where changes are rather significant.[11–14]

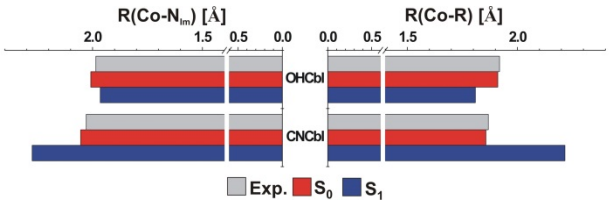

Figure 6.11. Comparison of Co-R and Co-N_{Im} bond lengths for Im-[Co^{III}(corrin)]-OH^+ and Im-[Co^{III}(corrin)]-CN^+ model complexes (red – in S_0 optimized geometries, blue - in S_1 optimized geometries, grey – experimental S_0 data).

Closer inspection of the optimized S_1 PES reveals that crossing of the $p_{OH}/d\rightarrow\pi^*$ and $p_{OH}/d\rightarrow\sigma^*$ states takes place when the Co-OH bond length is between 1.85 – 2.00 Å. The $p_{OH}/d\rightarrow\sigma^*$ state is the same as that obtained from vertical excitations, but with more contribution from cobalt d orbitals. Excited vertical state S_2 about $p_{OH}/d\rightarrow\sigma^*$ character during geometry relaxation lowers in energy and becomes the low-lying S1 electronic state. In the excited state, the Co-O bond has rather weak bonding character and for stretched Co-OH distances may cross with the ground state (S_0) leading to deactivation. It can be further proposed that the proximity of S_0/S_1 surfaces may lead to deactivation through two possible channels, Figure 6.9: (a) the first involves elongation and detachment of the axial base followed by corrin ring distortion, (i.e., $B(S_{1min}) \rightarrow C(S_1) \rightarrow E(S_{1min})$ path), a mechanism similar to MeCbl,[14,15] or (b) simultaneous elongation of both axial bonds,(i.e., $B(S_{1min}) \rightarrow C(S_1) \rightarrow D(S1)$ path) a mechanism similar to CNCbl.[14]

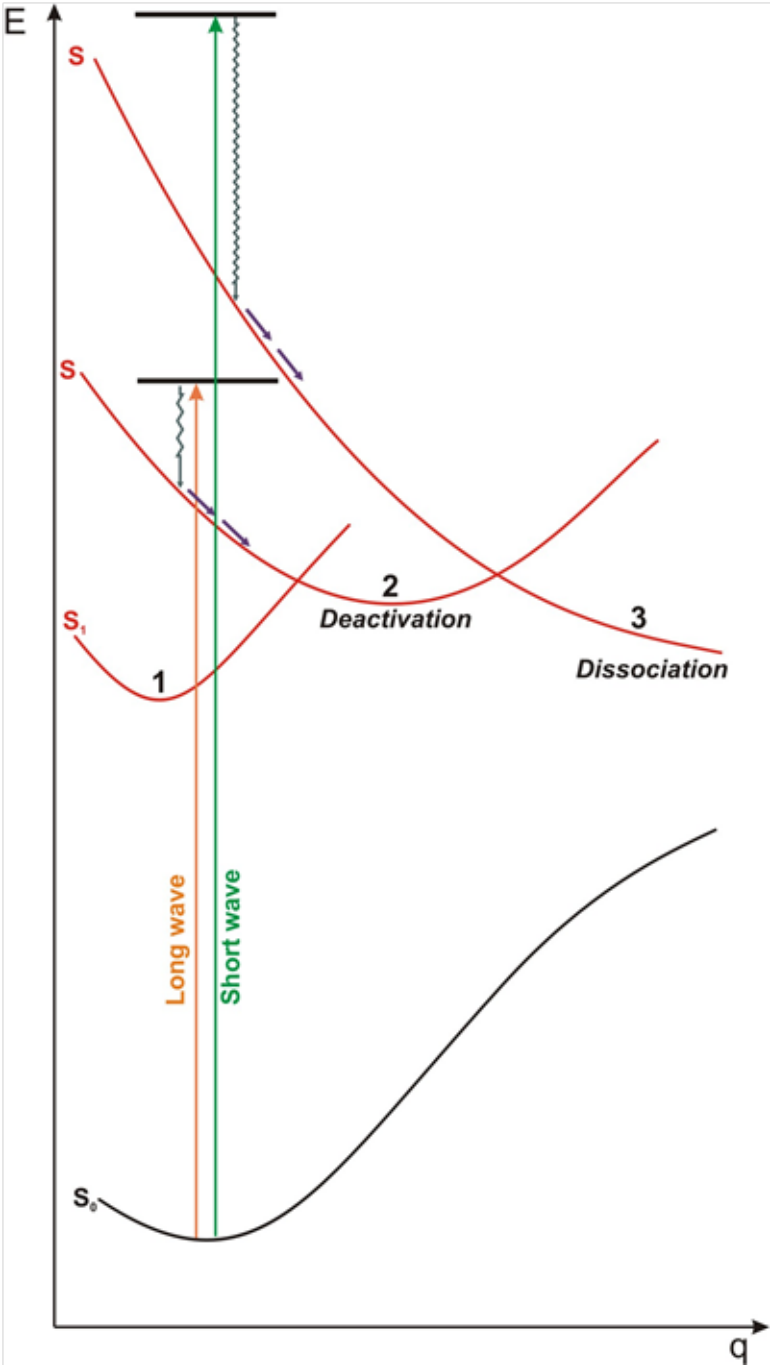

Figure 6.12. Scheme of potential energy curves involved in in the process of the deactivation and dissociation

The results of femtosecond UV-Visible transient absorption spectroscopy, in particular the photostability of HOCbl can be explained assuming the model shown in Figure 6.12. Because the lowest PES consists of at least three different electronic states (1-3), excitations using longer

wavelengths leads effectively to population of the energy minimum corresponding to the $p_{OH}/d \rightarrow \sigma^*$ electronic state (2), which is primarily responsible for deactivation. On the other hand, excitations with shorter wavelengths can populate a repulsive electronic state, with likely dominant $p_{OH}/d \rightarrow \sigma^*$ or $d/p_{OH} \rightarrow \sigma^*$ character, which at longer Co-OH distances becomes dissociative (3).

The comparison of steady state photolysis measurements, transient absorption measurements, and theoretical calculations provide a consistent picture of the photo-induced formation of OH· radicals from HOCbl. The comprehensive picture will help guide the *in situ* application of HOCbl photolysis as well as the potential photochemical applications of other B_{12} compounds. The relative energies of the three interacting states identified here control the photochemistry and photophysics of many B_{12} compounds and analogs.

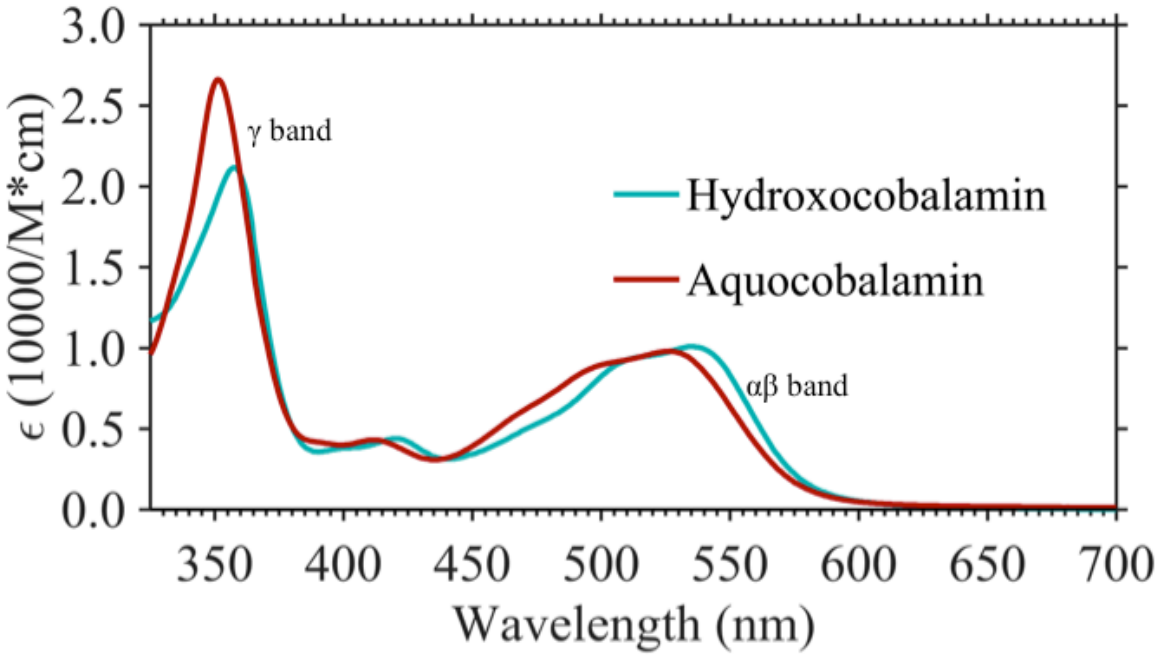

Figure 6.13. UV-vis spectra of HOCbl and H_2OCbl. The γ band for HOCbl is centered at 355 nm and 351 nm for H_2OCbl. The αβ band for HOCbl is red-shifted with respect to H_2OCbl.

Aquocobalamin Photochemistry. The pKa of the Co-OH group in hydroxocobalamin is about 7.8. Previous studies[3–5] conducted on hydroxocobalamin have actually been a mixture of hydroxo- and aquocobalamin, since they were carried out in pure water or buffers with pH close to 7.8. There are key differences between the UV-vis spectra of hydroxo- and aquocobalamin, Figure 6.13. Their excited state dynamics differ as well.

Ultrafast transient absorption spectra of aquocobalamin were collected in 11 mM pH 5 carbonate buffer to ensure that > 99% of the sample was in the protonated aquocobalamin form. Pump wavelengths including 269, 404, 540, and 560 nm were used, giving very similar transient absorption results. Typical results are shown Figure 6.14.

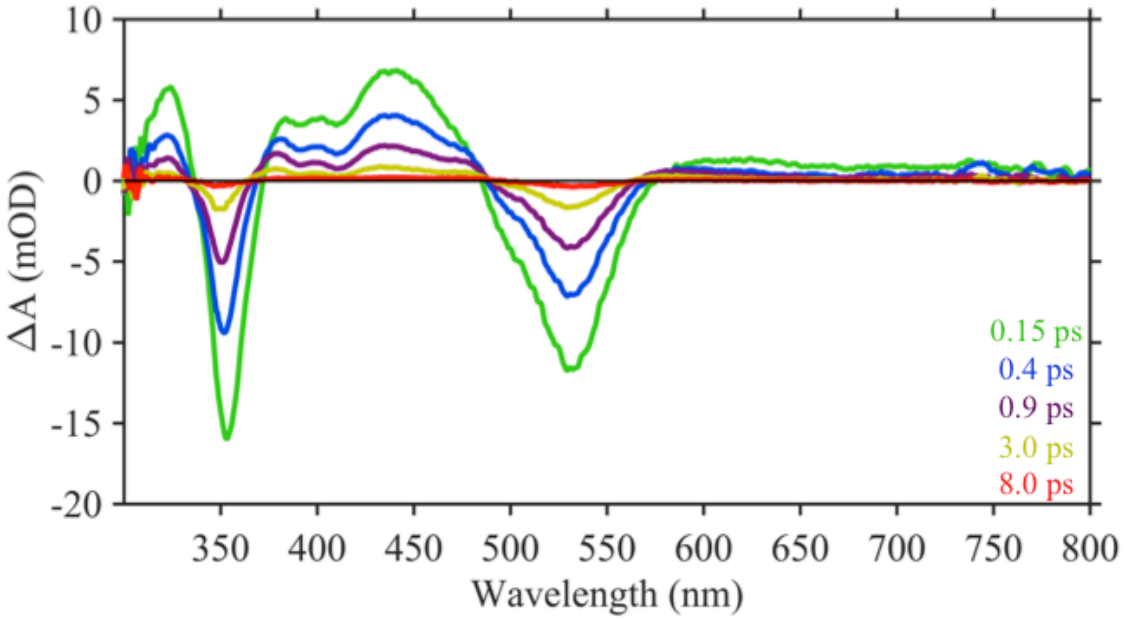

Figure 6.14. Transient absorption spectra of H_2OCbl excited with 560 nm.

The data in Figure 6.14 were collected in a wired guided flow, using a 560 nm pump wavelength at magic angle to the probe (320 – 800 nm). A sum of two exponentials were used to fit the data using a global analysis program.[6] In all cases the data are well modeled using two

exponential decay components: $\tau_1 = 0.25 \pm 0.11$ ps and $\tau_2 = 1.9 \pm 0.4$ ps. There may be a faster component as well, but analysis at short time-delays is complicated by coherent signals from both solvent and solute.

Several previous studies[8,9] have demonstrated that the spectrum of the S_1 state determined from TA reports on changes in the geometry of the upper and lower axial ligands of the cobalt. As mentioned above, geometry of the S_1 state in hydroxocobalamin is expected to be very similar to the ground state. In the case of aquocobalamin, the geometry of the S_1 state is even closer to the ground state because the overall magnitude of the difference in the TA is much smaller. In hydroxocobalamin, the bleach of the αβ band in the S_1 SADS is about 60% of the initial bleach, while in aquocobalamin the bleach of the αβ band in the S_1 SADS is about 25% of the initial bleach, Figure 6.15. The S_1 excited state spectrum of aquocobalamin is more similar to the ground state spectrum than the S_1 excited state spectrum of hydroxocobalamin.

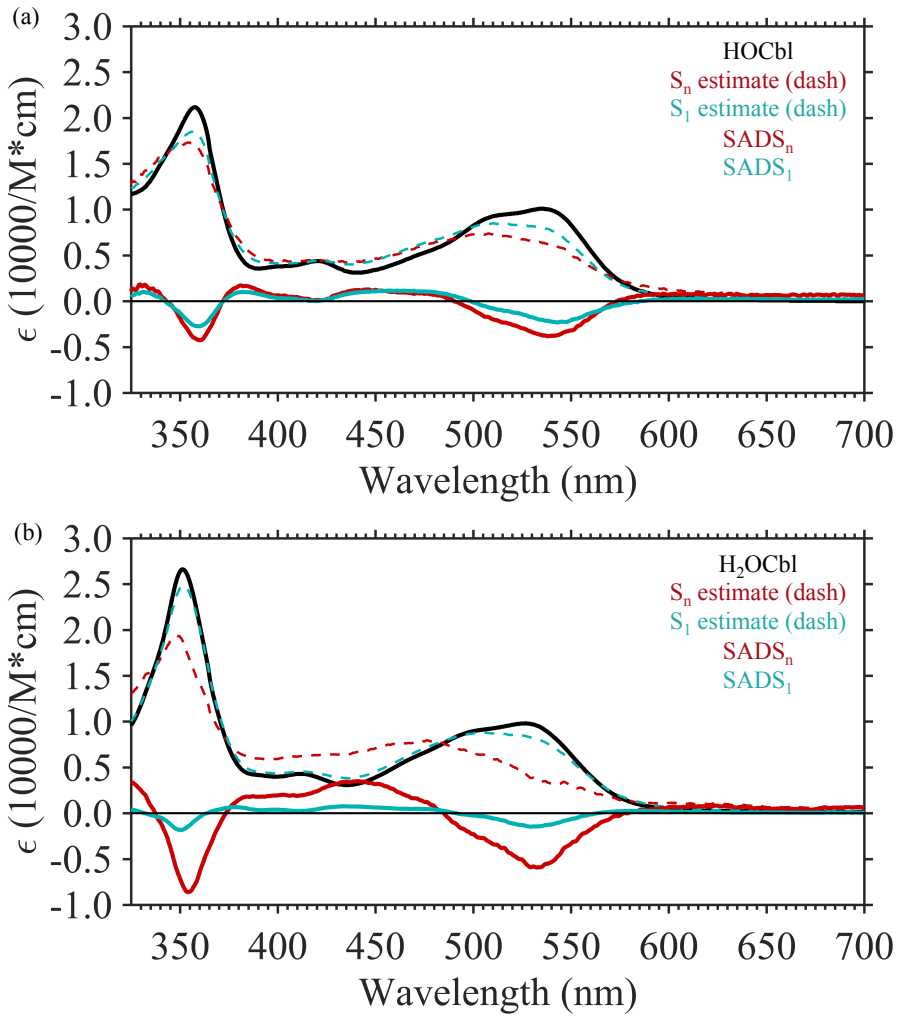

Figure 6.15. (a) HOCbl spectra: ground state (black), estimates of S_n (red dash) and S_1 states (blue dash), and SADS of S_n (solid red) and S_1 (solid blue), (b) H_2OCbl spectra: ground state (black), estimates of S_n (red dash) and S_1 states (blue dash), and SADS of S_n (solid red) and S_1 (solid blue).

Polarization studies. To further investigate the differences in the electronic states of hydroxocobalamin and aquocobalamin, the anisotropy of the transient absorption was collected using 404, 535 and 560 nm as pump wavelengths. Since hydroxocobalamin and aquocobalamin are large heavy molecules, and their excited state lifetimes are fairly short, the rotational diffusion of the molecule does not contribute to the anisotropy signals. The anisotropy of the S_1

species is calculated by the same procedure described in Chapter 3. The anisotropy of the S_n and S_1 species of HOCbl excited by 560 nm and H_2OCbl excited by 570 nm are shown in Figure 6.16.

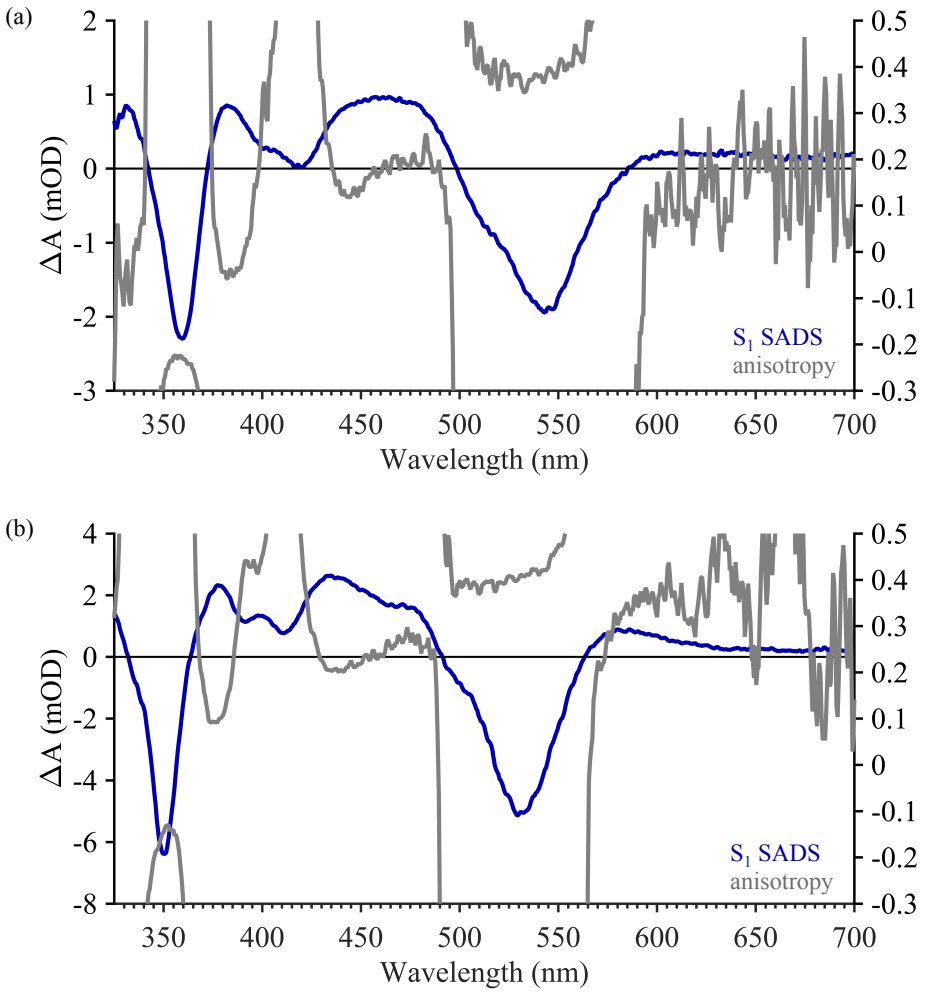

Figure 6.16. (a) Hydroxocobalamin S_1 SADS spectrum (blue) and the anisotropy of that species (grey), (b) Aquocobalamin S_1 SADS spectrum (blue) and the anisotropy of that species (grey).

Further analysis is needed characterize the anisotropy in detail. The data are complicated by many overlapping ground and excited state transitions. A key difficulty in a detailed analysis is uncertainty in the spectrum of the S_1 state. The S_1 state is estimated by adding a scaled amount of

the ground state spectrum into the S_1 SADS. Without a detailed analysis of the precise amount of excited molecules, it is difficult to accurately estimate the correct amount of ground state to add to the S_1 SADS. In addition, there are too many parameters in a least squares fits of the data to be confident at this point. However, certain gross details are evident in the data without an exhaustive analysis. As expected, the γ band and the αβ bands are polarized ~ 90° to each other[15,16]. When exciting the αβ band, an anisotropy of 0.4 is obtained and an anisotropy of -0.2 is obtained for the γ band. Also, the DE-band transition appears to be at roughly magic angle with respect to both the γ band and αβ band. Thus, DE-band transition dipole moment may be out of the plane of the corrin ring.

Solvent Dependence. The excited state dynamics of HOCbl and H_2OCbl were measured in a 1:1 mixture of ethanol and aqueous buffer. The HOCbl and H_2OCbl data are globally fit to a sum of two exponentials, however the lifetimes obtained from the fit are longer than those in aqueous buffer. The timescale for recovery to the ground state of HOCbl is τ_2 = 7.3 ps, and the timescale for H_2OCbl ground state recovery is τ_2 = 3.8 ps. These results are expected and observed for other cobalamins in other studies[3,8,9]. This effect is explained by stabilization of the S_1 state by more polar solvents. Figure 6.17 demonstrates the increase of the lifetime of the S_1 state in a 1:1 buffer:ethanol mixture relative to aqueous buffer.

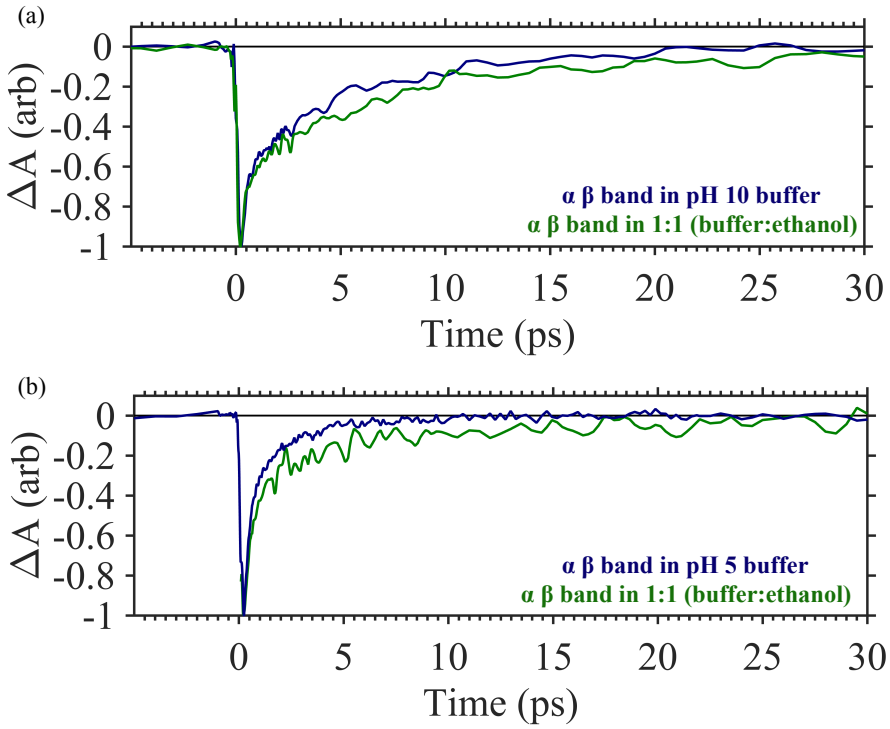

Figure 6.17. Normalized kinetic lineouts of the αβ band (a) HOCbl integrated from 530 to 550 nm and (b) H_2OCbl integrated from 515 to 545 nm. Green is in a 1:1 buffer:ethanol mixture, blue is in buffer.

Conclusions.

Hydroxocobalamin and aquocobalamin are non-alkylcobalamins, which have been demonstrated to function as photoactivated radical delivery reagents if irradiated with wavelengths < 350 nm. This is a result of a dissociative pathway forming on a region of the S_1 PES that likely has σ^* character. This region of the PES can only be accessed by excitation to high-energy excited states. This interesting property has attracted the interest of chemists and biochemists in need of light activated hydroxyl radical catalysts. HOCbl and H_2OCbl provide a new alternative to the Fenton reaction to deliver hydroxyl radicals in a more controllable fashion activated by UV irradiation.

In addition, previously reported experiments were likely examining a mixture of HOCbl and H_2OCbl. We show here the two species have different excited state lifetimes and previously reported lifetimes can be explained as weighted averages of HOCbl and H_2OCbl. Future studies of HOCbl must be careful to account for the pH of the solution. For example, biological studies where HOCbl is a relevant species typically take place at physiological pH (7.4). Physiological pH is close to the pKa of the Co-OH (pKa = 8), and as a result the solution will actually be ~ 80 % H_2OCbl and ~ 20 % HOCbl.

Transient absorption of HOCbl and H_2OCbl indicate the spectra of the S_1 state between the two molecules are somewhat different. The S_1 excited state spectrum of HOCbl shows greater differences than the ground state spectrum, while the S_1 spectrum of H_2OCbl is much more similar to the ground state spectrum. These results can be interpreted in terms of relative displacements of the upper and lower axial ligands. HOCbl is likely to have much more elongation of its axial ligands in the S_1 state relative to H_2OCbl. Efforts to further understand the differences of the electronic states of HOCbl and H_2OCbl have gone in the direction of TA anisotropy, however these data are difficult to accurately analyze.

Notes on Chapter 6

(1) Wiley, T. E.; Miller, W. R.; Miller, N. A.; Sension, R. J.; Lodowski, P.; Jaworska, M.; Kozlowski, P. M. *J. Phys. Chem. Lett.* **2016**, *7* (1), 143–147.

(2) Shell, T. A.; Lawrence, D. S. *J. Am. Chem. Soc.* **2011**, *133* (7), 2148–2150.

(3) Shiang, J. J.; Cole, A. G.; Sension, R. J.; Hang, K.; Weng, Y.; Trommel, J. S.; Marzilli, L. G.; Lian, T.; Arbor, A. *J. Am. Chem. Soc.* **2006**, *128* (3), 801–808.

(4) Jones, A. R.; Russell, H. J.; Greetham, G. M.; Towrie, M.; Hay, S.; Scrutton, N. S. *J. Phys. Chem. A* **2012**, *116* (23), 5586–5594.

(5) Rury, A. S.; Wiley, T. E.; Sension, R. J. *Acc. Chem. Res.* **2015**, *48* (3), 860–867.

(6) Frey, P. A.; Hegeman, A. D. *Enzymatic Reaction Mechanisms*; 2007; Vol. 1.

(7) Snellenburg, J. J.; Laptenok, S. P.; Seger, R.; Mullen, K. M.; van Stokkum, I. H. M. *J. Stat. Softw.* **2012**, *49* (3).

(8) Wiley, T. E.; Arruda, B. C.; Miller, N. A.; Lenard, M.; Sension, R. J. *Chinese Chem. Lett.* **2015**, *26* (4), 439–443.

(9) Harris, D. A.; Stickrath, A. B.; Carroll, E. C.; Sension, R. J. *J. Am. Chem. Soc.* **2007**, *129* (24), 7578–7585.

(10) Kumar, M.; Kozlowski, P. M. *Chem. Phys. Lett.* **2012**, *543*, 133–136.

(11) Lodowski, P.; Jaworska, M.; Kornobis, K.; Andruni, T.; Kozlowski, P. M. *J. Phys. Chem. B* **2011**, *115*, 13304–13319.

(12) Solheim, H.; Kornobis, K.; Ruud, K.; Kozlowski, P. M. *J. Phys. Chem. B* **2011**, *115* (4), 737–748.

(13) Kornobis, K.; Kumar, N.; Wong, B. M.; Lodowski, P.; Jaworska, M.; Andruniów, T.; Ruud, K.; Kozlowski, P. M. *J. Phys. Chem. A* **2011**, *115* (7), 1280–1292.

(14) Lodowski, P.; Jaworska, M.; Andruniów, T.; Garabato, B. D.; Kozlowski, P. M. *Phys. Chem. Chem. Phys.* **2014**, *16* (35), 18675.

(15) Stich, T. A.; Buan, N. R.; Brunold, T. C. *J. Am. Chem. Soc.* **2003**, *125*, 5897–5914.

(16) Fugate, R. D.; Chin, C.; Song, P. *Biochim. Biophys. Acta* **1976**, *421*, 1–11.

Chapter 7

Conclusions and future directions

Molecular motors. A combination of transient absorption (TA), pump repump probe (PrPP) and pump dump probe (PDP) has been used to study the excited state dynamics and photoproducts of the all of the conformations (P-cis, M-cis, P-trans, and M-trans) in the rotary cycle of a first generation molecular motor. The data show interesting differences between the photoisomerization of P-cis and P-trans.

The data support a model where P-trans forms M-cis through a single conical intersection. This is indicated by the photochemical production of P-trans from M-cis in PrPP experiments. In addition, low temperature photolysis of P-trans creates a photo-stationary state between M-cis and P-trans. Metastable M-cis is photoactive, isomerizing in the reverse direction of the intended rotation direction of the molecular motor. In contrast, P-cis appears to have two conical intersections involved in its excited state reaction path. Excitation of M-trans, probed by standard TA and PrPP, shows return of M-trans to the ground state with no measureable photoproducts. Thus, the conical intersection responsible for M-trans ground state recovery is essentially unity. However, P-cis is not likely to form M-trans with quantum yield equal to unity. There is likely a second conical intersection that P-cis reaches earlier on, determining the overall P-cis to M-trans quantum yield. Low temperature photolysis of P-cis supports this finding as well. Photolysis is able to drive P-cis completely to M-trans because M-trans is not photoactive.

Details of the ground state distribution of P-trans also became clear through TA and steady state fluorescence experiments. The UV-vis spectrum of P-trans in solution at room temperature

has a small shoulder on the red edge (> 385 nm) as shown in Chapter three Figure 3.18. If this shoulder is excited by the second harmonic of the laser at 404 nm, the resulting TA spectra are very different than TA observed exciting with 368 nm or 269 nm. The second harmonic excitation TA data are in agreement with PrPP of the P-cis photoproducts, which are M-trans. In addition, the steady state fluorescence spectrum of a P-trans solution, when excited with 400 nm versus 368 nm is red shifted and more broad as seen in Chapter three Figure 3.19. All of these results imply a small amount of M-trans in equilibrium with P-trans in solution at room temperature.

These investigations of the first generation molecular motor show important photochemical properties, which could be improved upon. It is undesirable for isomerization to occur in the backwards direction in the case of M-cis. This backwards rotation will limit the overall efficiency of the molecular motor. Some light energy will be wasted driving the motor backward. On the other hand, the isomerization of P-cis to M-trans shows a more promising design for increasing the efficiency of the molecular motor. The M-trans isomer is not photoactive, showing no isomerization in the backwards direction.

Many questions remain to be addressed. Foremost, theoretical calculations to search for the two conical intersections involved in the photoisomerization of P-cis and the single conical intersection involved in the photoisomerization of P-trans are needed to test the pathways proposed in Chapter four. Many theoretical investigations to date have stressed the importance of multiple conical intersections in the isomerization of similar molecular motors[1–6]. Low temperature actinometry of the isomers to determine the quantum yields of isomerization for P-cis, P-trans, and M-trans would be excellent supporting information.

Additional PrPP experiments are of interest as well. Foremost, the uncertainty introduced to the P-cis PrPP data as a result of the "α" scale factor was an unforeseen issue in the experimental design. Future PrPP experiments must either: (1) develop a calibration procedure for determining α, or (2) more preferably use a repump wavelength not absorbed by the ground state of the sample. A repump pulse at 800 nm could target the early excited state absorption (ESA) and also alleviate the α factor issue. A repump pulse at ~ 430 nm could more optimally target the sharp ESA peaks of the dark states of P-trans and P-cis.

Finally, moving to a second generation molecular motor is a necessary direction for future research efforts. For one, the second generation molecular motor has two rather than four conformations, which provides a simplified model system. Second, a molecular motor with stronger absorptions at the convenient wavelengths (400 or 500-700 nm) of the laser system would improve the data quality. Several second generation molecular motors syntheses are published for structures which larger extinction coefficients at 400 nm[7–11].

Photochromic photoacids. The nature of the photoproduct formed by phenylhydroxy-MCH depends on the solvent in which the molecule is dissolved. If phenylhydroxy-MCH is dissolved in aqueous buffer, a long-lived intermediate likely a cis merocyanine isomer is formed on a 10 ps timescale which persists for >> 3.5 ns. This cis isomer goes on to form phenylhydroxy-SP. However, if phenylhydroxy-MCH is dissolved in DMSO, it produces phenylhydroxy-SP on a ~ 50 ps timescale. Calculations of the barrier for phenylhydroxy-SP formation from CCC-phenylhydroxy-MC$^-$ show a hydrogen bonding water molecule can increase the barrier by ~ 2 kcal/mol, enough to decrease the rate by a factor of 40. Contrary to the reported mechanism by Liao et al.[12], the conjugate base phenylhydroxy-MC$^-$ shows no measureable quantum yield for

ring closure. Finally, the indazole-MCH photoproduct in TA experiments shows little dependence on whether aqueous buffer or DMSO is used.

There are several questions that have emerged from these initial photochromic photoacid studies. Foremost, if the long-lived phenylhydroxy photoproduct in aqueous buffer is stabilized by hydrogen bonding, then a solvent composition study would be useful for testing this. Small percentages of water could be added to DMSO (0.5%, 1.0%, 2.0% for example) and TA could be done as a function of these solvent mixtures. Second, there are many published reports of similar spiropyran/merocyanine molecules with ground state inhomogeneity[13–15]. Typically the TTT and TTC merocyanine are present in solution, and these conformers display unique excited state dynamics and photoproduct quantum yields. Work by Brixner et al.[14,15] has clearly demonstrated these findings by scanning the excitation wavelength in transient absorption. Experiments of this kind have recently become possible with the founding of the Laboratory for Ultrafast Multidimensional Optical Spectroscopy (LUMOS).

Hydroxocobalamin and Aquocobalamin. Hydroxocobalamin (HOCbl) and aquocobalamin (H_2OCbl) are UV light activated hydroxyl radical photocatalysts. Irradiation of HOCbl or H_2OCbl with wavelength ≤ 300 nm produces hydroxyl radicals and Cob(II)alamin. If the procedure is carried out under aerobic conditions, dissolved oxygen will react with the Cob(II)alamin to reform HOCbl or H_2OCbl. This property is unexpected since the non-alkylcobalamins are considered photostable[16–20]. However, this property has attracted the attention of biochemists looking for chemically mild light activated hydroxyl radical delivery agents for DNA hydroxyl damage research[21,22].

Many previous studies of the TA of HOCbl have not accounted for the pKa of the Co-OH group, around 8[16,23,24]. As a result, these studies actually examined mixtures of HOCbl and H_2OCbl, and the lifetimes obtained in their analyses can be explained by an average of the lifetimes of HOCbl and H_2OCbl weighted by their concentrations. Furthermore, the peak centers of the excited state spectra of H_2OCbl are much closer to the peak centers of the ground state spectrum. In contrast, HOCbl's excited state spectrum is much more different than its ground state. This is likely an indication of the relative changes in the axial bond lengths between the two molecules in their excited states. Transient anisotropy studies have been conducted to investigate the angles of the transition dipole moments for both molecules, but more work is needed to analyze these results. The main issue is the large number of overlapping peaks in the ground and excited states, making a detailed analysis difficult.

The proposed pathway for photolysis of HOCbl is high energy excitation allows the molecule to access a dissociative region of its S_1 potential energy surface. This is demonstrated by TA with 269 nm excitation and careful anaerobic photolysis with $\leq$ 300 nm[25]. Future work investigating this dissociative pathway should make use of PrPP spectroscopy. Excitation of the molecule with 404 nm and repumping with 808 nm at very early times after excitation, ~ 100 – 200 fs, could supply enough energy to reach this dissociative pathway without using UV light. Scanning the time delay of the repump pulse while monitoring the photoproduct signal could find an optimal time delay for bond cleavage. If possible, this would be useful to the biochemistry community where UV light is often damaging to biological molecules.

Notes on Chapter 7

(1) Kazaryan, A.; Filatov, M. *J. Phys. Chem. A* **2009**, *113* (43), 11630–11634.

(2) Kazaryan, A.; Kistemaker, J. C. M.; Schäfer, L. V.; Browne, W. R.; Feringa, B. L.; Filatov, M. *J. Phys. Chem. A* **2010**, *114* (15), 5058–5067.

(3) Kazaryan, A.; Lan, Z.; Schäfer, L. V.; Thiel, W.; Filatov, M. *J. Chem. Theory Comput.* **2011**, *7* (7), 2189–2199.

(4) Filatov, M.; Olivucci, M. *J. Org. Chem.* **2014**, *79* (8), 3587–3600.

(5) Liu, F.; Morokuma, K. *J. Am. Chem. Soc.* **2012**, *134* (10), 4864–4876.

(6) Li, Y.; Liu, F.; Wang, B.; Su, Q.; Wang, W.; Morokuma, K. *J. Chem. Phys.* **2016**, *145* (24), 244311.

(7) Faulkner, A.; Van Leeuwen, T.; Feringa, B. L.; Wezenberg, S. J. *J. Am. Chem. Soc.* **2016**, *138* (41), 13597–13603.

(8) Vicario, J.; Meetsma, A.; Feringa, B. L. *Chem. Commun.* **2005**, 47, 5910–5912.

(9) Amirjalayer, S.; Cnossen, A.; Browne, W. R.; Feringa, B. L.; Buma, W. J.; Woutersen, S. *J. Phys. Chem. A* **2016**, *120* (43), 8606–8612.

(10) Conyard, J.; Addison, K.; Heisler, I. A.; Cnossen, A.; Browne, W. R.; Feringa, B. L.; Meech, S. R. *Nat. Chem.* **2012**, *4* (7), 547–551.

(11) Conyard, J.; Cnossen, A.; Browne, W. R.; Feringa, B. L.; Meech, S. R. *J. Am. Chem. Soc.* **2014**, *136* (27), 9692–9700.

(12) Shi, Z.; Peng, P.; Strohecker, D.; Liao, Y. *J. Am. Chem. Soc.* **2011**, *133* (37), 14699–14703.

(13) Hobley, J.; Pfeifer-Fukumura, U.; Bletz, M.; Asahi, T.; Masuhara, H.; Fukumura, H. *J. Phys. Chem. A* **2002**, *106* (10), 2265–2270.

(14) Buback, J.; Kullmann, M.; Langhojer, F.; Nuernberger, P.; Schmidt, R.; Würthner, F.; Brixner, T. *J. Am. Chem. Soc.* **2010**, *132* (46), 16510–16519.

(15) Nuernberger, P.; Ruetzel, S.; Brixner, T. *Angew. Chemie - Int. Ed.* **2015**, *54* (39), 11368–11386.

(16) Shiang, J. J.; Cole, A. G.; Sension, R. J.; Hang, K.; Weng, Y.; Trommel, J. S.; Marzilli, L. G.; Lian, T.; Arbor, A. *J. Am. Chem. Soc.* **2006**, *128* (3), 801–808.

(17) Rury, A. S.; Wiley, T. E.; Sension, R. J. *Acc. Chem. Res.* **2015**, *48* (3), 860–867.

(18) Wiley, T. E.; Arruda, B. C.; Miller, N. A.; Lenard, M.; Sension, R. J. *Chinese Chem. Lett.* **2015**, *26* (4), 439–443.

(19) Miller, N. A.; Wiley, T. E.; Spears, K. G.; Ruetz, M.; Kieninger, C.; Kräutler, B.; Sension, R. J. *J. Am. Chem. Soc.* **2016**, *138* (43), 14250–14256.

(20) Miller, N. A.; Deb, A.; Alonso-Mori, R.; Garabato, B. D.; Glownia, J. M.; Kiefer, L. M.; Koralek, J.; Sikorski, M.; Spears, K. G.; Wiley, T. E.; Zhu, D.; Kozlowski, P. M.; Kubarych, K. J.; Penner-Hahn, J. E.; Sension, R. J. *J. Am. Chem. Soc.* **2017**, *139* (5), 1894–1899.

(21) Shell, T. A.; Lawrence, D. S. *J. Am. Chem. Soc.* **2011**, *133* (7), 2148–2150.

(22) Kumar, M.; Kozlowski, P. M. *Chem. Phys. Lett.* **2012**, *543*, 133–136.

(23) Jones, A. R.; Russell, H. J.; Greetham, G. M.; Towrie, M.; Hay, S.; Scrutton, N. S. *J. Phys. Chem. A* **2012**, *116* (23), 5586–5594.

(24) Kutta, R. J.; Hardman, S. J. O.; Johannissen, L. O.; Bellina, B.; Messiha, H. L.; Ortiz-Guerrero, J. M.; Elías-Arnanz, M.; Padmanabhan, S.; Barran, P.; Scrutton, N. S.; Jones, A. R. *Nat. Commun.* **2015**, *6*, 7907.

(25) Wiley, T. E.; Miller, W. R.; Miller, N. A.; Sension, R. J.; Lodowski, P.; Jaworska, M.; Kozlowski, P. M. *J. Phys. Chem. Lett.* **2016**, *7* (1), 143–147.